DYNAMICS OF THE ICE AGE EARTH

RICHARD PELTIER

Department of Physics
University of Toronto
Toronto, Ontario, Canada

ADVANCES IN GEOPHYSICS, VOLUME 24

ISBN 0-12-018824-4

1. INTRODUCTION

For at least the past 10^6 yr, and most probably for the past 3×10^6 yr, the Northern Hemisphere continents near the rotation pole have been subjected to a continuous cycle of glaciation and deglaciation. During this Pleistocene period, in which the first manlike fossils are to be found in deposits from East Africa dated at about 3.0×10^6 yr B.P., vast continental ice sheets have waxed and waned on a regular time scale of about 10^5 yr (e.g., Broecker and Van Donk, 1970). At each glacial maximum the mass contained in these transient ice complexes has been on the order of 10^{19} kg, equivalent to a global drop of sea level of approximately 10^2 m, which is itself approximately 1 part in 10^6 of the entire mass of the planet. It should not be surprising, given the vast dimensions of this naturally recurring phenomenon, that it has inspired an intense interest not only among members of the geological and geophysical communities but also among atmospheric scientists, zoologists, botanists, and archaeologists, to name but a few of the disciplines whose members have made important contributions to its understanding. Although the Ice Age industry, begun by the Swiss zoologist Louis Agassiz over 150 years ago, has matured considerably since Agassiz' time, it has yet to provide a fully satisfactory explanation either for the occurrence of the Ice Age itself or for the quasi-periodic life cycle of its major ice sheets. The purpose of this paper is to provide a geophysical perspective on the current state of this industry, to summarize what we "know" or think we know because of our employment in it, and to attempt to reveal as clearly as possible the issues which remain to be settled as effort continues.

The geophysical importance of the Ice Age is connected both with the magnitude of the stress to which the planet was subjected in consequence of the growth of individual ice sheets on its surface and with the time scale over which these surface loads were applied. Because of the magnitude of the loads, the deformation of the planet's shape effected by mutual gravitational attraction between load and planet was sufficiently large as to leave easily observable effects in the geological record. Because of the duration of individual loading events, on the other hand, the strains produced by loading are not entirely elastic in nature. Indeed, the 10^5-yr time scale is such that the total deformation is dominated by an effectively viscous response to the gravitationally induced stress field, a viscous response through which the coupled system tends inexorably toward a state of isostatic (gravitational) equilibrium. Although the concepts of isostasy and isostatic adjustment are crucial to the understanding of a wide variety of geophysical observations (e.g., the lack of a gravity anomaly associated with the contrast between continents and oceans, the lack of a gravity anomaly associated

with large mountain complexes, and the observed ratio of the Bouger gravity anomaly over continents to the topography as a function of topographic wavelength), virtually all of these observations refer to the properties of the planet in the fully adjusted (isostatic) state. The observations associated with the phenomenon of glacial isostatic adjustment, on the other hand, are geophysically unique in that they not only provide evidence for the *existence* of this process but also provide us with quantitative information concerning the *rate* at which isostatic adjustment proceeds.

If the elastic properties and density of the earth are considered fixed by the frequencies of its elastic gravitational free oscillations (e.g., Gilbert and Dziewonski, 1975), then the rate of isostatic adjustment is governed by a single physical parameter—the effective viscosity of the planetary mantle. Even in Wegener's (1926) book "The Origin of Continents and Oceans," in which the complete (for the time) range of arguments in favor of the hypothesis of continental drift was first put forward, the observation of delayed vertical motion associated with the Fennoscandian deglaciation was included as the central argument in favor of the ability of mantle material to deform as a viscous fluid in spite of the fact that it has a seismically observed shear modulus approaching that of cold steel. Wegener argued that if such apparently viscous vertical motion could occur then similar horizontal motion should also be possible. Continents composed of relatively low-density granitic material surrounded by a more dense viscous sea of mafic or ultramafic material might then be considered analogous to blocks of ice floating in water. Although Wegener's hypothesis was considered to be quite disreputable in many if not most geological circles until the early 1960s, a torrent of new geophysical discoveries beginning at that time (particularly in paleomagnetism and seismology) quickly enforced a new conformity to it. Today, of course, this hypothesis is firmly entrenched as the paradigm in terms of which most geological and geophysical research is organized. The importance of the study of glacial isostatic adjustment to the internal self-consistency of this paradigm remains what it was in Wegener's time. It is the only reliable method we have of obtaining a direct *in situ* measurement of the viscosity of the planetary mantle and of determining its variation with depth. This parameter is a crucial variable in modern thermal convection theories of the drift process itself (Peltier, 1980b; Jarvis and Peltier, 1982).

The first quantitative attempt to infer the viscosity of the mantle from isostatic adjustment data was that by Haskell (1935, 1936, 1937), who was followed immediately in this work by Vening-Meinesz (1937). Both authors employed a Newtonian viscous half-space model of the earth with constant density and viscosity and inferred an effective viscosity from the observed recovery history of Fennoscandia following the deglaciation event which

began ca. 20 kyr B.P. The value of the viscosity which they inferred was very near 10^{21} Pa sec. Since no direct method of determining the ages of individual strandlines required to determine the history of uplift was then available, it is a testimony to the excellence of the varve-based chronology reported by Lidén (1938; see Mörner, 1980) that application of modern direct methods of dating to the stratigraphic sequence has led to no significant alteration of the value of the upper mantle viscosity which is inferred from the data. The advent of the radiocarbon method of dating (Libby, 1952) has nevertheless had a profound effect upon the study of glacial isostasy by removing the necessity of possessing such detailed stratigraphic information to control the time scale. The first application of ^{14}C dating in the construction of relative sea level (RSL) histories of which I am aware is that by Marthinussen (1962) in a study of the shorelines of northern Norway. Elsen's (1967) reconstruction of the history of North American glacial Lake Agassiz (which was centered on the present lakes Winnipeg and Winnipegosis in the Canadian province of Manitoba) using ^{14}C dating is also a noteworthy early contribution. The 5730 (±40)-yr decay time for the beta disintegration of ^{14}C ($^{14}C \rightarrow \beta^- + {}^{14}N^+$) makes the method perfectly suited to the study of the sea level record during the past 20 kyr since glacial maximum. Very recently devised accelerator-based techniques for ^{14}C dating, which count atoms directly (Litherland, 1980), are expected to gradually replace conventional β-counting in many applications. These new methods make it possible to obtain dates from much smaller samples ($\lesssim$1 mg) than can by analyzed conveniently using the method developed by Libby and his co-workers.

Since the pioneering studies of mantle viscosity by Haskell and Vening-Meinesz there have been an enormous number of similar investigations reported by other workers using either the same data set or similar information from other geographic locations. The most important locations outside of Fennoscandia include the North American continent as a whole (the northern half of which, Canada, was covered by the huge Laurentide ice sheet at 20 kyr B.P.) and the region surrounding the much smaller scale glacial Lake Bonneville, which was located in what is now the state of Utah in the Basin and Range geological province. Taken together with the data from Fennoscandia, the observations from these regions provide information on the isostatic adjustment of horizontal scales of surface deformation ranging over a full order of magnitude from a few hundred to a few thousand kilometers. Since the horizontal scale of the adjusting region in part determines the vertical extent of the flow through which isostatic adjustment takes place, the existence of data covering such a wide range of spatial scales promises the capability of using it to infer the variation of viscosity as a function of depth in the mantle. Until rather recently, the scientific results

obtained through inversion of the combined data set have proved to be extremely controversial.

The Newtonian viscous half-space model of Haskell and Vening-Meinesz predicts that a sinusoidal surface deformation with horizontal wave number k_H should decay exponentially in time with decay constant $\tau = 2\nu k_H/\rho g_s$, in which ν is the viscosity, ρ the density, and g_s the surface gravitational acceleration. Van Bemmelen and Berlage (1935), working at the same time as Haskell and on the same data set, assumed that isostatic adjustment was confined to a thin channel near the surface of depth h. Their analysis showed the relaxation time for this model to be $\tau = (12\nu/\rho g_s h^3)(1/k_H^2)$ and thus to depend inversely upon the square of deformation wave number. Assuming h to be 100 km, they inferred a viscosity of $\nu = 3 \times 10^{18}$ Pa sec [1 Pa sec (SI units) = 10 P (cgs units)]. Although the flaws in this thin-channel model (low near-surface viscosity in spite of low near-surface temperature, inability to fit relaxation amplitude and relaxation time simultaneously, etc.) are much more evident today than they were in the late 1930s, the model nevertheless disappeared from the early literature for some time. Its later resurrection may be attributed to Crittenden (1963). Crittenden had compiled data for the relaxation associated with the disappearance of Pleistocene Lake Bonneville and discovered that although the spatial extent of this region differed by an order of magnitude from that of Fennoscandia, the relaxation times for the two regions differed only slightly—both being on the order of 5000 yr. These results seemed to Crittenden to support the idea of thin-channel flow, since Haskell's model predicted that relaxation time should increase continuously with wave number whereas the channel model predicted a decrease. Even in 1963 there was therefore a body of informed geophysical opinion which considered that the effective viscosity of the earth was anomalously low in the coldest layer immediately adjacent to the surface!

The controversy over simultaneous interpretation of the Lake Bonneville and Fennoscandia data inspired the work of McConnell (1968), who realized that the increasing confinement of the flow to the near-surface region as wavelength decreased which these data *seemed* to demand did not require infinitely rigid material beneath some critical depth but could be accommodated by a model in which viscosity increased smoothly. His was the first attempt to use the $\tau(k_H)$ information contained in the Fennoscandia data to directly constrain the ν(depth) profile, and many of his conclusions remain valid today. The only novel feature which McConnell's model contained was a "lithospheric" layer at the surface in which the viscosity was infinitely high but whose thickness was variable. He found that the relaxation spectrum $\tau(k_H)$ extracted from the Fennoscandia data required the presence of such a layer and constrained its thickness to be near 120 km.

Although the required presence of such a layer agrees in a satisfying way with modern *a priori* expectation based upon knowledge of the temperature dependence of viscosity and the fact that temperature increases markedly with depth near the planetary surface, the picture is nevertheless rather different from that advocated in the model of Van Bemmelen and Berlage and supported by Crittenden. As demonstrated by McConnell, the presence of the thin surficial elastic lithosphere modifies Haskell's model in such a way that for wavelengths shorter than a few times the lithospheric thickness, relaxation time is forced to decrease with increasing deformation wave number. Modern theory, discussed in Section 3, shows the effect to be such that the spatial scales of Fennoscandia and Lake Bonneville straddle the maximum in the $\tau(k_H)$ spectrum and thus have comparable relaxation times though their spatial scales are separated by an order of magnitude (see Fig. 13).

The results obtained by McConnell (1968) for the viscosity stratification beneath the lithosphere have not proved as immune to later analysis as have his inferences concerning the lithosphere itself. McConnell found that the $\tau(k_H)$ data from Fennoscandia, determined by the spectral decomposition of Sauramo's (1958) shoreline diagram, required an upper mantle viscosity which is very nearly constant and equal in magnitude to 10^{21} Pa sec (10^{22} P), the same value previously inferred by Haskell. He was aware that the $\tau(k_H)$ data themselves were insensitive to viscosity structure beneath a depth of about 600 km, a fact which was later demonstrated by Parsons (1972) using the formal resolving-power analysis developed by Backus and Gilbert (1967, 1968, 1970). In order to constrain the viscosity profile beneath this depth, McConnell was obliged to invoke extra information. What he did was to assume that a so-called nonhydrostatic bulge existed; that is, that the polar flattening of the planet (produced by the centrifugal force) was in excess of that which would be in equilibrium with the current rotation rate, an idea which had been advocated by Munk and MacDonald (1960). He further assumed that the excess bulge was produced by glaciation. (Although this assumption is incorrect, we show in Section 6 that there are nevertheless important observable effects of deglaciation upon the earth's rotation which *can* be employed to constrain mantle viscosity.) It followed to McConnell from the existence of the bulge that it must have been relaxing very slowly and therefore that the relaxation time of the degree-two harmonic was in excess of $\tau = O(10^4)$ yr. This requires a high value for the viscosity beneath 670 km depth (the lower mantle), and McConnell described models in which the lower mantle viscosity was constrained to be in excess of 10^{23} Pa sec (10^{24} P). McKenzie (1966, 1967, 1968) came to a similar conclusion which was also based upon the assumption that the nonhydrostatic equatorial bulge was a genuine characteristic of the planet and preferred models for the mantle viscosity profile in which the lower

mantle value was greater than 10^{25} Pa sec (10^{26} P). This argument for extremely high viscosity in the lower mantle was completely undermined by Goldreich and Toomre (1969), who pointed out that the crucial non-hydrostatic equatorial bulge did not in fact exist! It had been inferred from a spherical harmonic expansion which was improperly biased to the degree-two harmonic. The question of the magnitude of the viscosity in the deep mantle remained open.

It was beginning about this time that data from ^{14}C-dated shorelines in Canada began to become available in sufficient quantity and quality as to promise a considerable enhancement of depth resolution. Although major papers containing detailed observations on the rebound of the crust in North America began appearing in the early 1960s (Løken, 1962; Farrand, 1962; Washburn and Struiver, 1962; Bloom, 1963), it does not appear that any detailed efforts at geophysical interpretation were attempted prior to the paper by Brotchie and Sylvester (1969), who were followed by Walcott (1970). Brotchie and Sylvester were among the first to consider the isostatic recovery problem using a spherical model, but their work did not lead them to any particular interpretation of the mantle viscosity profile, although they did note that the observed relaxation times in North America were short (1000–1500 yr) and that they could fit them with their model. Such short relaxation times were also reported by Andrews (1970), based upon data from Baffin Island and other sites in the Canadian Arctic, who noted apparent relaxation times on the order of 2000 yr. The validity of this observation is also clear from the rather complete set of North American RSL data compiled by Walcott (1972). If one employs Haskell's half-space model to infer a viscosity from this relaxation time, for a deformation of Laurentide scale, one obtains a value for the viscosity of the mantle which is very nearly the same as that implied by the Fennoscandia data, i.e., $\sim 10^{21}$ Pa sec. Because of the considerable increase of the horizontal scale of the Laurentide load over that which existed on Fennoscandia, the isostatic adjustment of Canada is sensitive to viscosity variations across the seismic discontinuity at 670 km depth, which marks the boundary between the upper and lower mantle. Since the viscosity inferred from the two data sets is the same, the implication is clearly that there is no substantial viscosity contrast across this boundary. This conclusion was enforced in work by Cathles (1975), Peltier (1974), and Peltier and Andrews (1976), who employed spherical viscoelastic models and showed that radiocarbon-controlled RSL data from the Hudson Bay region and from the eastern seaboard of North America could not be fit by models which had any extreme contrast in viscosity between the upper and lower mantle. This result has had considerable influence on the recent debate concerning the style of the convective circulation in the mantle.

It is a result which has proved to be controversial, however—as contro-

versial as was the interpretation of the combined uplift data from Fennoscandia and Lake Bonneville. The reason for the controversy over interpretation of isostatic adjustment data from North America has concerned an apparent contradiction between the short relaxation time obtained from RSL data and the rather large free-air gravity anomaly which is observed over Hudson Bay, in very close apparent correlation with the topography of the Laurentide ice sheet at glacial maximum. A discussion of this difficulty first appeared in Walcott (1970), who presented a free-air gravity anomaly map based upon the work of Innes *et al.* (1968) which shows a clear elliptical anomaly trending NW with an amplitude of approximately −35 mGal. The zero anomaly contour on the map passes through the St. Lawrence Valley, the Great Lakes, lakes Winnipeg and Athabaska, Great Bear and Great Slave lakes, and Melville Sound; in other words, virtually coincident with the edge of the ancient Laurentide ice sheet (e.g., Bryson *et al.*, 1969). As Walcott (1970) argues and later (Walcott, 1973, 1980) reiterates, it seems preposterous to suppose, as have O'Connell (1971) and Cathles (1975), that this gravity anomaly is unrelated to the currently existing degree of isostatic disequilibrium associated with the melting of Laurentide ice. Yet if one does ascribe the anomaly to deglaciation one is led to an impasse, since one then estimates an amount of uplift remaining to be $\Delta h = \Delta g/2\pi G\rho$ (where Δg is the observed gravity anomaly, G the gravitational constant, and ρ the density of the material displaced to form the depression), which gives approximately 250 m. As Walcott correctly argues, this large remaining uplift is incompatible with exponential relaxation of the uplift with a time constant as low as 2×10^3 yr. Rather, he asserts that *if the relaxation is purely exponential* then the relaxation time must be "between 10,700 and 17,100" yr, which he (Walcott, 1970) recognized to be an order of magnitude greater than that implied by the sea level data. This is the contradiction which has fueled recent controversy. In his 1970 paper, Walcott suggests an empirical way out of this dilemma by showing that if the relaxation consisted of a superposition of two exponential decays, so that the remaining uplift (in meters) obeyed an expression like "$h = 150e^{-t/10^3\ \mathrm{yr}} + 450e^{-t/5 \times 10^4\ \mathrm{yr}}$," then the impasse might be avoided. He suggests three possible physical effects which might support such behavior: (1) the presence of a lithosphere, (2) the presence of viscosity stratification with a low-viscosity "asthenosphere" overlying a high-viscosity lower mantle, or (3) non-Newtonian effects. As we show in Sections 3, 4, and 5 of this article, Walcott's empirical idea turns out to be almost correct, but for none of the physical reasons he suggested! His own currently preferred explanation (Walcott, 1980) is that relaxation times in Hudson Bay are in fact in excess of 10,000 yr, even though this must be considered extremely unlikely given the weight of observational evidence to the contrary.

Virtually all authors who have attempted to infer the viscosity of the deep mantle from isostatic adjustment data and have come to the conclusion that the viscosity of the mantle is essentially constant have had to ignore the free-air gravity data in order to support their claims. Cathes (1975), for example, argues along with O'Connell (1971) that there is no substantial deglaciation-related free-air anomaly associated with either the Laurentide or Fennoscandian depressions. Such correlations as apparently exist are considered by them to be merely coincidental. O'Connell's argument for a low value of the deep mantle viscosity is particularly interesting. He attempted to infer a mean value for mantle viscosity by *assuming*, following Dicke (1969), that the cause of the nontidal component of the acceleration of the earth's rotation was Pleistocene deglaciation (we prove by direct calculation in Section 6 that this assumption is correct). His analysis led him to believe that either one of two possible relaxation times for the degree-two harmonic would allow him to fit these data, the two relaxation times being near 2×10^3 and 10^5 yr, respectively. To determine which of these times was appropriate, he compared the potential perturbation produced by the shift in surface load to the earth's present anomalous gravitational potential as determined by the satellite data available to him at that time. Since he found no correlation between these fields, he concluded that compensation must be complete and therefore that the correct relaxation time was the smaller of the two, so that the mean mantle viscosity was low. Walcott (1980) accepts O'Connell's claim of a lack of correlation and provides an argument (which does not seem reasonable to me) as to why this result should imply that the longer relaxation time must be preferred. It is quite clear from more modern satellite data (e.g., Lerch *et al.*, 1979), however, that there is a very good correlation between the geoid anomaly and Laurentide ice topography, as clear as that shown by the surface free-air data.

Several authors have used the apparent inability of Newtonian viscoelastic earth models to simultaneously satisfy the RSL and free-air gravity data as a point of departure from which to launch rather extreme theories for the rheology of the planetary mantle. Jeffreys (1973), for example, has maintained his longstanding argument that this difficulty was due to the fact that the assumption of a steady-state Newtonian viscous rheology for the long-term behavior of the earth was fundamentally in error. He argues that *any* steady-state deformation of mantle material is impossible and as a corollary to this that thermal convection in the mantle cannot occur. Although somewhat less extreme in their views. Post and Griggs (1973) begin from the same point and argue (using data from Lliboutry, 1971, on uplift at the mouth of the Ångerman River in Sweden) that the observed relation between the uplift remaining and the rate of uplift demands that the mantle

be non-Newtonian in its mode of steady-state deformation. Their conclusion is based upon the assumption that the present-day free-air anomaly over Fennoscandia produced by deglaciation is about −30 mGal. The actual anomaly is closer to −15 mGal according to Balling (1980) (Walcott, 1973, accepts −17 mGal), and this completely undermines the argument of Post and Griggs that the Fennoscandian rebound provides direct evidence for non-Newtonian behavior and for a power law exponent near $n = 3$. Cathles (1975), in his arguments in favor of uniform mantle viscosity, is forced to argue that the free-air anomaly over Fennoscandia associated with deglaciation is only −3.5 mGal, which is also, and clearly, incorrect on the basis of modern analyses of this field. Anderson and Minster (1979), following a suggestion by Weertman (1978), have adopted a position with respect to the rebound observations which is also rather difficult to defend. They have argued that postglacial rebound is in a transient creep regime rather than the regime of steady-state deformation and so are philosophically close to Jeffreys. Peltier *et al.* (1980) have provided several arguments as to why this suggestion is unreasonable. These few citations should suffice to demonstrate that the apparent inability of Newtonian viscoelastic earth models to fit both gravity and sea level data simultaneously have caused many geophysicists to adopt extreme positions concerning the rheology. In Section 2 of this article we describe a simple linear viscoelastic rheology which appears capable of reconciling geodynamic phenomena with time scales which encompass the entire spectrum between those of the elastic gravitational free oscillations and those of mantle convection. The steady-state behavior of this model is Newtonian viscous, and the transient creep regime lasts only about 200 yr.

Aside from demonstrating in the following sections of this article the way in which the modern theory of glacial isostasy is able to simultaneously reconcile observations of RSL and free-air gravity, we also show that certain characteristic properties of the earth's history of rotation are attributable to Pleistocene deglacial forcing. The existence of such effects is particularly important since they depend only upon the degree-two harmonic of the glaciation-induced deformation and therefore provide optimal information on the viscosity of the deepest mantle. One of these effects is the observed nontidal component of the acceleration of rotation which is responsible for the observed nontidal variation of the length of day. Although this cause-and-effect relation was previously assumed by O'Connell (1971) following the suggestion of Dicke (1966), we will discuss the recent results of Peltier and Wu (1982), who calculate this effect directly. The second of the deglaciation-related rotation effects discussed here is the observed secular drift of the rotation pole as recorded astronomically by the International Latitude Service (ILS) and the International Polar Motion Service (IPMS) over the

time period 1900–1980. This drift is at a rate near $1°/10^6$ yr toward Hudson Bay and as pointed out by Sabadini and Peltier (1981) seems also to be due to deglacial forcing. When these rotation data are combined with the RSL and free-air gravity information, we are able to constrain the mantle viscosity profile to depths which extend well into the lower mantle.

Although Sections 2–6 of this article deal exclusively with the theory and phenomenology of glacial isostatic adjustment, Section 7 has been included to provide one example of an application of the theory of glacial isostasy to an important problem in paleoclimatology. Recent analyses of the magnitude of the ratio of concentrations of the stable isotopes of oxygen ($^{18}O/^{16}O$) as a function of depth in sedimentary cores taken from the deep ocean basins have revealed certain remarkable properties of the climatic oscillations which have characterized the Pleistocene period (Hays *et al.*, 1976). Although it was initially believed (Emiliani, 1955) that this isotopic variability was a direct reflection of Pleistocene temperatures, it was subsequently established (Imbrie and Kipp, 1971) that the isotopic ratio for the most part reflected the variation of Northern Hemisphere ice volume. Hays *et al.* (1976) were able to transform the depth scale in some particularly long cores into a time scale by finding the depth corresponding to the Matuyama–Brunhes polarity transition of the earth's magnetic field, which is marked by certain faunal extinctions. Since the age of this polarity transition (~700 kyr B.P.) is known from the paleomagnetic time scale established on land, their assumption of constant sedimentation rate leads directly to a depth → time transformation. Power spectral analysis of the resulting time series revealed remarkable periodicities to be present in the history of ice volume fluctuations. Statistically significant spectral peaks were found corresponding to periods near 19,000, 23,000, 41,000, and 100,000 yr. These are all astronomically significant periods, the first two corresponding to the period of precession of the equinoxes, the next to the period of changes in orbital obliquity, and the last to the period on which changes occur in the eccentricity of the earth's orbit around the sun. Hays *et al.* (1976) of course interpreted their results in terms of Milankovitch (e.g., Imbrie and Imbrie, 1978) theory of paleoclimatic change, which attributed all major fluctuations in climate to variations in the insolation received by the earth due to precisely these changes in the orbital parameters. An embarrassing difficulty with this interpretation, however, is that there is no significant variation of insolation predicted on the period of 10^5 yr, yet it is at this period that well over 50% of the spectral variance in the ice cover record is found. In Section 7 we analyze a paleoclimatic model proposed by Weertman (1961, 1976) and more recently elaborated by Birchfield (1977) and Birchfield *et al.* (1981) which essentially involves coupling of a model of ice-sheet flow with a model of glacial isostatic adjustment. These

authors analyze the time variation of ice volume which would be produced by solar forcing of this nonlinear model and find that although there is a diffuse peak at 10^5 yr in the fluctuation time series it is overwhelmed by peaks at the forcing periods associated with orbital precession and obliquity. As we will show, however, the model of isostatic adjustment those authors employ is completely inadequate to describe this physical process. When results from the modern theory of glacial isostatic adjustment are used to redesign this model, we find that it does support a free relaxation oscillation at the observed period.

The process of glacial isostatic adjustment described in the main body of this article is therefore one which has rather wide-ranging importance in many fields of earth science. Indeed, the basic rudiments of the theory which has been developed to understand this collection of related phenomena (contained in Peltier, 1974, and later articles) has found application in the study of such diverse geophysical phenomena as the formation of sedimentary basins (Beaumont, 1978) and the relaxation of impact craters on Mars (Philips and Lambeck, 1980). It also contains within it, in a particular limit, a complete spherical viscoelastic description of the problem of lithospheric flexure which has proved useful in describing a number of other important geophysical observations (see the review by Turcotte, 1979). It is hoped that the following elaboration of these ideas may suggest further avenues of application.

2. Mantle Rheology: A Uniformly Valid Linear Viscoelastic Model

Perhaps the most important ingredient in the theory of glacial isostasy is the model which is employed for the rheology of the mantle. In a sense, all of the physical predictions of the theory follow immediately once the rheology is specified—given that some care is taken in solving the mathematical problem posed by the classical conservation laws. Since the question of the precise nature of the rheological law which governs the response of mantle material to an applied shear stress remains one of the most controversial in geodynamics, it is perhaps not inappropriate that we should begin by defending the particular form of the rheological law which will be employed in our subsequent analysis of glacial isostatic adjustment.

Although it is well known that for short time scale seismic processes the earth behaves essentially like a Hookean elastic solid, even on these time scales this rheological model is inadequate in many important respects. It does not, for example, predict the observed spatial attenuation of propagating surface waves, nor does it predict the observed finite quality factors

(Q's) of the elastic gravitational free oscillations. In recent years there has developed a consensus among seismologists that it is possible to describe all of these and some other consequences of the departure of the mantle from perfect Hookean elasticity using the *linear* relations between stress and strain, which are those appropriate for anelastic materials. Several similar relations have been proposed, including the modified Lomnitz law preferred by Jeffreys (1972, 1973) and the very closely related absorption band models adopted by Liu *et al.* (1976) and Minster and Anderson (1980a,b). Since anelastic materials (Nowick and Berry, 1972) predict *finite* strain in response to an applied shear stress which is maintained for an *infinite* length of time, they cannot support continuous flow such as that associated with thermal convection.

In order to support flow, the behavior of mantle material must become viscous in the long-time limit. As mentioned in the last section, early work on the problem of postglacial rebound was all predicated upon the *assumption* that the earth's mantle could be described as a Newtonian viscous fluid, and elastic effects due to loading were neglected entirely. This assumption may introduce substantial error, but to correct it we are forced to design a rheological model for mantle material which is *uniformly valid in time.* Its initial behavior must be that of an anelastic solid, while its final behavior must be that of a viscous fluid. Although the fact that mantle material does support a steady-state viscous mode of deformation has been very well established experimentally (e.g., Kohlstedt and Goetze, 1974; Durham and Goetze, 1977), the data from these high-temperature creep experiments suggest a nonlinear relation between stress and strain rate and therefore a non-Newtonian behavior in the steady-state viscous regime.

This question of the linearity or nonlinearity of the rheological law in steady-state creep is the most outstanding issue which remains to be settled concerning mantle rheology. The experimental studies cited above cannot be considered definitive for two reasons. The first of these concerns the fact that most of the experiments have been conducted on single crystals of olivine, whereas the mantle is polycrystalline. The second reason is that the experiments must be performed at stress levels and strain rates which are orders of magnitude different from those which obtain in postglacial rebound or in convection (strain rates of 10^{-6} sec^{-1} are typical of the experiments, whereas 10^{-16} sec^{-1} are typical natural strain rates). It could very well be that at natural stress levels near 10 Pa the rheological law governing steady-state creep could become linear as grain boundary processes become increasingly important. Recent studies by Twiss (1976), Berckhemer *et al.* (1979), Greenwood *et al.* (1980), and Breathau *et al.* (1979) are all suggestive of this possibility.

Given the plausibility that the rheological behavior of the mantle could

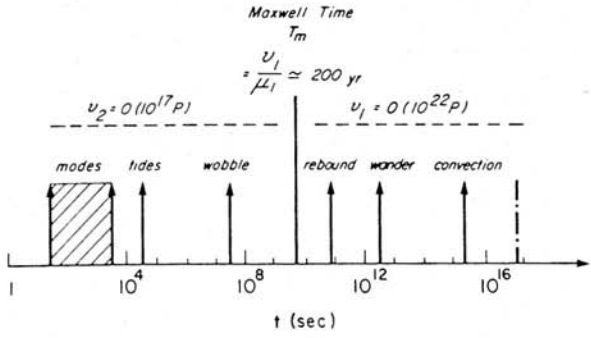

FIG. 1. Characteristic time scales of various geodynamic processes compared to the Maxwell time of the earth's mantle. Phenomena with characteristic times shorter than the Maxwell time should be governed by anelasticity, whereas those with longer characteristic time should be governed by steady-state viscous deformation.

very well be linear across the entire geodynamic spectrum, which includes the range of phenomenological time scales illustrated in Fig. 1, it is not at all unreasonable to inquire as to the form which a complete rheological law would then take. The development of this idea, which will be presented here, follows that in Peltier *et al.* (1981) and Yuen and Peltier (1982). Peltier *et al.* (1981) have argued that the simplest rheological law which is capable of describing the required transition from short-term anelastic to long-term viscous behavior is a model which they have called the *generalized Burgers body*. As is shown in what follows, this model behaves essentially as a Maxwell solid insofar as postglacial rebound is concerned if the parameters which determine the short time scale anelasticity are fixed by fitting the model to the observed Q's of the elastic gravitational free oscillations. We can consider the process of fitting the observations of glacial isostasy with this model as a basic consistency test of the model assumptions. If the model can be fitted to the data then we may conclude that the data contain no characteristics which demand a non-Newtonian rheology to explain them. This would not, of course, imply that the mantle was Newtonian, although it would provide strong circumstantial evidence of the possibility. Much more work on the isostatic recovery of non-Newtonian models of the sort begun by Brennan (1974) and Crough (1977) will have to be done if we are to understand the diagnostic characteristics of such physical behavior properly.

2.1. *The Generalized Burgers Body*

In Fig. 2 we show a sequence of standard spring and dashpot analogs to several common linear viscoelastic rheologies. The analog shown in Fig. 2c

is the simplest linear model which exhibits the transition from short-term anelastic to long-term viscous behavior, which is characteristic of the planetary mantle. It consists essentially of the superposition of the Maxwell model shown in Fig. 2a and the standard linear solid shown in Fig. 2b. A three-dimensional tensor form of the rheological constitutive relation for the Burgers body solid has been derived in Peltier *et al.* (1981) and has the form

$$\ddot{\sigma}_{kl} + \left(\frac{\mu_1 + \mu_2}{\nu_2} + \frac{\mu_1}{\nu_2}\right)\left(\dot{\sigma}_{kl} - \frac{1}{3}\dot{\sigma}_{kk}\,\delta_{kl}\right) + \frac{\mu_1\mu_2}{\nu_1\nu_2}\left(\sigma_{kl} - \frac{1}{3}\sigma_{kk}\,\delta_{kl}\right)$$
$$= 2\mu_1\ddot{e}_{kl} + \lambda_1\ddot{e}_{kk}\,\delta_{kl} + \frac{2\mu_1\mu_2}{\nu_2}\left(\dot{e}_{kl} - \frac{1}{3}\dot{e}_{kk}\,\delta_{kl}\right) \tag{2.1}$$

in which σ_{kl} and e_{kl} are the stress and strain tensors, dots denote time differentiation, μ_1 and λ_1 are the unrelaxed (elastic) Lamé parameters, and μ_2 is the shear modulus associated with the Kelvin–Voight element (parallel combination of spring and dashpot). For this model the elastic defect is $\Delta = \mu_1/\mu_2$. The two viscosities ν_1 and ν_2 are respectively the long and short time scale parameters which together control the range of time scales on which anelastic and viscous processes dominate (see Fig. 1).

Constitutive relations for the simpler Maxwell and standard linear solids may be derived from the Burgers body expression (2.1). In the limit $\nu_2 \to \infty$ Eq. (2.1) becomes

$$\ddot{\sigma}_{kl} + (\mu_1/\nu_1)(\dot{\sigma}_{kl} - \tfrac{1}{3}\dot{\sigma}_{kk}\,\delta_{kl}) = 2\mu_1\ddot{e}_{kl} + \lambda_1\ddot{e}_{kk}\,\delta_{kl}$$

which may be integrated once in time to give the Maxwell constitutive

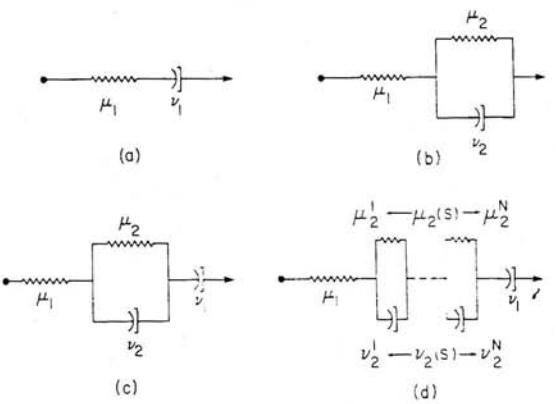

FIG. 2. Spring and dashpot analogs of several common linear viscoelastic rheologies. (a) Maxwell solid. (b) standard linear solid. (c) Burgers body solid. (d) the "generalized" Burgers body.

relation

$$\dot{\sigma}_{kl} + (\mu_1/\nu_1)(\sigma_{kl} - \tfrac{1}{3}\sigma_{kk}\,\delta_{kl}) = 2\mu_1\dot{e}_{kl} + \lambda_1\dot{e}_{kk}\,\delta_{kl} \tag{2.2}$$

which was introduced by Peltier (1974) in developing the linear viscoelastic theory of glacial isostasy. If in Eq. (2.1) we take the opposite limit $\nu_1 \to \infty$, then we obtain

$$\begin{aligned}\ddot{\sigma}_{kl} + [(\mu_1 + \mu_2)/\nu_2](\dot{\sigma}_{kl} - \tfrac{1}{3}\dot{\sigma}_{kk}\,\delta_{kl}) \\ = 2\mu_1\ddot{e}_{kl} + \lambda_1\ddot{e}_{kk}\,\delta_{kl} + (2\mu_1\mu_2/\nu_2)(\dot{e}_{kl} - \tfrac{1}{3}\dot{e}_{kk}\,\delta_{kl})\end{aligned}$$

which can also be integrated once in time to yield the rheological constitutive relation for the standard linear solid (SLS) as

$$\begin{aligned}\dot{\sigma}_{kl} + [(\mu_1 + \mu_2)/\nu_2](\sigma_{kl} - \tfrac{1}{3}\sigma_{kk}\,\delta_{kl}) \\ = 2\mu_1\dot{e}_{kl} + \lambda_1\dot{e}_{kk}\,\delta_{kl} + (2\mu_1\mu_2/\nu_2)(e_{kl} - \tfrac{1}{3}e_{kk}\,\delta_{kl})\end{aligned} \tag{2.3}$$

In the domain of the Laplace transform variable s, each of the linear viscoelastic constitutive relations (2.1)–(2.3) may be written in Hookean elastic form by direct Laplace transformation to give

$$\sigma_{kl} = 2\mu(s)e_{kl} + \lambda(s)e_{kk}\,\delta_{kl} \tag{2.4}$$

in which the moduli $\mu(s)$ and $\lambda(s)$ are functions of the Laplace transform variable. Explicit forms of these moduli for the four cases are as follows:

(1) *Hookean elastic solid*

$$\mu(s) = \mu_1 \qquad \lambda(s) = \lambda_1 \tag{2.5a}$$

(2) *Maxwell solid*

$$\mu(s) = \frac{\mu_2 s}{s + \mu_1/\nu_1} \qquad \lambda(s) = \frac{\lambda_1 s + \mu_1 K/\nu_1}{s + \mu_1/\nu_1} \tag{2.5b}$$

(3) *Standard linear solid*

$$\begin{aligned}\mu(s) &= \frac{\mu_1(s + \mu_2/\nu_2)}{s + (\mu_1 + \mu_2)/\nu_2} \\ \lambda(s) &= \frac{\lambda_1 s + \{[(\mu_1 + \mu_2)/\nu_2](\lambda_1 + \frac{2}{3}\mu_1) - \frac{2}{3}(\mu_1\mu_2/\nu_2)\}}{s + (\mu_1 + \mu_2)/\nu_2}\end{aligned} \tag{2.5c}$$

(4) *Burgers body solid*

$$\mu(s) = \frac{\mu_1 s}{s + \mu_1/\nu_1}\left[\frac{(s + \mu_1/\nu_2)(s + \mu_1/\nu_1)}{(s + \mu_2/\nu_2)(s + \mu_1/\nu_1) + \mu_1 s/\nu_2}\right]$$

$$\lambda(s) = \frac{\lambda s^2 + \left[\left(\dfrac{\mu_1 + \mu_2}{\nu_2} + \dfrac{\mu_1}{\nu_1}\right)\left(\lambda_1 + \dfrac{2}{3}\mu_1\right) - \dfrac{2}{3}\dfrac{\mu_1\mu_2}{\nu_2}\right]s + \dfrac{\mu_1\mu_2}{\nu_1\nu_2}\left(\lambda_1 + \dfrac{2}{3}\mu_1\right)}{s^2 + \left(\dfrac{\mu_1 + \mu_2}{\nu_2} + \dfrac{\mu_1}{\nu_1}\right)s + \dfrac{\mu_1\mu_2}{\nu_1\nu_2}} \tag{2.5d}$$

It is important to note that all of these constitutive relations have been designed under the constraint that they have zero bulk dissipation, which is to say that the bulk modulus $K = \lambda(s) + \frac{2}{3}\mu(s)$ is independent of s for every model. Dissipation is therefore realized only in shear and not in compression.

In spite of the fact that the Burgers body described through constitutive relation (2.1) displays the transition from initial anelastic to final viscous behavior which is required to understand the general behavior of the mantle, it is nevertheless incapable of fitting the full set of relevant observational data. The problem has to do with the single Debye peak representation of the anelastic behavior embodied in this model. As we will show through examples discussed below, when the simple Burgers body is employed to fit observations of the Q's of the elastic gravitational free oscillations, it is found to be incapable of delivering the weak dependence of Q upon frequency which is characteristic of the observations. In order to generate a viscoelastic model which does not suffer this deficiency, we are forced to consider constitutive relations which are not expressible in a simple differential form like Eq. (2.1). Generalized models such as are required to understand the short time scale viscoelastic structure of the earth require the superposition of a large number of distinct relaxation peaks, which are represented schematically by the chain of Kelvin–Voight elements in the analog shown in Fig. 2d. The necessity of using such models to describe the mantle makes this region of the earth very much like an amorphous polymer (Nowick and Berry, 1972) insofar as its rheology is concerned.

As the number of Kelvin–Voight elements in the chain approaches infinity, it becomes advantageous to describe the resulting constitutive relation in terms of the notion of a continuous relaxation spectrum (Gross, 1947; Zener, 1948; MacDonald, 1961; Liu *et al.*, 1976). This in turn necessitates use of the integral representation of the stress–strain relation which follows from the Boltzmann superposition principle. The most general form of such a relation is

$$\sigma_{ij}(t) = \int_{-\infty}^{t} C_{ijkl}(t - \tau)\dot{e}_{kl}(\tau)\, d\tau \tag{2.6}$$

where C_{ijkl} is a fourth-order tensor function for stress relaxation (Christensen, 1971) and the convolution integral over τ is to be regarded as a Stieltjes integral. For an isotropic material, Eq. (2.6) reduces to

$$\sigma_{ij}(t) = \delta_{ij} \int_{-\infty}^{t} \lambda(t - \tau)\dot{e}_{kk}(\tau)\, d\tau + 2 \int_{-\infty}^{t} \mu(t - \tau)\dot{e}_{ij}(\tau)\, d\tau \tag{2.7}$$

in which λ and μ are the two stress relaxation functions required to describe an isotropic linear viscoelastic solid. Assuming that the viscoelasticity of the mantle is felt only in shear and not in compression, then Eq. (2.7) becomes

$$\sigma_{ij}(t) = \delta_{ij} \int_{-\infty}^{t} \left[K - \frac{2}{3}\mu(t-\xi) \right] \frac{de_{kk}}{d\xi}\, d\xi + 2 \int_{-\infty}^{t} \mu(t-\xi) \frac{de_{ij}(\xi)}{d\xi}\, d\xi \quad (2.8)$$

where $K = \lambda + \frac{2}{3}\mu$ is the elastic bulk modulus as before.

If we first restrict our attention to the short time scale anelastic component of the rheology, it is useful to introduce the idea of a normalized relaxation function in describing the single parameter $\mu(t)$ which is needed in the integral constitutive relation (2.8). We define

$$\mu(t) = \mu_R \Delta\phi(t) \quad (2.9)$$

with μ_R the relaxed modulus of our generalized standard linear solid, $\Delta = (\mu_1 - \mu_R)/\mu_R$ the modulus defect of this solid, and $\phi(t)$ the normalized relaxation function. Following standard work on linear viscoelasticity (Gross, 1953; Christensen, 1971), we may further relate ϕ to the relaxation spectrum R through the integral transform

$$\phi(t) = \int_{-\infty}^{+\infty} R(\tau_\epsilon) e^{-t/\tau_\epsilon}\, d(\ln \tau_\epsilon) \quad (2.10)$$

In his recent work on transient wave propagation in an absorption band solid, Minster (1978) employed a relaxation spectrum which was parabolic in shape as

$$R(\tau_\epsilon) = (B/\tau_\epsilon) H(\tau_\epsilon - T_1) H(T_2 - \tau_\epsilon) \quad (2.11)$$

with τ_ϵ the relaxation time at constant strain, B a normalization constant, and H the Heaviside step function. Substitution of Eq. (2.11) into Eq. (2.10) and Eq. (2.10) into Eq. (2.9) followed by direct Laplace transformation of $\mu(t)$ gives the analytic expression for the transformed shear modulus as

$$\mu(s) = \mu_1 \left[1 + \frac{2}{\pi Q_m} \ln \frac{s + 1/T_2}{s + 1/T_1} \right] \quad (2.12)$$

From Eq. (2.8) it is then quite clear that the Laplace transform domain form of the constitutive relation is just

$$\delta_{ij}(s) = 2\mu(s) e_{ij} + [K - \tfrac{2}{3}\mu(s)] e_{kk}\, \delta_{ij} \quad (2.13)$$

which thus has the same Hookean elastic form as Eq. (2.4), which was obtained from the differential constitutive relations.

Now expression (2.12) has been found to provide a reasonably accurate description of the high-frequency anelastic behavior of the mantle and is also a form which has been commonly applied in similar analysis of polymers (Ferry, 1980). Using Minster's geophysically reasonable values for the model parameters ($Q_m = 250$, $T_1 = 10^{-2}$ sec, and $T_2 = 10^4$ sec), we may estimate the elastic defect $\Delta = (\mu_1 - \mu_R)/\mu_R$ to be

$$\Delta = \frac{(2/\pi Q_m)\ln(T_2/T_1)}{1 - (2/\pi Q_m)\ln(T_2/T_1)} \approx \frac{2}{\pi Q_m} \ln \frac{T_2}{T_1} \approx 0.03 \tag{2.14}$$

so that the difference between the relaxed and unrelaxed shear modulus is only 3%. Even though Eq. (2.12) provides a good phenomenological description of high-frequency processes, however, it is incapable of supporting thermal convection as it does not possess long-term viscous behavior.

In order to design a model which has both the correct long time scale and the correct short time scale behavior, we can appeal to the expression for the transformed shear modulus of the simple Burgers body given in Eq. (2.5d). Clearly, if we replace the expression in square brackets in the first equation of (2.5d) by the expression in square brackets in Eq. (2.12) we will obtain an expression for the transformed shear modulus which is *uniformly valid in time.* This is

$$\mu(s) = \frac{\mu_1 s}{s + \mu_1/\nu_1}\left[1 + \frac{2}{\pi Q_m} \ln \frac{s + 1/T_2}{s + 1/T_1}\right] \tag{2.15}$$

For $\mu_1/\nu_1 \ll s \ll 1/T_2$, Eq. (2.15) becomes

$$\mu(s) = \frac{\mu_1 s}{s + \mu_1/\nu_1}\left[1 - \frac{2}{\pi Q_m} \ln \frac{T_2}{T_1}\right] = \frac{\mu_R s}{s + \mu_1/\nu_1} \tag{2.16}$$

which is the expression for the transformed shear modulus of a Maxwell solid, so that in the low-frequency limit the *generalized Burgers body* described by Eq. (2.15) will behave like a Newtonian viscous fluid. In the high-frequency limit $s \gtrsim 1/T_2$, it will behave as a simple absorption band.

In the following two subsections we will provide simple illustrations of the ability of the rheological model (2.15) to fit both high- and low-frequency geophysical data.

2.2. *Free Oscillations of a Homogeneous Spherical Burgers Body*

Our intention in this subsection is to demonstrate the way in which free oscillations data may be employed to constrain the parameters Q_m, T_2, and T_1 which are required to specify the absorption band part of the generalized Burgers body rheology Eq. (2.15). We will restrict this discussion to consideration of a homogeneous, spherical, nonrotating, viscoelastic, and isotropic continuum which is perturbed from its hydrostatic equilibrium configuration by oscillations of infinitesimal amplitude. Such self-gravitating oscillations satisfy the following linearized equations of momentum balance and gravitation (see Gilbert, 1980, for a recent discussion):

$$\nabla \cdot \sigma - \nabla(\rho g \mathbf{u} \cdot \hat{e}_r) - \rho \nabla \phi + g \nabla \cdot \rho \mathbf{u} \hat{e}_r = -\rho s^2 \mathbf{u} \tag{2.17}$$

$$\nabla^2\phi = -4\pi G\nabla \cdot \rho\mathbf{u} \tag{2.18}$$

The scalar fields $\rho(r)$ and $g(r)$ are the density and gravitational acceleration in the hydrostatic rest state, respectively; σ is the stress tensor, ϕ the associated perturbation of the gravitational potential, $\mathbf{u}$ the displacement vector, G the gravitational constant, and $\hat{e}_r$ an outward-pointing radial unit vector. The stress tensor in Eq. (2.17) is given by Eq. (2.13) with $\mu(s)$ specified by Eq. (2.15). In general the Laplace transform variable s is complex, so that $\mu(s)$ is complex also. In attacking the viscoelastic free oscillations problem in this fashion we are employing the so-called correspondence principle and in so doing following the same approach employed by Peltier (1974) in analysis of the isostatic adjustment problem. The method has very wide applicability.

We lose no important generality by seeking solutions to Eqs. (2.17) and (2.18) in the form

$$\mathbf{u} = \sum_{l=0}^{\infty}\left[U_l(r, s)P_l(\cos\theta)\hat{e}_r + V_l(r, s)\frac{\partial P_l}{\partial\theta}(\cos\theta)\hat{e}_\theta + W_l(r, s)\frac{\partial P_l}{\partial\theta}(\cos\theta)\hat{e}_\circ\right] \tag{2.19a}$$

$$\phi = \sum_{l=0}^{\infty}\phi_l(r, s)P_l(\cos\theta) \tag{2.19b}$$

in which $\hat{e}_\theta$ and $\hat{e}_\circ$ are unit vectors in the θ and ϕ directions, respectively, and P_l is the Legendre polynomial of degree l and order zero. Substitution of Eq. (2.19) into Eqs. (2.17) and (2.18), assuming that the physical properties of the earth model ρ, μ, and K are constant, reduces the field equations to two decoupled sets of first-order ordinary differential equations of the form

$$d\mathbf{X}/dr = \mathbf{B}\mathbf{X} \tag{2.20a}$$
$$d\mathbf{Y}/dr = \mathbf{A}\mathbf{Y} \tag{2.20b}$$

in which $\mathbf{X} = (W_l, T_{\phi l})^{\mathrm{T}}$, $\mathbf{Y} = (U_l, V_l, T_{rl}, T_{\theta l}, \phi_l, Q_l)^{\mathrm{T}}$, and $\mathbf{A}$ and $\mathbf{B}$ are reduced forms of the 2×2 and 6×6 matrices of coupling coefficients given by Gilbert (1980). The r- and s-dependent coefficients T_{rl}, $T_{\theta l}$, and $T_{\phi l}$ are those which appear in the spherical harmonic expansions of the σ_{rr}, $\sigma_{r\theta}$, and $\sigma_{r\phi}$ components of the stress tensor, and the Q_l are those which appear in the expansion of the auxiliary variable $q = \partial\phi/\partial r + (l + 1)\phi/r + 4\pi G\rho u_r$. The differential systems (2.20a,b) respectively govern the toroidal and spheroidal free oscillations. With $l = 0$ the spheroidal system describes the radial modes of free oscillation for which $V_0 = T_{\theta 0} = 0$ so that (ϕ_0, Q_0) decouple from U_0, $T_{\theta 0}$ and Eq. (2.20b) reduces to the second-order system

$$d\mathbf{Z}/dr = \mathbf{C}\mathbf{Z} \tag{2.20c}$$

where $\mathbf{Z} = (U_n, T_{rn})^{\mathrm{T}}$ and n is used to label the radial eigenstates.

Complex eigenvalues $s = s_r + is_i$ for the homogeneous systems (2.20) are determined from simultaneous zero crossings of the real and imaginary parts of the secular functions $D_j(s, l)$ associated with each set of equations. The secular functions are themselves determined by the boundary conditions at the earth's surface. From Takeuchi and Saito (1972), the secular function for the toroidal system (2.20a) is

$$D_1(s, l) = (l - 1)j_l(k, a) - kaj_{l+1}(k, a) \tag{2.21}$$

where $k_1 = [\rho_0/\mu(s)]^{1/2}$, a is the earth's radius, and ρ_0 is the average earth density. For the spheroidal system (2.20a) the characteristic equation is of the form

$$D_2(s, l) = \det \begin{bmatrix} T_{\theta l}^1 & T_{\theta l}^2 & T_{\theta l}^3 \\ T_{rl}^1 & T_{rl}^2 & T_{rl}^3 \\ Q_l^1 & Q_l^2 & Q_l^3 \end{bmatrix} \tag{2.22}$$

where the superscripts 1, 2, and 3 denote the three linearly independent solutions regular at the origin, each of which consists of a combination of two spherical Bessel functions $j_l(z)$ with different complex arguments z and a polynomial in r of degree l. Explicit expressions will also be found in Takeuchi and Saito (1972). The secular function for the radial system is also given in this reference as

$$D_3(s, n) = \frac{\tan k_2 a}{\mu(s)} - \frac{k_2 a}{\mu(s) - \frac{1}{4}[\lambda(s) + 2\mu(s)]k_2^2 a^2} \tag{2.23}$$

where

$$k_2(s) = \left[\rho_0 \frac{16(\frac{1}{3}\pi G)\rho_0 - s^2}{\lambda(s) + 2\mu(s)}\right]^{1/2}$$

Complex eigenspectra for the homogeneous earth model with properties listed in Table I have been calculated by Yuen and Peltier (1982) using the numerical methods developed for hydrodynamic stability analysis by Davis and Peltier (1976, 1977, 1979). We will discuss a small subset of their results in order to illustrate the points which most concern us here. Figure 3 shows free oscillation frequency $s_i = \omega$ as a function of angular degree l and overtone number n for the radial modes, spheroidal modes, and toroidal modes of a homogeneous model with either the simple Burgers body rheology, which has $\mu(s)$ given by Eq. (2.5d), or the generalized Burgers body rheology, which has $\mu(s)$ given by Eq. (2.15). The parameter ν_1 is fixed as $\nu_1 = 10^{21}$ Pa sec in both models. For the simple Burgers body, the short time scale viscosity ν_2 has been fixed by the requirement that the frequency of ${}_0S_2$ does not deviate substantially from the elastic frequency and that the

TABLE I. PHYSICAL PROPERTIES OF THE HOMOGENEOUS MODEL

Property	Symbol	Average value	Units
Density	ρ_0	5517	kg/m^3
s-Wave velocity	v_s	5130	m/sec
p-Wave velocity	v_p	10798	m/sec
Shear modulus	μ	1.4519×10^{11}	N/m^2
Comp. modulus	λ	3.5288×10^{11}	N/m^2
Surface gravity	g_s	9.82	m/sec^2
Radius	a	6.371×10^6	m

Q of ${}_0S_2$, where $Q \equiv s_r/2s_i$, is equal to 200. This requires that $\nu_2 \approx 10^{16}$ Pa sec (10^{17} P); μ_2 is chosen such as to make $\Delta = 0.03$. The parameters of the prototype absorption band have been fixed at $Q_m = 250$, $T_1 = 10^{-2}$ sec, and $T_2 = 10^4$ sec. With such low intrinsic dissipation, the free oscillation frequencies are not significantly affected by the deviation from perfect Hookean elasticity, as is well known. The necessity of choosing $\nu_2 \approx 10^{16}$ Pa sec in order to fit observed modal Q's (which are on the order of a few hundred; Anderson and Hart, 1978; Buland *et al.*, 1979; Sailor and Dziewonski, 1978) explains the value for this parameter which is marked on Fig. 1. In the case of absorption band anelasticity we can think of a continuous *spectrum* of short-term viscosities centered on this characteristic value.

Although the simple and generalized Burgers bodies are not distinguishable from one another through their predictions of free oscillation frequency, they are strikingly different in their predictions of modal Q. Figure 4 shows $Q = s_r/2s_i$ for a selection of radial, spheroidal, and toroidal modes for each of these models. The simple Burgers body with $\nu_2 = 10^{16}$ Pa sec predicts rapidly increasing Q with increasing modal frequency, whereas the absorption band model eliminates this extreme variation. Since observations of free oscillation Q's for the real earth cited above show no extreme variations of modal Q to exist, the single Debye peak of the simple Burgers body is not a valid description of mantle anelasticity and the generalized Burgers body must be employed. The predicted variations of Q with angular order and overtone number for this model shown in Fig. 4 are remarkably like those which have been observed for the stratified real earth. We note the sharp drop in Q along the radial-mode sequence from the fundamental mode to the first overtone, which is also characteristic of the observations (Buland *et al.*, 1979). We note also the local Q maxima along the spheroidal-mode overtone sequences, which are due to the relative partitioning of energy in the modes between shear and compression. This is also char-

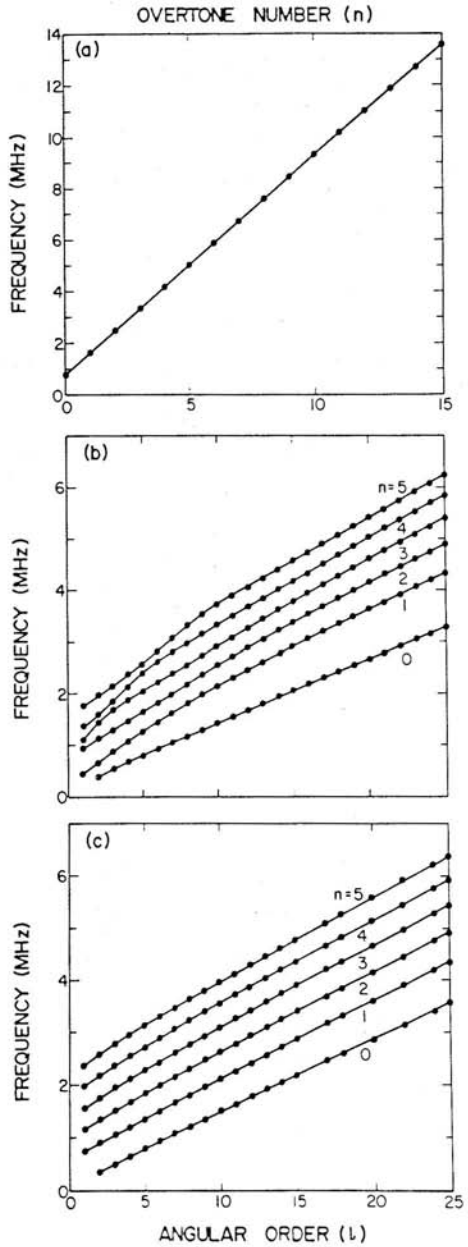

FIG. 3. Free oscillation frequency as a function of angular degree l and overtone number n for a sequence of (a) radial (${}_nS_0$), (b) spheroidal (${}_nS_l$), and (c) toroidal (${}_nT_l$) modes for a homogeneous spherical Burgers body model of the earth.

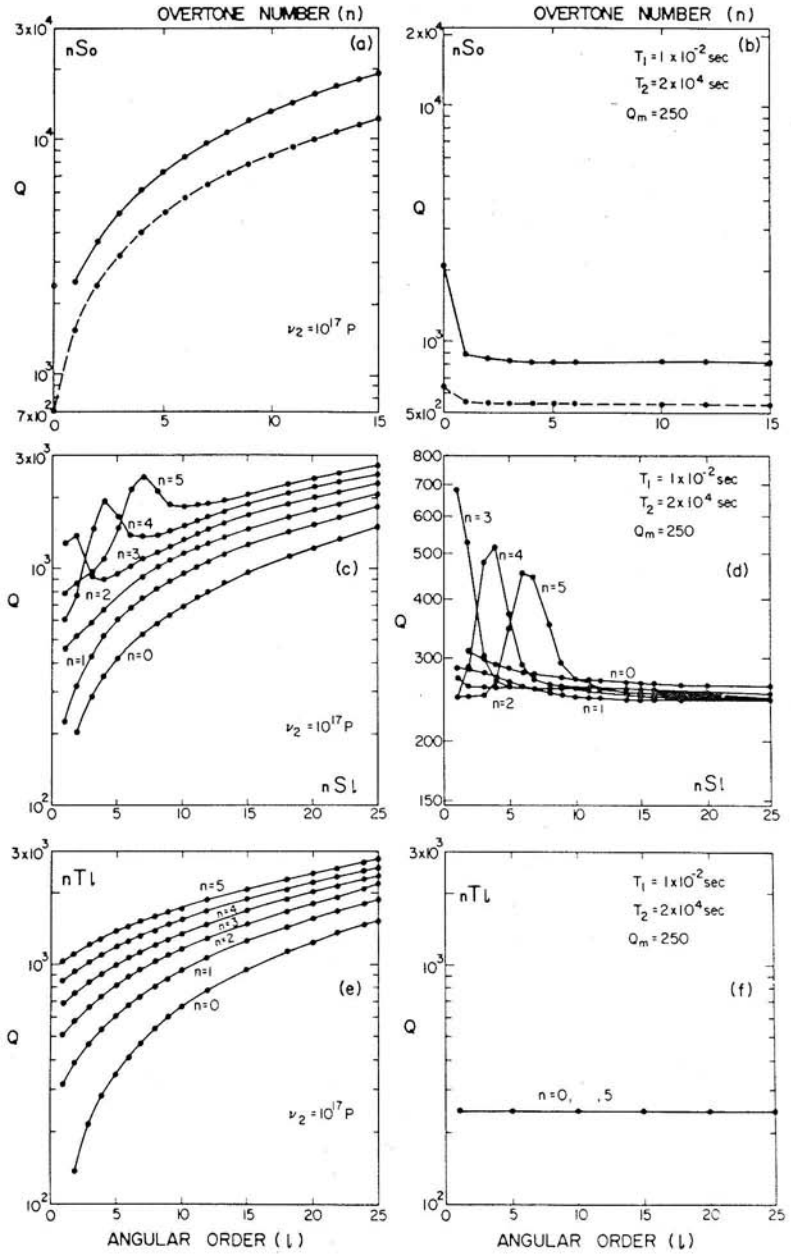

FIG. 4. Normal-mode Q as a function of angular degree l and overtone number n for the simple (a, c, e) and generalized (b, d, f) Burgers body rheologies for radial (${}_nS_0$), spheroidal (${}_nS_l$), and toroidal (${}_nT_l$) modes, respectively.

acteristic of the observations (Anderson and Hart, 1978). The interested reader will find a more detailed discussion of these calculations in Yuen and Peltier (1982).

For our present purposes the above abbreviated discussion suffices to establish that an absorption band description of the anelasticity of the mantle seems to be required to explain observations of free oscillation Q. Because of the magnitude of the long time scale viscosity ν_1 in the generalized Burgers body, it produces no influence upon the attenuation of high-frequency seismic oscillations. This is demonstrated in Table II, where we show a sequence of calculations comparing the Q's and periods of the mode ${}_0S_2$ for the absorption band model, with $\mu(s)$ defined in Eq. (2.12), with those for the generalized Burgers body, with $\mu(s)$ given by Eq. (2.15) as a function of the long time scale viscosity ν_1. Not unless ν_1 is less than 10^{17} Pa sec is the influence of its presence significant. Seismology is oblivious of the fact that the eventual behavior of the mantle is viscous.

As discussed in Peltier *et al.* (1981) and Yuen and Peltier (1982), the generalized Burgers body supports not only the weakly damped oscillatory modes of the free oscillation family, but also *two* families of quasi-static modes which lie on the negative real axis of the complex s plane. They are normal modes of viscous gravitational relaxation and exhibit exponentially decaying rather than oscillatory behavior in time. In Fig. 5 we show two schematic diagrams of the complex s plane, one for the simple and one for the generalized Burgers body. Both plots show the spheroidal modes of degree $l = 2$ for the prototype rheologies and include all of the free oscillations up to overtone number $n = 5$. The arrows show the displacement of the free oscillation eigenvalues off the imaginary s axis due to finite anelasticity. For the simple Burgers body (Fig. 5a), there are two additional modes on the negative real s axis. The first has a decay time of 15.94 hr and is supported by the anelastic component of the rheology, whereas the second has a decay time of approximately 10^3 yr and is supported by the viscous component. The first of these modes is marked by a solid circle and the latter by a cross near the origin $s = 0$. Because of the magnitude of their relaxation times, inertial forces play no role in the dynamics of these modes, and I therefore refer to them as quasi-static. The complex s plane for the generalized Burgers body (Fig. 5b) differs from that for the simple model only with respect to the nature of the short time scale quasi-static mode. For this generalized model, no such distinct mode exists, but rather there is a continuum of them ranging in relaxation time from the short time scale cutoff of the absorption band T_1 to the long time scale cutoff T_2. This is illustrated in Fig. 5b by the branch cut connecting the points $s_r = -1/T_1$ and $s_r = -1/T_2$. The quasi-static mode associated with the viscous response is imperceptibly shifted from its location for the simple Burgers body. All

TABLE II. COMPARISON OF PERIOD AND Q OF THE MODE ${}_0S_2$ FOR THE GENERALIZED BURGERS BODY RHEOLOGY (τ_B, Q_B) WITH THOSE FOR THE ABSORPTION BAND RHEOLOGY (τ_0, Q_0)

ν_1 (Pa sec)	$(Q_B - Q_0)/Q_0$ (%)	$(\tau_B - \tau_0)/\tau_0$ (%)
10^{21}	-6×10^{-4}	1×10^{-5}
10^{20}	-1×10^{-3}	3×10^{-5}
10^{19}	-2×10^{-3}	7×10^{-5}
10^{18}	-8×10^{-3}	4×10^{-4}
10^{17}	-3×10^{-1}	6×10^{-3}
10^{16}	-4×10	2×10^{-1}

of the quasi-static modes are viscous gravitational in nature and are supported by the density contrast across the free outer surface of the model. As we will see in the detailed discussion of the quasi-static viscous modes provided in Section 3, additional density discontinuities which exist in the radial structure of realistic earth models lead to the appearance of additional quasi-static modes. This turns out to have extremely important physical consequences in the theory of glacial isostasy, which is formulated in terms of the quasi-static viscous modes, and in fact explains the ability of our theory of this phenomenon to explain RSL and free-air gravity data simultaneously.

The discrete quasi-static modes supported by the anelasticity of the simple Burgers body and the continuum present in the generalized model have yet to be exploited in the understanding of geodynamic phenomena. It is in terms of these modes that the explanation of the phenomenon of postseismic rebound might be found, for example, though they have yet to be employed in this context. Much of the recent literature on this problem may err seriously, in my view, by attempting to describe the observed relaxation of the surface above the slip zone in terms of models which have Maxwell rheology below the lithosphere (Rundle and Jackson, 1977; Thatcher and Rundle, 1979; Cohen, 1980a,b). These models seem to require much lower values for the long time scale viscosity than those required to fit glacial rebound data. However, when SLS rheology is assumed to invert the postseismic uplift data, values of the short time scale viscosity ν_2 which are about 10^{16} Pa sec appear to be required (Yamashita, 1979; Nur and Mavko, 1974). This accords with the value required to fit seismic Q and that which fits the observed Q of the Chandler wobble (Scheidegger, 1957; Smith and Dahlen, 1981). As illustrated in Fig. 1, all geodynamic phenomena with time scales less than the Maxwell time of the mantle ($\sim$200 yr) should see only the anelastic component of the rheology. It is important to keep in mind that the short time scale and long time scale viscosities ν_2 and ν_1 are actual

material properties of the planet and not merely "factors" which appear in equally convenient Maxwell and SLS rheologies, which both predict exponential relaxation of harmonic loads. Although it is possible to fit postseismic rebound data with a Maxwell model by choosing an appropriate low value of the viscosity, this does not mean that this phenomenon is actually controlled by steady-state creep.

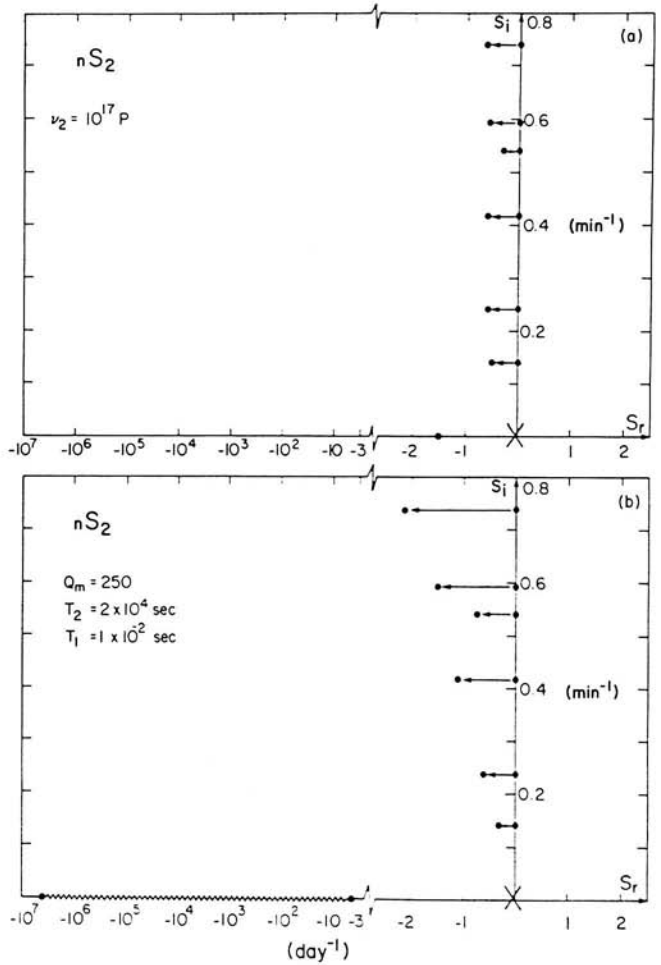

FIG. 5. Complex s plane for spheroidal modes $_nS_2$ for both the simple (a) and generalized (b) Burgers body rheologies. The earth model is homogeneous and the solid circles denote complex normal-mode frequencies supported by the anelastic component of the rheology. The crosses near the origin denote the imaginary frequency of the normal mode of viscous gravitational relaxation supported by the steady-state viscous component of the rheology.

2.3. *Viscous Gravitational Relaxation of a Homogeneous, Incompressible, and Spherical Burgers Body*

Because the eventual behavior of the generalized Burgers body is both viscous and incompressible, we may approximately determine the nature of the quasi-static viscous part of the complete normal mode spectrum of the earth model by neglecting compressibility at the outset. For such a model, the constitutive relation which replaces Eq. (2.13) is

$$\sigma_{ij} = \pi \delta_{ij} + 2\mu e_{ij} \tag{2.24}$$

Making use of the fact that $\nabla \cdot \mathbf{u} = 0$, the stress tensor can be shown to have divergence

$$\nabla \cdot \sigma = \nabla \pi - \mu \nabla \times \nabla \times \mathbf{u} \tag{2.25}$$

when the shear modulus μ is independent of spatial position. Since s is small for the quasi-static viscous modes (see Fig. 5), we may neglect the inertial force on the right-hand side of Eq. (2.17) and rewrite it, using $\partial_r \rho_0 = 0$ and $\nabla \cdot \mathbf{u} = 0$, in the form

$$-\nabla(\rho_0 \phi_1 + \rho_0 g_0 \mathbf{u} \cdot \mathbf{e}_r - \pi) - \mu \nabla \times \omega = 0 \tag{2.26}$$

where $\omega = \nabla \times \mathbf{u}$. The divergence of Eq. (2.26) is

$$(\rho_0/\mu)\nabla^2(\phi_1 + g_0 \mathbf{u} \cdot \mathbf{e}_r - \pi/\rho_0) = 0 \tag{2.27}$$

In the incompressible limit when the density is constant, Eq. (2.18) also reduces to the form

$$\nabla^2 \phi_1 = 0 \tag{2.28}$$

Spheroidal solutions to the system (2.27, 2.28) can be constructed by expanding $\mathbf{u}$ and ϕ as in Eq. (2.19) and π and ω as

$$\pi = \sum_{l=0}^{\infty} \pi_l(r, s) P_l(\cos \theta) \tag{2.29a}$$

$$\omega = \sum_{l=0}^{\infty} H_l(r, s)\, \partial_\theta P_l(\cos \theta) \hat{e}_\phi \tag{2.29b}$$

where $H_l = V_l + V_l/r - U_l/r$. Substitution in Eqs. (2.27) and (2.28) reduces them to

$$\nabla_r^2(\Phi_l + \xi r U_l - \pi_l/\rho_0) = 0 \tag{2.30}$$

$$\nabla_r^2 \Phi_l = 0 \tag{2.31}$$

where $\nabla_r^2(r^2 U_l) = (d^2 U_l/dr^2) + (2/r)(dU_l/dr) - l(l+1)(U_l/r^2)$. The radial component of Eq. (2.26) is also required and is

$$\frac{d^2(r^2U_l)}{dr^2} - l(l+1)U_l = \frac{\rho_0}{\mu} r^2 \frac{d}{dr}\left(\Phi_l + \xi r U_l - \frac{\pi_l}{\rho_0}\right) \tag{2.32}$$

Now the solutions to Eqs. (2.30) and (2.31) are

$$\Phi_l = C_3 r^l \tag{2.33}$$

$$\Phi_l + \xi r U_l - (\pi_l/\rho_0) = (\mu/\rho_0) C_1 r^l \tag{2.34}$$

Substitution of Eq. (2.34) into Eq. (2.32) then gives

$$U_l = [C_1 l/2(2l+3)] r^{l+1} + C_2 r^{l-1} \tag{2.35}$$

Given Φ_l, U_l, and π_l from Eqs. (2.33)–(2.35) in terms of the three unknown constants C_1, C_2, C_3 we may compute the tangential displacement amplitudes V_l, the normal stress amplitudes $T_{rl} = \pi_l + 2\mu U_l$, the tangential stress amplitudes $T_{\theta l} = \mu(V_l - V_l/r + U_l/r)$ and the amplitudes $Q_l = \Phi_l + (l+1)\Phi_l/r + 4\pi Q \rho_0 U_l$ of the auxiliary variable Q related to the radial derivative of the potential. In terms of a solution 6-vector $\mathbf{Y} = (U_l, V_l, T_{rl}, T_{\theta l}, \Phi_l, Q_l)^t$ the complete solution may then be represented as

$$\mathbf{Y} = \sum_{i=1}^{3} C_i \mathbf{y}_i \tag{2.36}$$

where

$$\mathbf{y}_1 = \left(\frac{l r^{l+1}}{2(2l+3)}, \frac{(l+3) r^{l+1}}{2(2l+3)(l+1)}, \frac{\rho_0 \xi l r^{l+2} + 2\mu r^l (l^2 - l + 3)}{2(2l+3)}, \right.$$
$$\left. \frac{2\mu l (l+2) r^l}{2(2l+3)(l+1)}, 0, \frac{3\xi l r^{l+1}}{2(2l+3)}\right)^t \tag{2.37a}$$

$$\mathbf{y}_2 = (r^{l-1}, r^{l-1}/l, \rho_0 \xi r^l + 2\mu(l-1) r^{l-2}, 2\mu(l-1) r^{l-2}/l, 0, 3\xi r^{l-1})^t \tag{2.37b}$$

$$\mathbf{y}_3 = (0, 0, \rho_0 r^l, 0, r^l, (2l+1) r^{l-1})^t \tag{2.37c}$$

The quasi-static spectrum for the incompressible homogeneous model may now be determined by applying homogeneous boundary conditions at the outer surface of the model. We insist that the tangential stress and the normal stress vanish and that the gradient of the potential perturbation be continuous, which give the boundary conditions

$$T_{rl}(a) = 0 \qquad T_{\theta l}(a) = 0 \qquad Q_l(a) = 0 \tag{2.38}$$

Application of these conditions at $r = a$ leads to three simultaneous homogeneous algebraic equations for the C_i in the form

$$\mathbf{MC} = 0 \tag{2.39a}$$

where the matrix $\mathbf{M}$ is

$$\mathbf{M} = \begin{bmatrix} \dfrac{\rho_0 \xi l a^{l+2} + 2\mu a^l (l^2 - l + 3)}{2(2l+3)} & \rho_0 \xi a^l + 2\mu(l-1)a^{l-2} & \rho_0 a^l \\ \dfrac{2\mu l(l+2)a^l}{2(2l+3)(l+1)} & \dfrac{2\mu(l-1)a^{l-2}}{l} & 0 \\ \dfrac{3\xi l a^{l+1}}{2(2l+3)} & 3\xi a^{l-1} & (2l+1)a^{l-1} \end{bmatrix} \tag{2.39b}$$

For a nontrivial solution we clearly require that the secular condition $\det \mathbf{M} = 0$ be satisfied. Since

$$\det \mathbf{M} = \frac{2\mu(s)(l-1)(2l+1)a^{3l-1}}{l(l+1)(2l+3)} [\rho_0 \xi l + \mu(s)(2l^2 + 4l + 3)]^{-2} \tag{2.40}$$

the eigenvalues of the homogeneous problem are either solutions of

$$\mu(s) = -\rho_0 l \xi a^2 / (2l^2 + 4l + 3) \tag{2.41}$$

or are the values of s which make $\mu(s) = 0$. Using $\mu(s)$ for the homogeneous Burgers body given by Eq. (2.15), the nonzero eigenvalues are obviously solutions of

$$\frac{\mu_1 s}{s + \mu_1/\nu_1} \left[1 + \frac{2}{\pi Q_m} \ln \frac{s + 1/T_2}{s + 1/T_1} \right] = - \frac{\rho_0 l \xi a^2}{(2l^2 + 4l + 3)} \tag{2.42}$$

Since the Maxwell time $T_m = \nu_1/\mu_1$ is such that $T_m \gg T_1 (T_2)$ there will be a simple root

$$s^l = \left(\frac{\mu_r}{\mu_1} \nu_1 \frac{2l^2 + 4l + 3}{\rho_0 l g_0 a} + \frac{\nu_1}{\mu_1} \right)^{-1} \tag{2.43}$$

on the negative real axis of the complex s plane (where μ_r is the relaxed elastic modulus). Since the modulus defect is small, $\mu_r/\mu_1 \approx 1$, and s^l may be approximated as

$$s^l = \left(\nu_1 \frac{2l^2 + 4l + 3}{\rho_0 l g_0 a} + \frac{\nu_1}{\mu_1} \right)^{-1} \tag{2.44}$$

A fundamental property of the earth is that

$$(s^{Vl})^{-1} = \nu_1 \frac{2l^2 + 4l + 3}{\rho_0 l g_0 a} \gg \frac{\nu_1}{\mu_1} = T_m \tag{2.45}$$

for sufficiently large l. Since the factor on the left-hand side of the inequality (2.45) is just the relaxation time for a homogeneous Newtonian viscous sphere (Peltier, 1974), we therefore see that the reason why the earth may be approximated as a Newtonian viscous fluid for the purpose of analyzing

TABLE III. COMPARISON OF s^{-l} AND $s^{-\nu l}$ FOR VARIOUS VALUES OF l AND A HOMOGENEOUS EARTH

l	s^{-l}	$s^{-\nu l}$	Percentage difference
2	−0.9165	−1.1458	25
4	−0.7196	−0.8537	18
6	−0.5766	−0.6597	14
8	−0.4784	−0.5342	10
10	−0.4080	−0.4479	10
50	−0.1023	−0.1046	2
100	−0.0527	−0.0534	1
500	−0.0108	−0.0108	<0.1

the rate at which surface deformations relax under the gravitational force is due to the small value of the nondimensional parameter

$$P = \frac{\rho_0 l g_0 a}{\mu_1 [2l^2 + 4l + 3]} \tag{2.46}$$

which clearly does not involve the viscosity. In Table III we compare $(s^l)^{-1}$ with $(s^{\nu l})^{-1}$ for various values of l and a homogeneous earth with $\rho_0 = 5517$ kg/m^3, $a = 6.371$ km, $g_0 = 9.82$ m sec^{-2}, $\mu_1 = 1.4519 \times 10^{11}$ N/m^2. Inspection of this table shows that the elastic correction to the viscous decay time is at most 25% and obtains for the smallest value of l shown. For $l = 10$ the difference is reduced to 10%. These results show that although elastic–viscous coupling contributes significantly in determination of the rate of decay of harmonic surface irregularities, the viscous approximation is nevertheless not an unreasonable one insofar as the computation of decay times is concerned.

We will conclude this subsection by demonstrating the way in which Eq. (2.44) may be employed to estimate the steady-state viscosity of the planetary mantle. Figure 6 shows a photograph of a flight of raised beaches located in the Richmond Gulf of Hudson Bay near the center of the Laurentide rebound. The relict beaches remain very well exposed at this site, as they do throughout much of the Canadian Arctic and sub-Arctic. For this reason they are in many ways much easier to collect data from than is found to be the case in Europe, where much of the region of uplift is quite heavily populated. Figure 7 shows the RSL data for this site, with the individual data points shown as crosses and dots and with the height of each beach in the sequence plotted as a function of its age in sidereal years (corrected ^{14}C dates). The solid curve on this figure is the prediction of a model which will be discussed later. In Fig. 8 the data are replotted on a

FIG. 6. Flight of raised beaches located in the Richmond Gulf of Hudson Bay.

log–linear diagram on which they would appear as a straight line if the relaxation were perfectly exponential. The solid line on this figure is the best-fit straight line to the data for the last 5000 yr, during which time we can be fairly sure that the vertical motion was essentially free decay, since most of the surface ice had by that time disappeared. The slope of this straight line gives a relaxation time at this site of approximately 1760 yr. Since the Laurentide ice sheet had a radius of approximately 15°, its relaxation spectrum is dominated by harmonic degree $l = 6$. If we substitute $(s^l)^{-1} = 1760$ yr and $l = 6$ in Eq. (2.44) and solve for the viscosity, we obtain $\nu_1 \approx 10^{21}$ Pa sec (10^{22} P), which demonstrates in a completely uncomplicated way how this number is obtained.

2.4. The Phenomenological Utility of the Generalized Burgers Body

The brief discussion in the preceding subsections should be seen as an argument in favor of the phenomenological utility of a particular viscoelastic rheology which appears to be uniformly valid in time. The generalized Burgers body has 5 parameters (μ_1, ν_1, T_1, T_2, and Q_m), which along with the density ρ are to be determined by fitting the model to geophysical observations such as the elastic gravitational free oscillations and postglacial rebound. In this phenomenological approach, what one hopes to do is fix

all of the parameters of the model by fitting a subset of the totality of geodynamic observations and then check the validity of the model so determined by predicting other geophysical observables. An example of this approach applied to the short time scale parameters is to fix T_1, T_2, and $Q_m(r)$ using free oscillation data and then use the model to predict the Q of the Chandler wobble; an analysis of this sort has been completed by Smith and Dahlen (1981). A second example applied to the long time scale parameters is to use postglacial rebound to fix $\nu_1(r)$ and then use ν_1 in mantle convection models of the sea-floor spreading process. A discussion of this idea has been given by Peltier (1980b).

It should be recognized, however, that the above approach *is* purely phenomenological in that there is no guarantee that the constitutive relation which we employ can be given rigorous microphysical justification. What we would eventually like to accomplish is a direct derivation of this relation from solid-state physical principles concerned, for example, with the dynamics of dislocations. The macroscopic approach which we have elected to take will nevertheless provide rather clear guidelines which will have to be accommodated by any successful microphysical model. One might make the obvious analogy here with simple liquids. Although one cannot, for liquids, directly derive the Navier–Stokes equations which describe their macroscopic behavior from *simple* statistical-mechanical first principles (which can be done for gases), this does not make the Navier–Stokes

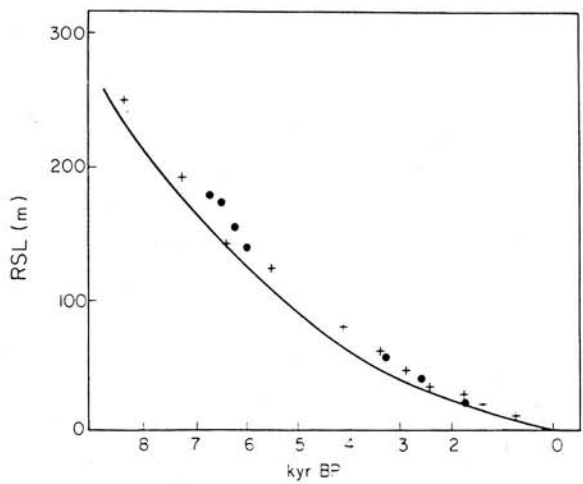

FIG. 7. Relative sea level curve obtained from radiocarbon-dated beach material in the sequences shown in Fig. 6. Ages have been corrected to give proper sidereal age; the solid curve is the prediction of a theoretical model.

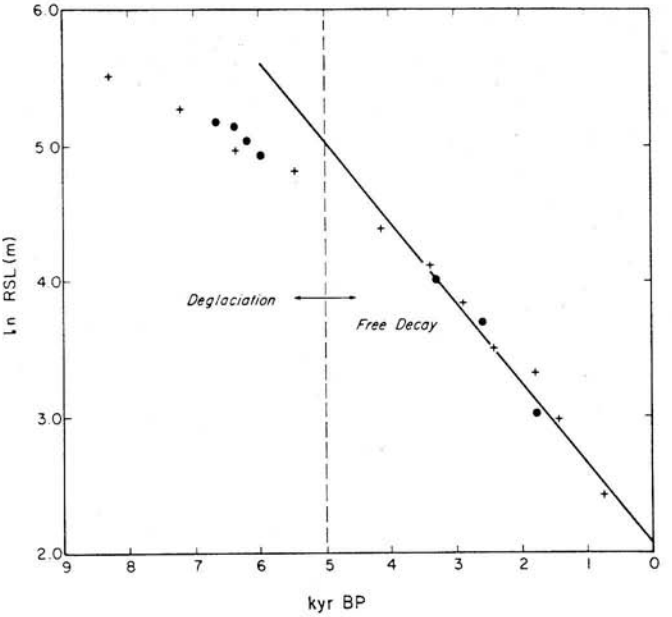

FIG. 8. Log–linear plot of the RSL data shown in Fig. 7.

equations less useful for describing the macroscopic motion of liquids. Neither does it make the measured viscosities of liquids less useful physical parameters.

In the next section we shall go on to apply the low-frequency limiting form of our general rheological model to develop the theory of glacial isostatic adjustment.

3. THE IMPULSE RESPONSE OF A MAXWELL EARTH

In the limit of low frequency, the generalized Burgers body developed in the last section reduces to a Maxwell solid with frequency-dependent Lamé parameters given essentially by Eq. (2.5b), although the parameter μ_1 which appears in the numerator of the expression for $\mu(s)$ should be replaced by the relaxed shear modulus μ_R. Since the elastic defect is small, however, which it must be to fit seismic observations, we may safely neglect this effect in constructing a model for glacial isostatic adjustment. This argument justifies use of the Maxwell constitutive relation

$$\sigma_{ij} = \lambda(s) e_{ii}\, \delta_{ij} + 2\mu(s) e_{ij} \tag{3.1}$$

with

$$\lambda(s) = \frac{\lambda s + \mu K/\nu}{s + \mu/\nu} \tag{3.2a}$$

$$\mu(s) = \frac{\mu s}{s + \mu/\nu} \tag{3.2b}$$

where we have now dropped the subscript 1 on λ and μ, which denotes the instantaneous elastic value, and on ν, which distinguishes it as the long time scale parameter. In constructing our model of glacial isostatic adjustment we will assume that the elastic Lamé parameters λ and μ are known functions of radius determined by the systematic inversion of body wave and free oscillations data and that $\nu(r)$ is to be determined by fitting the model to isostatic adjustment observations.

3.1. *The Observed Elastic Structure of the Planet and Its Physical Interpretation*

In Fig. 9a we show a representative spherically averaged elastic earth model which fits a large fraction of the seismic data set. The parameters which describe this model are λ and μ and the density field ρ, which in the

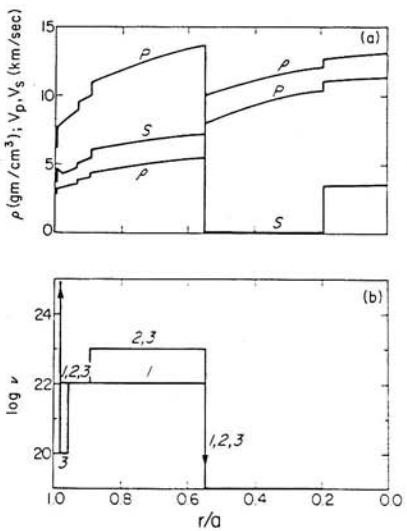

FIG. 9. (a) Radial elastic structure of model 1066B of Gilbert and Dziewonski (1975). Note the presence of discontinuities of the elastic parameters at depths of 420 and 670 km associated with solid–solid phase transformations. (b) Several of the mantle viscosity models which are discussed in the text.

figure have values equal to those in model 1066B of Gilbert and Dziewonski (1975). Actually, we have not shown λ and μ individually in this figure, but rather have given the velocities $V_p = \sqrt{(\lambda + 2\mu)/\rho}$ and $V_s = \sqrt{\mu/\rho}$ of longitudinal and transverse elastic waves, respectively. Inspection of this figure clearly reveals the major regions into which the planetary interior may be divided: the small solid inner core; the liquid outer core, in which $V_s = 0$; the lower mantle, beneath 670 km depth, throughout which V_p, V_s, and ρ increase smoothly; the transition region marked by the presence of two discontinuities in V_p and V_s at about 420 and 670 km depth (the deepest of which has a somewhat larger associated density jump); the upper mantle, between about 30 and 420 km depth, in which the physical properties also change smoothly; and finally the crust, which extends to about 30 km depth (above the so-called Mohorovičic discontinuity), in which the density is low and seismic wave speeds are slower than in the underlying mantle.

The physical explanations of the major divisions of the interior have been well understood for some time. The most important division, that between core and mantle, is clearly chemical in origin, the mantle being essentially a mixture of iron and magnesium silicates and the core consisting of a mixture of iron alloyed with some lighter element (e.g., Jacobs, 1975). The density jump between the solid inner core and the liquid outer core contains a small contribution due to the fact that the light alloying element is expelled into the melt as the solid inner core freezes; this idea is useful to dynamo theorists, since the process is expected to drive a compositional convection which would provide an extremely efficient energy source for the geomagnetic field (Braginski, 1963; Loper and Roberts, 1978).

Only rather recently has a fully satisfactory explanation of the seismic discontinuities at 420 and 670 km depth in the mantle been provided. Although Ringwood and Major (1970) showed by direct high-pressure experiment that the 420-km boundary was due to a solid–solid phase transition of the low-pressure phase olivine to the high-pressure spinel structure, only very recently (Yagi *et al.*, 1979) has high-pressure diamond anvil technology advanced to the extent that the regime of higher pressures (and greater depths) could be assessed directly with experiments in which thermodynamic equilibrium prevails. In Fig. 10 we show a phase equilibrium diagram from Jeanloz (1981) for the system $(Mg, Fe)_2SiO_4$ as a function of pressure at a fixed temperature of $T = 1000°C$. Inspection of this figure clearly shows that the 670-km discontinuity is also due to a phase change, in this case from spinel to a mixture of perovskite + magnesiowustite. Data discussed in Yagi *et al.* (1979) show that the increase in density which occurs in this transition is just that which is required to explain the seismically observed increase. As explained in Jeanloz (1981), the olivine $\rightarrow$ spinel and

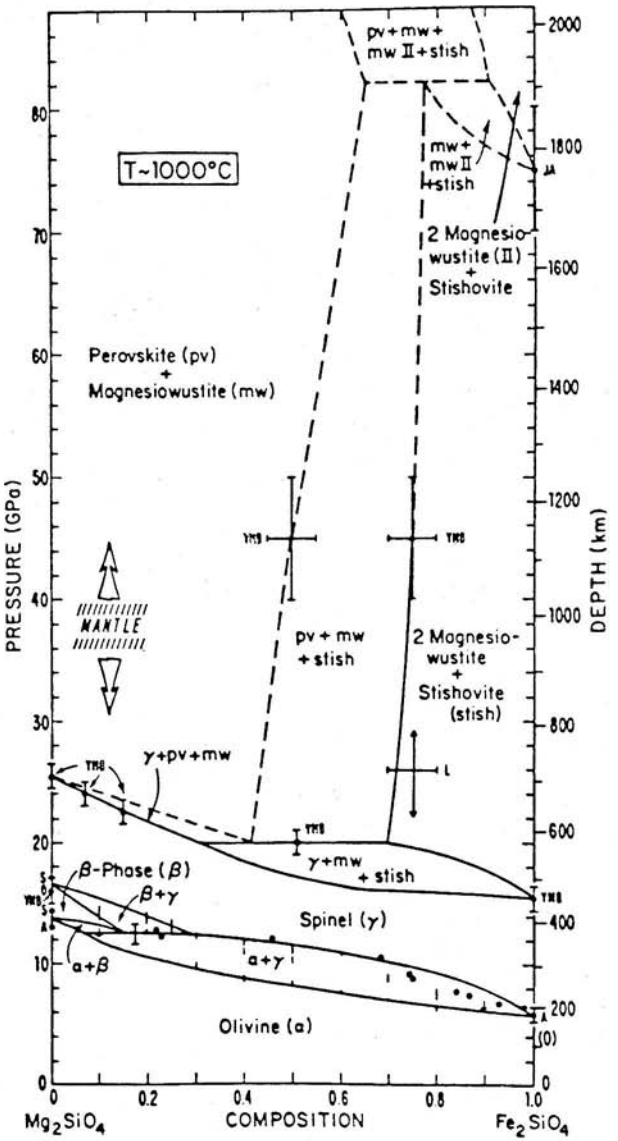

FIG. 10. Phase equilibrium diagram for the system $(Mg, Fe)_2SiO_4$ as a function of pressure (depth) (from Jeanloz, 1981.) The composition corresponding to the earth's mantle is shown on the figure.

spinel → perovskite + magnesiowustite transitions are fundamentally different. The former involves no change in the atomic packing configuration, whereas the latter is a true high-pressure transformation in the sense that such a change of coordination does occur. In my view, these new data may severely undermine the idea which has been prevalent in the geophysical literature for some time (e.g., Anderson, 1981) that there is a significant change of mean atomic weight (i.e., chemistry) across this boundary. Most of what we know about the mantle suggests that it is very nearly homogeneous chemically. The only apparent exception to this is the recent information on the degree of mantle mixing which has been derived from studies of the Rb–Sr and Nd–Sm isotopic systems which seem to suggest that the mantle consists of two fairly distinct isotopic reservoirs, one of which is essentially "primitive" in its content of radioactive elements and the other of which is essentially depleted. Given preexisting ideas in the literature to the effect that the 670-km discontinuity is a chemical boundary, it is perhaps not surprising that geochemists have tended to associate the primitive reservoir with the lower mantle and the depleted reservoir with the upper mantle, although their data give no direct information concerning the location of these apparently required reservoirs. The last of the boundaries evident in the spherically averaged model shown in Fig. 9, that between crust and mantle, is clearly influenced to a nonnegligible degree by lateral heterogeneity connected with differences between oceans and continents. Such lateral heterogeneity of the near-surface elastic structure should not be too important to viscoelastic relaxation, however, since all of this heterogeneity is contained in the low-temperature, high-viscosity lithosphere in which flow may occur only on extremely long time scales.

3.2. *Formulation of the Viscoelastic Problem for Models with Radial Heterogeneity*

In order to describe the viscoelastic response of realistic earth models with the rather complicated elastic structure shown in Fig. 9, we are forced to extend the discussion in Section 2.3 considerably, both to include strong radial heterogeneity of ρ and μ and to include the effect of finite λ (compressibility). The mathematical problem is that posed by the linearized versions of Eqs. (2.17) and (2.18) in the quasi-static limit, which we will rewrite for convenience as

$$\nabla \cdot \sigma - \nabla(\rho g \mathbf{u} \cdot \mathbf{e}_r) - \rho_0 \nabla \phi_1 - g_0 \rho_1 \hat{e}_r = 0 \tag{3.3}$$

$$\nabla^2 \phi_1 = 4\pi G \rho_1 \tag{3.4}$$

where the density perturbation ρ_1 is obtained from the linearized continuity equation as

$$\rho_1 = -\rho_0 \nabla \cdot \mathbf{u} - \mathbf{u} \cdot (\partial_r \rho_0) \hat{e}_r \tag{3.5}$$

The momentum equation (3.3) has been linearized with respect to perturbations from a background hydrostatic equilibrium configuration (ρ_0, p_0, ϕ_0) which satisfies

$$\nabla p_0 = -\rho_0 g_0 \hat{e}_r \tag{3.6a}$$

$$\nabla^2 \phi_0 = 4\pi G \rho_0 \tag{3.6b}$$

In Eqs. (3.3) and (3.4) the gravitational potential perturbation ϕ_1 will in general be the sum of two parts, ϕ_2 and ϕ_3, which are respectively the potential of any externally applied gravitational force field (the load) and that due to the internal redistribution of mass effected by the load-induced deformation.

We will require solutions to Eqs. (3.3) and (3.4) which describe the deformation of the radially stratified planet induced by surface loading. Since the response to an arbitrary load can be obtained by convolution with an appropriate point-load Green's function and since symmetry considerations demand that this response depend only upon r, s, and the angular distance from the point load θ, fundamental solutions are spheroidal and have the following vector harmonic decompositions:

$$\mathbf{u} = \sum_{l=0}^{\infty} \left(U_l(r, s) P_l(\cos\theta) \hat{e}_r + V_l(r, s) \frac{\partial P_l}{\partial \theta}(\cos\theta) \hat{e}_\theta \right) \tag{3.7a}$$

$$\phi_1 = \sum_{l=0}^{\infty} \Phi_l(r, s) P_l(\cos\theta) \tag{3.7b}$$

$$\nabla \cdot \mathbf{u} = \sum_{l=0}^{\infty} \chi_l(r, s) P_l(\cos\theta) \tag{3.7c}$$

Substitution of Eq. (3.7) into Eq. (3.3) reduces these field equations to the following set of three simultaneous second-order equations:

$$\ddot{\Phi} + \frac{2}{r}\dot{\Phi} - \frac{l(l+1)}{r^2}\Phi = -4\pi G(\rho_0 \chi + \dot{\rho}_0 U) \tag{3.8a}$$

$$0 = -\rho_0 \dot{\Phi} + \rho_0 g_0 \chi - \rho_0 \, d(g_0 U)/dr + d(\lambda\chi + 2\mu\dot{U})/dr + (\mu/r^2)4r\dot{U} - 4U + l(l+1)(3V - U - r\dot{V}) \tag{3.8b}$$

$$0 = -\rho_0 \Phi - \rho_0 g_0 U + \lambda\chi + r\frac{d}{dr}\left[\mu\left(\dot{V} - \frac{V}{r} + \frac{U}{r}\right)\right] + (1/r)[5U + 3r\dot{V} - V - 2l(l+1)V] \tag{3.8c}$$

in which the dot denotes differentiation with respect to r and

$$\chi = \dot{U} + \frac{2}{r}U - \frac{l(l+1)}{r}V \tag{3.8d}$$

$$\dot{g}_0 + (2/r)g_0 = 4\pi G\rho_0 \tag{3.8e}$$

in all of which it is understood that U, V, Φ, χ, λ, and μ stand for $U_l(r, s)$, $V_l(r, s)$, $\Phi_l(r, s)$, $\chi_l(r, s)$, $\lambda(r, s)$, and $\mu(r, s)$, respectively. Equations (3.8a–c) may be rewritten as a set of simultaneous first-order equations in terms of a vector $\mathbf{Y}$, the elements of which are

$$\mathbf{Y} = (U_l, V_l, T_{rl}, T_{\theta l}, \Phi_l, Q_l)^{\mathrm{t}} \tag{3.9}$$

where

$$T_{rl} = \lambda\chi_l + 2\mu\dot{U}_l \qquad T_{\theta l} = \mu\left(\dot{V}_l - \frac{1}{r}V_l + \frac{1}{r}U_l\right) \tag{3.10}$$

$$Q_l = \dot{\Phi}_l + \frac{(l+1)}{r}\Phi_l + 4\pi G\rho_0 U_l$$

$$d\mathbf{Y}/dr = \mathbf{A}\mathbf{Y} \tag{3.11}$$

where the elements of the $\mathbf{A}$ matrix are

$$a_{1i} = (-2\lambda/r\beta,\ l(l+1)\lambda/r\beta,\ 1/\beta,\ 0,\ 0,\ 0) \tag{3.12a}$$

$$a_{2i} = (-1/r,\ 1/r,\ 0,\ 1/\mu,\ 0,\ 0) \tag{3.12b}$$

$$a_{3i} = \left(\frac{4}{r}\left[\frac{\gamma}{r} - \rho_0 g_0\right],\ -\frac{l(l+1)}{r}\left[\frac{2\gamma}{r} - \rho_0 g_0\right],\ -\frac{4\mu}{r\beta},\ \frac{l(l+1)}{r},\ -\frac{\rho_0(l+1)}{r},\ \rho_0\right) \tag{3.12c}$$

$$a_{4i} = \left(\frac{1}{r}\left[\rho_0 g_0 - \frac{2\gamma}{r}\right],\ -\frac{1}{r^2}[2\mu - l(l+1)(\gamma+\mu)],\ -\frac{\lambda}{r\beta},\ -3/r,\ \rho_0/r,\ 0\right) \tag{3.12d}$$

$$a_{5i} = (-4G\rho_0,\ 0,\ 0,\ 0,\ -(l+1)/r,\ 1) \tag{3.12e}$$

$$a_{6i} = \left(-4\pi G\rho_0[(l+1)/r],\ 4\pi G\rho_0 l(l+1)/r,\ 0,\ 0,\ 0,\ \frac{l-1}{r}\right) \tag{3.12f}$$

where

$$\beta = \lambda(r, s) + 2\mu(r, s) \tag{3.13a}$$

$$\gamma = \mu(r, s)\,\frac{3\lambda(r, s) + 2\mu(r, s)}{\lambda(r, s) + \mu(r, s)} \tag{3.13b}$$

Now the solution 6-vector which solves Eq. (3.11) may be represented quite generally as a linear superposition of six linearly independent solutions. The combination coefficients in this linear superposition are determined by the boundary conditions at the endpoints of the domain $0 \le r \le a$. Three of the required six boundary conditions are that U, V, and Φ be regular at the origin $r = 0$. The remaining boundary conditions depend upon the physical

conditions which obtain at $r = a$. In Section 2.3 we assumed homogeneous boundary conditions Eq. (2.38) at $r = a$ and deduced an analytic expression for the relaxation spectrum of the incompressible model with constant physical properties. In the next subsection we will discuss the properties of the relaxation spectrum of realistic earth models with elastic structure fixed to that shown in Fig. 9.

3.3. *Normal Modes of Viscous Gravitational Relaxation*

When the effect of radial stratification of the earth model is included, the elements of the secular matrix **M** in Eq. (2.39b) must be determined numerically. In order to do this, we proceed by integrating the system of equations (3.11) for each harmonic degree l from the center of the earth to its surface. We employ a standard "parallel shooting" method, in which the system is integrated from depth to the surface using three linearly independent starting vectors determined from the three linearly independent solutions which solve Eq. (3.11) for a homogeneous compressible sphere. These solutions are given explicitly in Wu and Peltier (1982a). As l increases, the starting depth is decreased and the properties of the homogeneous sphere which determine the starting solution are taken equal to those at the starting depth. Propagation of each of the linearly independent solutions to the surface $r = a$ generates values of T^j_{rl}, $T^j_{\theta l}$, and Q^j_l where $j = 1, 3$ denotes the number of the "shot." For homogeneous boundary conditions (2.38), it then follows from the linearity of the differential equations that the secular condition is given by

$$D_2(s, l) = 0 \tag{3.14}$$

where $D_2(s, l)$ is as defined in Eq. (2.22). The similarity between the problem of viscous gravitational relaxation and the problem of spheroidal free oscillation is therefore further reinforced. As pointed out previously, the totality of the normal-mode frequencies are represented as points in the complex s plane. In such a representation the quasi-static modes appear as points on the negative real s axis as shown previously in Fig. 5a,b and therefore have frequencies which are purely imaginary. Figure 11 shows a plot of the secular function $D_2(s, l)$ for $l = 6$ and for an earth model whose viscosity profile is shown in Fig. 9b as model 1 and whose elastic structure is as in Fig. 9a. The entire core is taken to have zero viscosity, the viscosity of the mantle is 10^{21} Pa sec (10^{22} P, ν is in poise in the figure) throughout, and the model has a 120-km-thick lithosphere in which ν is infinite. Inspection of Fig. 11 shows that for fixed l there are several modes for a given value of l rather than one as was found for the homogeneous earth model.

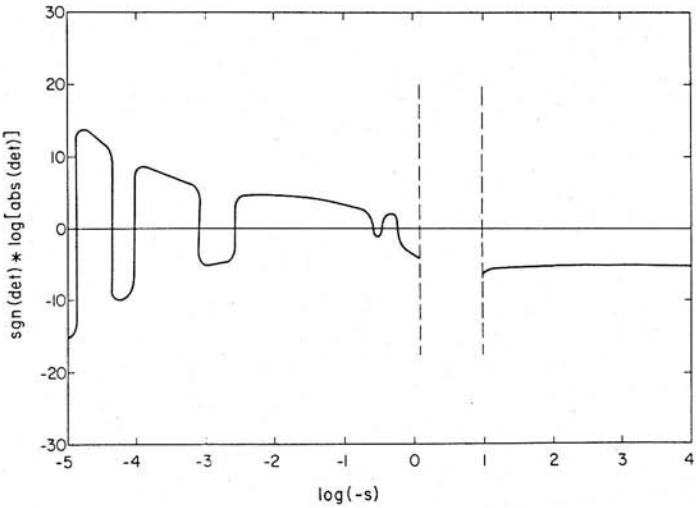

FIG. 11. The secular function for the spheroidal system for angular degree $l = 6$ as a function of the Laplace transform variable s.

Relaxation diagrams for all three of the viscosity models shown in Fig. 9b are shown in Fig. 12a,b,c (from Wu and Peltier, 1982a). On these diagrams we have plotted on a log–log scale the inverse relaxation time of each mode as a function of spherical harmonic degree l. Relaxation times have been nondimensionalized with a nominal time of 10^3 yr, so that where $\log(-s) = 0$ the relaxation time is 10^3 yr, whereas where $\log(-s) = -1$ the relaxation time is 10^4 yr. Visible on each of these three plates are six modal branches, which are marked L0, M0, M1, M2, C0, and C1. These distinct branches are analogous to the various body wave and surface wave branches which are visible on the dispersion diagram for the elastic gravitational free oscillations (e.g., Gilbert and Dziewonski, 1975) in that they owe their existence to specific physical properties of the radially stratified viscoelastic earth model. The M0 branch is the fundamental mode of the mantle, which corresponds to the single mode which exists in the homogeneous earth model discussed in Section 2.3. However, along this branch the relaxation time does not increase continuously with increasing spherical harmonic degree as predicted by Eq. (2.44) for the homogeneous model. Rather, for angular order l greater than about 30, relaxation time decreases with increasing l. This effect is due to the presence of the lithosphere and was first demonstrated by McConnell (1968) for half-space models. McConnell discovered this characteristic behavior in his deconvolution of Sauramo's (1958) shoreline data and used it to measure the thickness of the lithosphere.

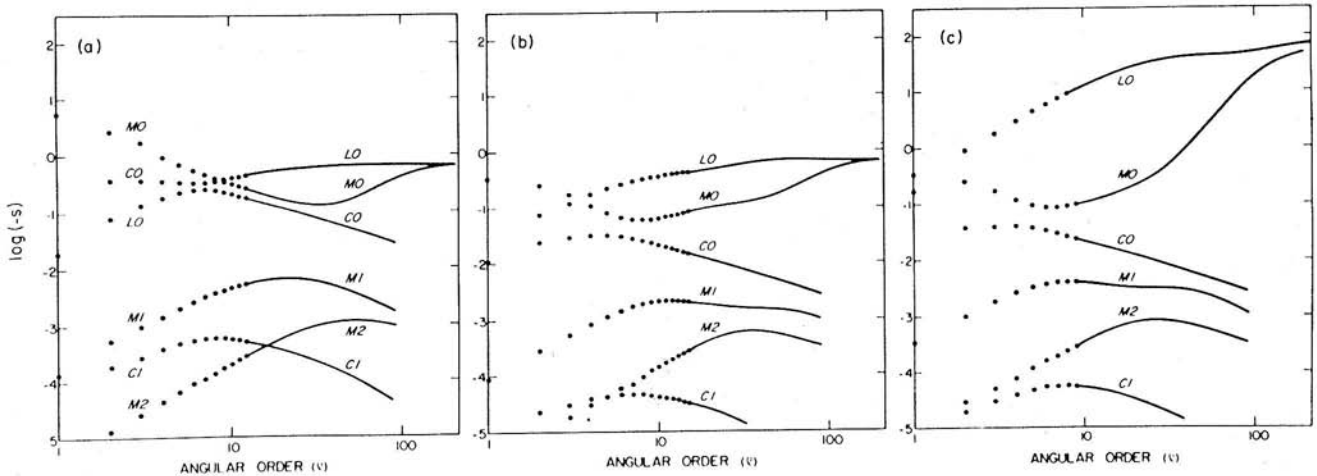

FIG. 12. Relaxation diagrams for viscosity models 1, 2, and 3 shown in Fig. 9b are shown in parts (a), (b), and (c), respectively. The elastic structure is that of model 1066B shown in Fig. 9a.

As well as altering the fundamental-mode relaxation curve in this way, the presence of the lithosphere also introduces a second modal branch, which is labeled L0 in the figures. As discussed in Wu and Peltier (1982a), the modes along this branch are not efficiently excited in general and so play no substantial role in viscoelastic deformation. At large l the M0 and L0 modal lines converge, and this is simply a mathematical manifestation of the physical fact that for sufficiently short wavelength (large l) all viscoelastic relaxation is suppressed, since such short-wavelength disturbances are completely controlled by the perfectly elastic lithosphere. The C0 branch on each of the modal diagrams is supported by the density contrast across the core–mantle boundary, and inspection of the relaxation diagrams shows that the M0, L0, and C0 branches are more closely interleaved for the uniform viscosity model (Fig. 12a) than they are for the other models which have moderately high lower mantle viscosity (Fig. 12b,c). In fact, in both the models with high lower mantle viscosity (models 2 and 3 of Fig. 9b) the relaxation times along the C0 branch are very nearly one order of magnitude larger than they are in the uniform viscosity case. This may be simply understood in terms of the variational principle derived in Peltier (1976). Since the core mode is sensitive only to lower mantle viscosity and since the lower mantle viscosity is one order of magnitude greater in models 2 and 3 than it is in model 1, the relaxation times for this mode are increased by one order of magnitude according to the variational formula. The remaining modes M1, M2, and C2 on this diagram have considerably larger relaxation times than do the modes M0, L0, and C0. Modes M1 and M2 are supported by the density jumps across the 670-km and 420-km discontinuities, respectively, whereas C1 is supported by the density contrast between the inner and outer cores. Of this sequence of long relaxation time modes, M1 is by far the most important, since it is the most efficiently excited by surface loading (Wu and Peltier, 1982a). It is at least in part a consequence of the excitation of this mode that models with uniform mantle viscosity are able to reconcile free-air gravity and RSL data simultaneously, as we shall see.

In Fig. 13 we have plotted relaxation time versus angular order for the fundamental mantle modes M0 of each of the previously discussed viscosity models numbered 1–3 in Fig. 9b. Also shown is the corresponding modal curve for a model numbered 4, which differs from 3 only in that the viscosity in the sublithospheric low-viscosity zone is 10^{20} Pa sec (10^{21} P) rather than 10^{19} Pa sec (10^{20} P). Superimposed upon these modal curves are hatched regions denoting observational estimates by various authors of the relaxation times for specific spatial scales. Also included is the $\tau(k_H)$ spectrum deduced by McConnell (1968) from Sauramo's shoreline data, which must, however, be considered unreliable at both the longest and shortest relaxation times.

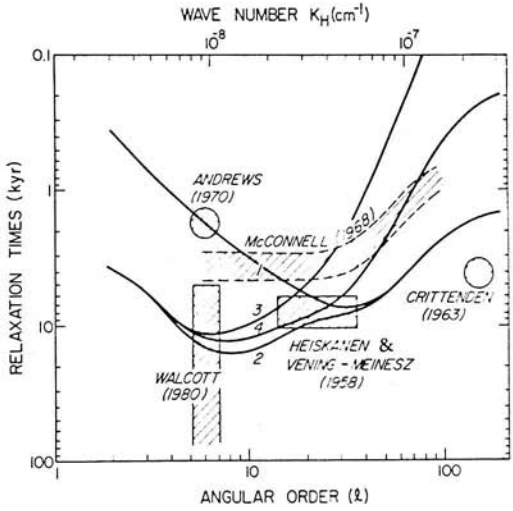

FIG. 13. Relaxation time versus angular degree for the sequence of viscoelastic earth models discussed in the text. The hatched regions represent estimates of relaxation times for specific horizontal scales by the authors noted.

The greatest disagreement evident in this diagram is that between Andrews (1970) and Walcott (1980) concerning the relaxation time for the $l = 6$ harmonic, which is deduced from the observed uplift of Hudson Bay after removal of the Laurentide load. Andrews's estimate of the relaxation time is based upon the shoreline data from the Ottawa Islands and some other locations and is between 1700 and 1900 yr. Our analysis in Section 2.3 of the Richmond Gulf data of Hillaire-Marcel and Fairbridge (1978) gave a relaxation time of 1760 yr and therefore agrees with Andrews's. Walcott's (1980) estimate is from a site near the Ottawa Islands and is based upon radiocarbon ages of shells and shell fragments of a single species (*Mytilus edulis*). He claims that the shortest relaxation time allowed by the data is about 4000 yr but that the actual relaxation time could be very much longer (i.e., >10,000 yr). Inspection of Fig. 13 shows that the minimum difference of a factor of 2–4 between Andrews's and Walcott's estimates of the relaxation time of the $l = 6$ harmonic is the difference between the model with uniform mantle viscosity and the model whose lower mantle viscosity is higher than 10^{21} Pa sec by at least one order of magnitude.

It should be quite clear on the basis of the complete relaxation diagrams for several viscosity models shown in Fig. 12, that attempts to constrain the mantle viscosity profile by comparing one modal branch of these diagrams to crude estimates of relaxation time for specific spatial scales of defor-

mation, such as is done on Fig. 13, is an inaccurate process at best. There is a good analogy which can be profitably drawn here between the interpretation of isostatic adjustment data and the interpretation of body wave seismic data. Very considerable advances in the latter area have been achieved by interpreting not only the times of arrival of the various phases but also the amplitudes of the waveforms themselves—which requires the construction of synthetic seismograms (e.g., Aki and Richards, 1980). We may consider the arrival times for specific body wave phases to be analogous to the relaxation times for specific horizontal scales. In order to improve the accuracy of our inferences of mantle viscosity from isostatic adjustment data, we are obliged to develop a theory for the equivalent in glacial isostasy of the synthetic seismogram in seismology. As we will see in Section 4, when we require the theory to predict isostatic adjustment amplitudes as well as decay times, then much of the ambiguity of interpretation evident from Fig. 13 may be removed. In the next subsections we will begin to develop the theoretical apparatus required to construct the synthetic "relaxograms" of glacial isostasy.

3.4. Love Number Spectra for Impulsive Forcing

In order to calculate the viscoelastic deformation of the planet's shape produced by glacial loading, we have simply to solve the field equations (3.3) and (3.4) with the appropriate boundary conditions. What we do in practice is to consider first the response of the planet to a surface point-mass load which is applied as a Dirac delta function in the time domain. To determine the appropriate boundary conditions for this problem we treat the point-mass load γ as a uniform disk load of vanishingly small radius α. Expanding γ in a Legendre series then gives

$$\gamma = \sum_{l=0}^{\infty} \Gamma_l P_l(\cos\theta) \tag{3.15}$$

in which the Γ_l are given by (Longman, 1963; Farrell, 1972)

$$\Gamma_l = \frac{2l+1}{4\pi a^2} \tag{3.16}$$

in the limit $\alpha \to 0$. The surface boundary conditions (Longman, 1963; Farrell, 1972) are that $\nabla\phi_2 \cdot \hat{e}_r$ change by $4\pi\gamma$ across $r = a$, that $(\nabla\phi_3 + 4\pi G\rho\mathbf{u}) \cdot \hat{e}_r$ be continuous, that the normal stress balance the applied load so that $\sigma_{rr}(a) = -\gamma g$, and that the tangential stress vanish so that $\sigma_{r\theta}(a) = 0$. When these boundary conditions are expanded in spherical harmonics the expansion coefficients are forced to satisfy

$$T_{rl}(a) = -g\Gamma_l \qquad T_{\theta l}(a) = 0 \qquad Q_l(a) = -4\pi G\Gamma_l \tag{3.17}$$

which are the conditions which replace Eq. (2.38) for the inhomogeneous problem under present consideration. Since the surface load is assumed to be applied as a delta function in the time domain, boundary conditions (3.17) are independent of the Laplace transform variable in the domain of which the field equations (3.3) and (3.4) must be solved. These boundary conditions suffice to completely determine the three other elements of the solution 6-vector $\mathbf{Y} = (U_l, V_l, T_{rl}, T_{\theta l}, \Phi_l, Q_l)^t$ at the surface $r = a$ and throughout the earth. By analogy with the surface loading problem for an elastic sphere it is convenient to describe these remaining elements in terms of a triplet of dimensionless scalar Love numbers (h_l, l_l, k_l) which are functions of r, l, and s defined through the relations

$$\begin{bmatrix} U_l(r, s) \\ V_l(r, s) \\ \Phi_{3,l}(r, s) \end{bmatrix} = \Phi_{2,l}(r) \begin{bmatrix} h_l(r, s)/g_0 \\ l_l(r, s)/g_0 \\ -k_l(r, s) \end{bmatrix} \tag{3.18}$$

Using Eq. (3.18) we may write the total potential perturbation as

$$\Phi_{1,l} = -\Phi_{2,l} + \Phi_{3,l} = -\Phi_{2,l}(1 + k_l) \tag{3.19}$$

where the coefficients in the expansion of the potential of the surface load $\Phi_{2,l}$ are obtained from the definition

$$\phi_2(\mathbf{s}) = \int \frac{G\gamma(r')\, d^2r'}{|\mathbf{r} - \mathbf{r}'|} \tag{3.20}$$

in which integration is over the earth's surface. If we substitute for $\gamma(\mathbf{r})$ in terms of its Legendre expansion Eq. (3.15) and use the addition theorem for spherical harmonics (e.g., Jackson, 1962) we find

$$\phi_2(a, \theta) = \sum_l^{\infty} \frac{4\pi aG}{2l + 1} \Gamma_l P_l(\cos\theta) \tag{3.21}$$

so that

$$\Phi_{2,l}(a, \theta) = \frac{4\pi aG\Gamma_l}{2l + 1} = \frac{ag_0}{M_e} \tag{3.22}$$

where M_e is the mass of the earth and g_0 the surface gravitational acceleration as before.

In Fig. 14 are shown example Laplace transform domain Love number spectra for an earth model with viscosity structure similar to that of model 1 in Fig. 9b and with the elastic structure shown in Fig. 9a. These spectra are found by direct integration of the simultaneous ordinary differential equations (3.11) subject to boundary conditions (3.17) for a sequence of values of s along the positive real s axis in the complex s plane. Two alternative representations of the Love number spectra $h_l(a, s)$ at the earth's surface are shown in Fig. 14, one an x–y plot of $h_l(a, s)$ for various values

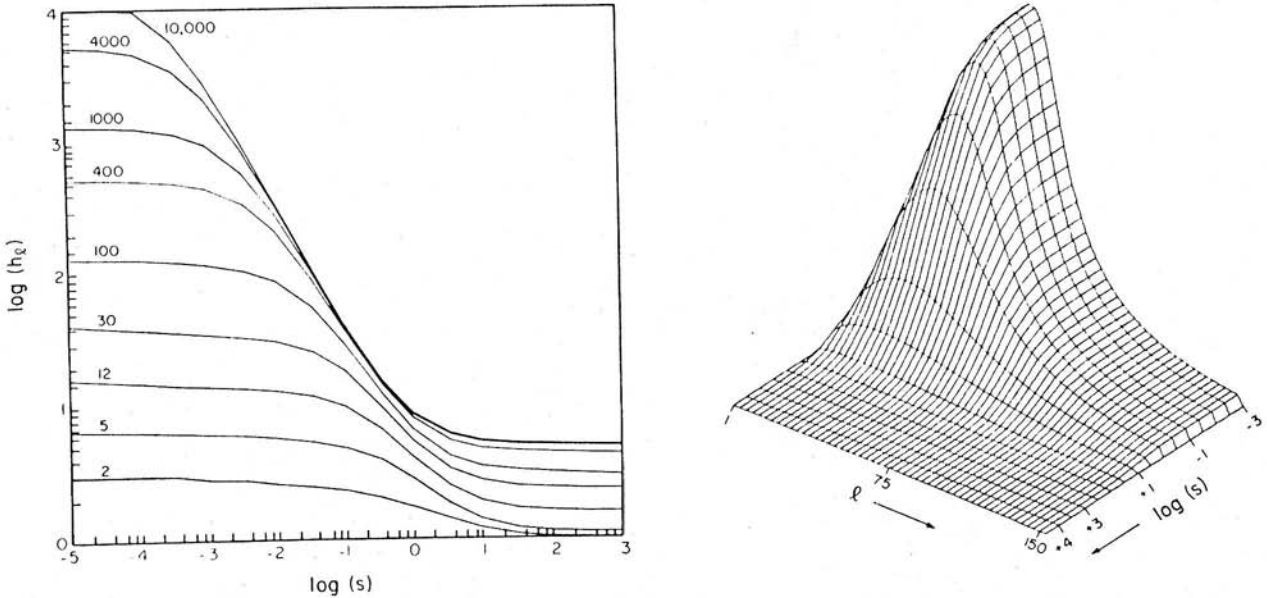

FIG. 14. Love number spectra h_l (a, s) for realistic viscoelastic earth models. The spectra shown on the left are for a model with the viscous structure of model 1 in Fig. 9b except that it lacks a lithosphere. The spectra on the right are for the same model with a lithosphere.

of l marked on the figure, which is for a model with no lithosphere, and the other a three-dimensional plot of the form of the spectral surface, which is for a model which includes a lithosphere. Several important features of these spectra are evident by inspection of the diagram. Most important is the fact that the spectra achieve asymptotic amplitudes both for sufficiently large and for sufficiently small values of the imaginary frequency s. Inspection of Eq. (3.2) shows that in the limit $s \to \infty$ the moduli $\lambda(s)$ and $\mu(s)$ become equal to their elastic values, so that in this limit the Love numbers become asymptotically equal to the Love numbers for an elastic sphere (e.g., Longman, 1963; Farrell, 1972). In this limit, our calculations agree with those of previous authors. In the opposite limit $s \to 0$, $\lambda(s) \to K$, the elastic bulk modulus, and $\mu(s) \to \nu s$, so that the Maxwell solid becomes like an incompressible viscous fluid. The existence of the small s asymptote is indicative of the existence in this limit of a new state of viscous gravitational equilibrium. As we will show, this is the state of isostatic equilibrium which obtains in the limit of long time. Also evident by inspection of the spectra shown on this figure (for the model with a lithosphere) is the fact that for sufficiently short wavelength the small s asymptote is reduced to equality with the large s asymptote and this is due to the complete suppression of viscous relaxation at the shortest wavelengths. In order to understand the meaning of the spectral asymptotes at small values of s, we need only consider the inversion of these spectra into the time domain. Since each of the Love numbers $h_l(a, s)$, $l_l(a, s)$, $k_l(a, s)$ has a spectrum similar to those shown in Fig. 14, they can all be expanded in the form

$$h_l(a, s) = h_l^{\mathrm{V}}(a, s) + h_l^{\mathrm{E}}(a) \tag{3.23}$$

where $h_l^{\mathrm{E}}(a)$ are the elastic asymptotes and $h_l^{\mathrm{V}}(a, s)$ therefore represents the viscous contribution to the response. The Laplace inverse of Eq. (3.23) is just

$$h_l(a, t) = \frac{1}{2\pi i} \int_{\mathcal{L}_1} h_l^{\mathrm{V}}(a, s) e^{st}\, ds + h_l^{\mathrm{E}}(a)\, \delta(t) \tag{3.24}$$

Now the integral along the Bromwich path $\mathcal{L}_1$ in Eq. (3.24) may be evaluated using Cauchy's theorem, which allows us to write

$$\int_{\mathcal{L}_1} h_l^{\mathrm{V}}(a, s) e^{st}\, ds = -\int_{\mathcal{L}_2} h_l^{\mathrm{V}}(a, s) e^{st}\, ds + 2\pi i \sum \begin{bmatrix} \text{residues at the poles} \\ \text{of the integrand} \\ \text{inside } (\mathcal{L}_1 + \mathcal{L}_2) \end{bmatrix} \tag{3.25}$$

Since the first integral on the right-hand side of Eq. (3.25) goes to zero as the radius of the semicircle tends to infinity, Eq. (3.24) therefore reduces to

$$h_l(a, t) = \sum \begin{bmatrix} \text{residues at the poles of the} \\ \text{integrand inside } (\mathcal{L}_1 + \mathcal{L}_2) \end{bmatrix} + h_l^{\mathrm{E}}(a)\, \delta(t) \tag{3.26}$$

Now the poles of the integrand $h_l^V(a, s)e^{st}$ are located at the zeros of the secular function $D_2(s, l)$ in Eq. (3.14) which we determine in the way discussed in the last section. These poles are all on the negative real s axis and we may label them $s = -s_j^l$ where the s_j^l are ≥ 0. Furthermore, they are all simple poles, and we may usually write

$$h_l(a, t) = \sum_j r_j^l e^{-s_j^l t} + h_l^E(a)\,\delta(t) \tag{3.27a}$$

where the "initial amplitudes" r_j^l can be determined as follows. If $h_l(a, t)$ have time domain forms (3.27a), they then have Laplace transform domain forms

$$h_l(a, s) = \sum_j r_j^l/(s + s_j^l) + h_l^E(a) \tag{3.27b}$$

If solutions of the inhomogeneous problem are obtained for $s = +s_j^l$ to give

$$h_l^V(s_j^l) = h_l(a, s_j^l) - h_l^E = \sum_{i=1}^{N} r_i^l/(s_j^l + s_i^l) \tag{3.28}$$

and if we define the elements of the matrix **m** as

$$m_{ij} = 1/(s_j^l + s_i^l) \tag{3.29}$$

then Eq. (3.28) may be written as

$$h_l^V(s_j^l) = m_{ij} r_i^l \tag{3.30}$$

from which we may compute the r_i^l as

$$r_i^l = m_{ij}^{-1} h_l^V(s_j^l) \tag{3.31}$$

This collocation method provides a very efficient means of solving the inhomogeneous problem using the discrete spectrum determined by solving the homogeneous problem. Solutions of the inhomogeneous problem are thereby represented in the form of a superposition of normal modes of viscous gravitational relaxation in which the r_j^l represent the excitation strengths for point forcing. Given the time domain forms (3.27) for the impulse response problem, we may employ them to compute the spectral amplitudes required to describe the response if the load is applied at $t = 0$ and then allowed to remain on the surface. These amplitudes are obtained by convolving Eq. (3.27) with a Heaviside step function to obtain

$$\begin{aligned} h_l^H(a, t) &= h_l(a, t) * H(t) \\ &= \sum_j (r_j^l/s_j)(1 - e^{-s_j^l t}) + h_l^E \end{aligned} \tag{3.32}$$

where the $*$ denotes convolution in time. Now inspection of Eqs. (3.32) and (3.27) shows that

$$\lim_{s\to 0} h_l(a, s) = \sum r_j^l/s_j^l + h_l^E = \lim_{t\to 0} h_l^H(a, t) \tag{3.33}$$

and the meaning of the small-s asymptotes of the impulse response spectra shown in Fig. 14 is thus clear. The difference between the large-s and small-s asymptotes, $\Sigma_j r_j^l/s_j^l$, for each value of l measures the amount of viscous relaxation which would occur if a load of harmonic degree l were applied to the surface at $t = 0$ and left for an infinite time. In Fig. 15 we show a sequence of plots of the viscous parts of the Heaviside Love number time histories

$$h_l^{H,V}(a, t) = \sum_j (r_j^l/s_j^l)(1 - e^{-s_j^l t})$$

for several values of l. The time interval covered by these plots is 20 kyr, and adjacent to the right margin of the figure we show the amount of relaxation which has yet to be realized until equilibrium of that harmonic is achieved. Given these time-dependent Love numbers for our radially inhomogeneous viscoelastic earth models we are now in a position to construct the Green's functions which are required to calculate the response to realistic space–time histories of surface loading. Before proceeding to discuss this phase of the analysis, however, we will provide a brief discussion of the method we have developed for calculation of the infinite-time response amplitudes which are shown adjacent to the curves on Fig. 15. These

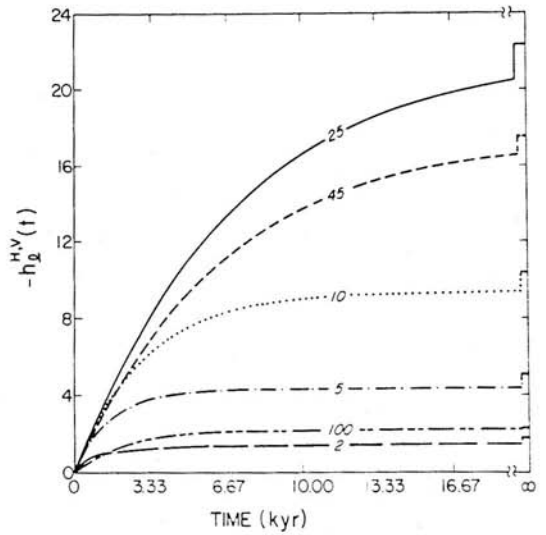

FIG. 15. Love number temporal history $h_l^{H,V}(a, t)$ for several values of l. The parameter $h_l^{H,V}$ is the viscous part of the Heaviside displacement amplitude and the viscosity model is model 1 shown in Fig. 9b.

amplitudes cannot in fact be computed by direct integration of Eq. (3.11) at small values of s because in this limit the system of ode's becomes "stiff" and is not directly integrable. The problem is not merely of technical interest. As we will show, the accurate calculation of this long-time response is crucial to the prediction of the free-air gravity anomaly.

3.5. *Elastic and Isostatic Asymptotes of the Love Number Spectra*

Although the elastic asymptotes of the individual relaxation spectra may be calculated in a straightforward way by setting $s = \infty$ in the field equations, inspection of the individual elements of the **A** matrix listed in Eq. (3.12) shows that the limit $s \to 0$ cannot be taken directly. From Eq. (3.2), however, we see that the limit $s \to 0$ and the limit $\nu \to 0$ are equivalent in the sense that in either limit the shear modulus $\mu(s)$ vanishes. Under this assumption, the field equations (3.3), (3.4), and (3.5) reduce to the following forms

$$0 = \rho_0 \nabla \phi_1 - \rho_1 g_0 \hat{e}_r - \nabla p \tag{3.34a}$$

$$\nabla^2 \phi_1 = 4\pi G \rho_1 \tag{3.34b}$$

$$\rho_1 = -\rho_0 \nabla \cdot \mathbf{u} - \mathbf{u} \cdot (\partial_r \rho_0) \hat{e}_r \tag{3.34c}$$

where we have introduced a pressure field (mean normal stress) through the association $p \equiv \mathbf{u} \cdot \rho_0 g_0 \hat{e}_r - K e_{ii}$. The static deformation of an inviscid part of the earth has most recently been discussed by Dahlen and Fels (1978), whose analysis agrees with previous conclusions of Smylie and Mansinha (1971) and others. There it is shown that fluid particles undergoing a quasi-static deformation experience changes neither of pressure nor of density as the deformation proceeds. It therefore follows that the dilatation is zero everywhere. Substituting $\nabla \cdot \mathbf{u} = 0$ in Eq. (3.34c) and expanding all variables in spherical harmonics reduces (3.34a,b) to (Wu and Peltier, 1982a)

$$d_r^2 \phi + \frac{2}{r} d_r \Phi - \left[\frac{l(l+1)}{r^2} + \frac{4\pi G \rho_0}{g_0} \right] \Phi = 0 \tag{3.35a}$$

$$U = -\Phi / g_0 \tag{3.35b}$$

In Eq. (3.35b), U is to be interpreted as the displacement of an equipotential, isobaric, or material surface. Using Eq. (3.10) we may reduce Eq. (3.35a) to a set of two simultaneous ordinary differential equations in the 2-vector $\mathbf{Y}^l = (\Phi_l, Q_l)^t$ of the form

$$\frac{d\mathbf{Y}^l}{dr} = \mathbf{A}^l \mathbf{Y}^l \tag{3.36a}$$

where

$$\mathbf{A}^l = \begin{bmatrix} 4\pi G \rho_0 / g_0 - (l+1)/r & 1 \\ 4\pi G \rho_0 (l-1)/g_0 r & (l-1)/r - 4\pi G \rho_0 / g_0 \end{bmatrix} \tag{3.36b}$$

In order to calculate the spectral asymptotes at $s = 0$ we must match solutions of Eq. (3.36a) across the mantle–lithosphere boundary to the elastic solutions which are valid in the lithosphere itself. If $\Phi_l^M(b^-)$ and $Q_l^M(b^-)$ are solutions of Eq. (3.36a) just below this boundary, then the solution just above the boundary is given by

$$\begin{bmatrix} U_l(b^+) \\ V_l(b^+) \\ T_{rl}(b^+) \\ T_{\theta l}(b^+) \\ \Phi_l(b^+) \\ Q_l(b^+) \end{bmatrix} = C_1 \begin{bmatrix} -U_l^M(b^-)/g(b) \\ 0 \\ 0 \\ 0 \\ \Phi_l^M(b^-) \\ Q_l^M(b^-) \end{bmatrix} + C_2 \begin{bmatrix} 0 \\ 1 \\ 0 \\ 0 \\ 0 \\ 0 \end{bmatrix} + C_3 \begin{bmatrix} 1 \\ 1 \\ \rho_0(b^-)g_0(b) \\ 0 \\ 0 \\ 4\pi G\rho_0(b^-) \end{bmatrix} \tag{3.37}$$

where b is the radius of the mantle–lithosphere interface and the C_i are determined as usual by satisfying boundary conditions (3.17). It will be recognized that this procedure for calculating the infinite-time spectral asymptotes is identical to the procedure which must be followed at arbitrary s for matching solutions in the inviscid core to solutions in the mantle across the core–mantle boundary. The procedure is perfectly stable numerically.

3.6. *Green's Functions for the Surface Mass Load Boundary Value Problem*

Green's functions for the gravitational interaction problem may be computed for various signatures of the response by summing infinite series like Eq. (3.7). In general these Green's functions may be written as the sum of an elastic part and a viscous part due to the fact that the Love numbers themselves can be so expanded. From Eq. (3.7b) we see that the Green's function for radial displacement may be written in terms of the Love numbers $h_l^H(a, s)$, assuming Heaviside forcing in time, as

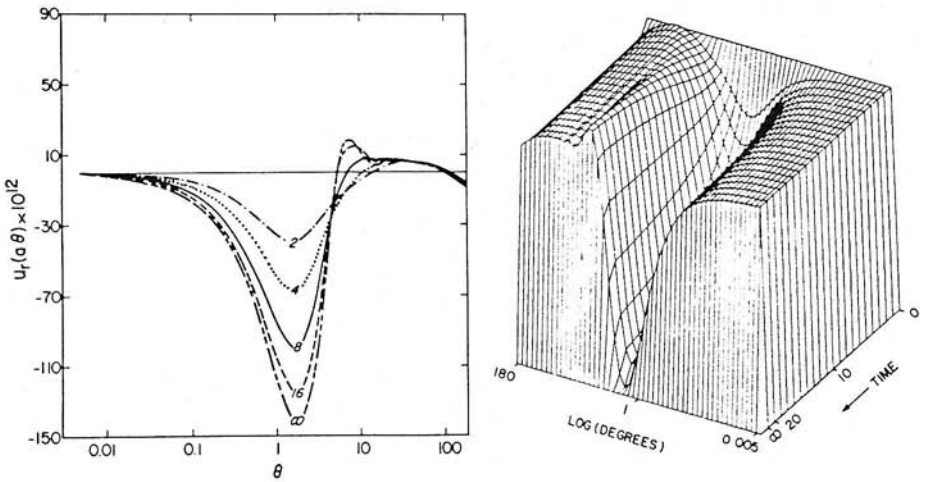

FIG. 16. Radial displacement Green's function $u^{H,V}(\theta, t)$ for viscosity model 1 shown in Fig. 9b. The Green's function has been multiplied by $a\theta$ to remove the geometric singularity at $\theta = 0$.

$$u^{H}(\theta, t) = \frac{a}{M_e} \sum_{l=0}^{\infty} h_l^{H}(a, t) P_l(\cos\theta) \tag{3.38}$$

Similar forms may be constructed for the perturbation of the gravitational acceleration $\alpha(\theta, t)$ (the "gravity anomaly") and for the perturbation of the gravitational potential $\phi(\theta, t)$ which may be shown (Longman, 1963) to have the forms

$$\alpha^{H}(\theta, t) = \frac{g}{M_e} \sum_{l=0}^{\infty} [l + 2h_l^{H} - (l+1)k_l^{H}]\, P_l(\cos\theta) \tag{3.39}$$

$$\phi^{H}(\theta, t) = \frac{ag}{M_e} \sum_{l=0}^{\infty} (1 + k_l^{H} - h_l^{H})\, P_l(\cos\theta) \tag{3.40}$$

In Eqs. (3.39) and (3.40) the Love number independent terms are due to the direct effects of the surface load, the terms involving h_l are due to the displacement of the earth's surface, and those involving k_l are due to the internal redistribution of matter produced by the time-dependent displacement field associated with the adjustment process. Once we have calculated the Love numbers, the Green's functions are obtained simply by summing the above infinite series, which is a straightforward process except in the elastic limit, where acceleration techniques such as the Euler transformation must be employed (Peltier, 1974).

One example of a Green's function is shown in Fig. 16, which illustrates the viscous part of the radial displacement response (3.38) for the model with uniform mantle viscosity and 1066B elastic structure. Again we give two presentations of this function. The first is a simple sequence of x–y plots which show $u^{H,V}(\theta, t)$ as a function of θ for several values of t marked adjacent to each curve in kiloyears. The Green's function has been multiplied by $a\theta$ to remove the geometric singularity which would otherwise occur at $\theta = 0$ for plotting purposes. We also show in this figure a full three-dimensional view of the $u^{H,V}(\theta, t)$ surface. Either representation shows that the viscous response is zero at $t = 0$ as it must be from Eq. (3.32). As time passes, the surface sags under the load while peripheral to the load the local radius is increased. As we shall see in the next section, it is the collapse of this so-called peripheral bulge which explains the submergence of shorelines in the region just outside the ice sheet margin which obtains along the east coast of North America. Also evident from inspection of Fig. 16 is the fact that for the uniform viscosity model the peripheral bulge migrates in time. This effect is absent in models which have high lower mantle viscosity (Peltier, 1974), and so observations of bulge migration can be quite diagnostic of the deep viscosity structure of the earth.

Having constructed Green's functions for the radially stratified viscoelastic earth model, such as that shown in Fig. 16, we can proceed to calculate the response of the planet to an arbitrary known history of surface mass loading. This response must in general include the elastic contribution. In the next subsection we will illustrate the characteristic patterns of deformation which are forced by parabolic disk load approximations to the major Pleistocene ice sheets.

3.7. Response to Simple Disk Load Deglaciation Histories

Convolution of the Green's functions over simple circular disk loads involves a straightforward exercise in spherical trigonometry, the details of which are provided in Wu and Peltier (1982a). Rather than repeat these details here, we will simply describe a few of the most interesting results which have been derived from such calculations. Figure 17a,b,c shows the radial displacement response forced by surface loading with a circular disk with parabolic thickness profile with disk radius and mass chosen to give reasonable approximations to the Lake Bonneville, Fennoscandia, and Laurentide loads, respectively. All calculations have been performed with the Green's function for viscosity model 1 shown in Fig. 9b and are based upon the assumption that the disk load is applied to the surface at $t = 0$ and left in place. The computed response is therefore that which would be produced by instantaneous glaciation of the surface, not deglaciation. The disk radii

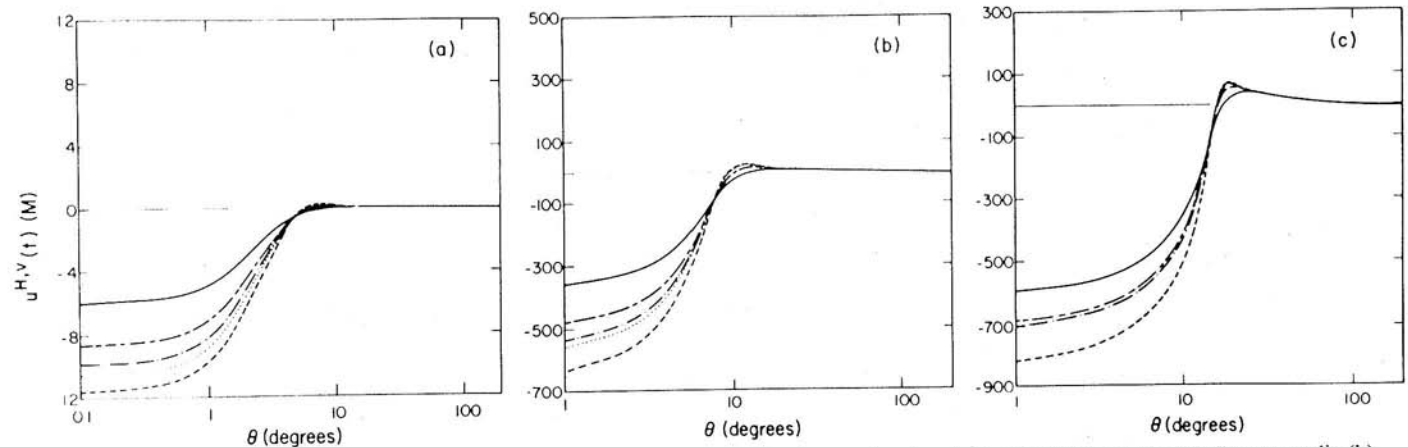

FIG. 17. Radial displacement response forced by a parabolic circular disk load approximation to the Lake Bonneville (a), Fennoscandia (b), and Laurentide (c) loads. Only the viscous contribution is shown, and the viscosity model is model 1 of Fig. 9b. The response is shown at times of (——) t = 4 kyr; (– – –) t = 8 kyr; (–·–) t = 12 kyr; (· · ·) t = 16 kyr; (- - -) t = ∞ kyr.

which approximate the loads at these three sites are shown on the individual plates by the thin solid line which extends from $\theta = 0°$ at $u_r^{H,V} = 0$ and ends at the edge of the disk. The radii of the Lake Bonneville, Fennoscandia, and Laurentide disks are respectively 1.2°, 8°, and 15°. Crittenden (1963) estimated the maximum depth of Lake Bonneville to be about 305 m, corresponding to a mass of approximately 10^{16} kg, and we have used his estimates in our disk calculations. For the Fennoscandia and Laurentide loads our parabolic disk models are taken to have central thickness of 2500 m and 3500 m, respectively, and are based upon the ice sheet reconstructions in Peltier and Andrews (1976). Figure 17 shows only the viscous contribution to the total radial displacement response at each of these sites, and this is given for the sequence of times shown in the figure caption.

The results of these simple disk load integrations illustrate several important characteristics of the isostatic adjustment process. Inspection of the calculated response for the Lake Bonneville model (Fig. 17a), for example, shows that the maximum amplitude of the response predicted by the model is only about 12 m, compared to the observed maximum of 64 m. Therefore, although viscosity model 1, which has a 120-km-thick lithosphere, predicts a relaxation time which is close to the observed time (Fig. 13) for the deformation at Lake Bonneville, the predicted amplitude is enormously underestimated. The reason for this is clearly that the lithospheric thickness in this model is excessive for the Basin and Range region and this leads to a suppression of the viscous relaxation, a fact previously pointed out in reference to the Love number spectra (Fig. 14) and their time domain forms (Fig. 15). In order to fit the observed relaxation at the Lake Bonneville site, the lithospheric thickness can be at most 40 km. But this modification of the model leads to a marked increase of the relaxation time for the dominant wavelengths in the response, which must be corrected by introducing a low-viscosity zone in the sublithospheric region. This example serves to reinforce the comment made previously in the discussion of Fig. 13. One cannot obtain an acceptable inference of the mantle viscosity structure on the basis of the relaxation spectrum alone. Only if response amplitudes and relaxation times are reconciled simultaneously will a reasonable inference result.

Comparison of Fig. 17a with Fig. 17b for the Fennoscandia model shows that as the horizontal scale of the load increases the peripheral bulge becomes more substantial. This is reinforced by the result for the model Laurentide load shown in Fig. 17c. The maximum height of the bulge in the region peripheral to Fennoscandia would be only about 20 m, whereas that peripheral to Laurentide would be about 70 m. Also evident as the horizontal scale of the load increases is the fact that the slope of the surface near the edge of the load becomes steeper, an effect which can be understood qualitatively on the basis of the increasing importance of the lithosphere for smaller scale loads.

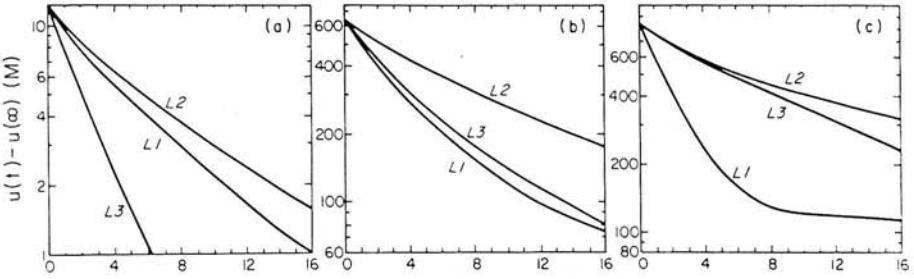

FIG. 18. Uplift remaining at the center of Lake Bonneville, Fennoscandia, and Laurentide depressions on the basis of the calculations shown in Fig. 17. Note the highly nonexponential response of the large-scale Laurentide region when the uniform viscosity model (L1) is employed.

In Figure 18a,b,c we show plots of the uplift remaining at the center of the Lake Bonneville, Fennoscandia, and Laurentide model disk loads as a function of time for each of the viscosity models shown in Fig. 9b. Models 1, 2, and 3 in Fig. 9b are labeled L1, L2, and L3 on this figure to emphasize that the models all have lithospheres which are 120 km thick. These response curves are all plotted on a semilogarithmic scale so that if the response were perfectly exponential they would all appear as straight lines. Inspection of these diagrams shows that every model predicts an increase of apparent relaxation time with time, with the effect generally becoming more pronounced as the spatial scale of the load increases and most important for the uniform mantle viscosity model L1. Of greatest interest is the comparison of Fig. 18b and c for Fennoscandia and Laurentide, respectively. Since models L1 and L3 deliver very similar response at the former site, it is clear that for surface loads of this scale both the increase of relaxation time and the decrease of relaxation amplitude produced by high viscosity in the lower mantle may be compensated by a low-viscosity channel. Such is not the case for a Laurentide-scale load, however; at least over the first 8×10^3 yr of relaxation, models L2 and L3 deliver very similar response, so that the influence of the low-viscosity channel is very small. The most important point to recognize by inspection of Fig. 18c is that the response curve for the uniform mantle viscosity model L1 is strongly nonexponential in shape. The first 8 kyr of the relaxation are dominated by a relaxation time near 2 kyr, whereas the response for times in excess of this appears to be dominated by a relaxation time on the order of 10^5 yr. This demonstrates very clearly the fundamental property of realistic viscoelastic models of the planet which makes it possible for them to simultaneously explain a short characteristic relaxation time for the initial stages of isostatic adjustment and a large free-air gravity anomaly indicative of a large amount

of uplift remaining. The reason for the transition in the response from one relaxation time to another is clear by inspection of the relaxation diagram for model L1 shown in Fig. 12a. At the dominant angular order $n = 6$ for the Laurentide load the M0, C0, L0 modes all have relaxation times of about 2000 yr, and the initial response will therefore be dominated by a response time of this order. For this model, however, the M1 mode associated with the density jump across the phase transition at 670 km depth is also efficiently excited, and it has a relaxation time of about 2×10^5 yr. The transition from short to long relaxation time for the Laurentide-scale load and viscosity model L1 is therefore completely explained on the basis of initial M0 (C0) and final M1 dominance of the response. As we will see in the following sections, this property of realistic viscoelastic models is crucial to understanding several different phenomena associated with glacial isostatic adjustment. The prediction of this characteristic of the adjustment mechanism must be considered one of the most important successes of the modern theory of this process.

4. Postglacial Variations of Relative Sea Level

Although the radial displacement response curves for simple disk load approximations to actual deglaciation events provide extremely useful insights into the actual histories of isostatic adjustment contained in the Quaternary geological record, they are imperfect approximations to these histories in many important respects. The problem is not simply that the ice sheets are not circular disks with parabolic cross sections which are removed and applied instantaneously. It is more fundamental. Relative sea level data such as those shown in Fig. 7 can be considered as measures of the change in local radius of the earth only to the extent that the local surface of the ocean (the geoid) can be assumed to have maintained a constant local distance from the earth's center of mass throughout the period of isostatic adjustment. If this were the case, then the flights of beaches cut into continental coastal areas, such as those shown in Fig. 6, would measure the local radial displacement histories exactly. This view turns out to be somewhat naive for the following reason. As the earth deforms in response to the melting of its surface ice sheets there is a discharge of meltwater to the ocean basins, which raises the elevation of the sea surface (geoid) with respect to the center of mass of the earth. If this increase of level were uniform, then it would be possible to simply correct the computed radial response curves for the increase in water level, and the response due to ocean loading could be simply added to the response due to glacial unloading at any point of interest. In fact, the meltwater produced by ice sheet dis-

integration cannot be added uniformly to the ocean basins since this would violate the equilibrium constraint that the geoid remain an equipotential surface. As the ice sheets melt, water is distributed over the ocean basins in the unique fashion required to ensure that the surface remains equipotential. In order to calculate postglacial variations of RSL accurately we are forced to develop a theory which is capable of predicting global histories of meltwater redistribution. In the next subsection the structure of this theory will be developed and discussed.

4.1. An Integral Equation for Relative Sea Level

The sea level equation which we will derive is based upon the Green's function for the perturbation of the gravitational potential defined in Eq. (3.40). Its structure will be most clearly understood if we begin by supposing that all of the ice sheets which were on the surface at glacial maximum melted instantaneously. If $L(\theta, \phi)$ is used to denote the ice thickness removed from position (θ, ϕ) at $t = 0$ and $S(\theta, \phi, t)$ the amount of water added to the ocean at position (θ, ϕ) and time t, then we may compute the net change of potential at any position on the surface by convolution of the surface loads L and S with the Green's function ϕ^{H} in Eq. (3.40) to obtain

$$\Phi(\theta, \phi, t) = \rho_{\mathrm{I}} \phi^{\mathrm{H}} \underset{\mathrm{I}}{*} L + \rho_{\mathrm{W}} \phi^{\mathrm{H}} \underset{\mathrm{O}}{*} S \tag{4.1}$$

where $\underset{\mathrm{I}}{*}$ and $\underset{\mathrm{O}}{*}$ indicate convolution over the ice and water, respectively, and ρ_{I} and ρ_{W} are ice and water densities. From Eq. (3.40) it is clear that Eq. (4.1) includes the change of potential due to the vertical displacement of the solid surface of the earth since the Green's function contains the Love number h_l. The change of potential given by Eq. (4.1) will force an adjustment of the thickness of the seawater locally in the amount (Farrell and Clark, 1976)

$$S = \frac{\Phi(\theta, \phi, t)}{g} + C \tag{4.2}$$

where the constant C is chosen such that conservation of mass is ensured. Now Eq. (4.2) is a result of first-order perturbation theory, which is valid for sufficiently small changes of the local bathymetry S. It is important to note that S is, by construction, the local variation of sea level with respect to the deformed surface of the solid earth and is thus precisely the quantity which is recorded in RSL data such as shown in Fig. 7. Substitution of Eq. (4.2) into Eq. (4.1) leads to the equation

$$S = \rho_I(\phi^H/g) \underset{I}{*} L + \rho_W(\phi^H/g) \underset{O}{*} S + C \tag{4.3}$$

In order to determine the constant C we note that the integral of $\rho_W S$ over the surface of the oceans must equal the instantaneous value of the total mass which has been lost by ice sheet disintegration at time t. Therefore

$$\begin{aligned} \langle \rho_W S \rangle_o &= \rho_W \langle \rho_I(\phi^H/g) \underset{I}{*} L + \rho_W(\phi^H/g) \underset{O}{*} S \rangle_o + \langle C \rangle_o \rho_W \\ &= -M_I(t) \end{aligned} \tag{4.4}$$

The minus sign on the right-hand side of Eq. (4.4) is required because $M_I(t)$, the mass loss history for all ice sheets combined, is defined as negative for load removal. In Eq. (4.4) the symbol $\langle \quad \rangle_o$ is used to denote integration over the oceans. Since C is constant at fixed time, therefore $\langle C \rangle_o = CA_o$, where A_o is the area of the oceans, and Eq. (4.4) gives

$$C = -\frac{M_I(t)}{\rho_W A_o} - \frac{1}{A_o} \left\langle \rho_I \frac{\phi^H}{g} \underset{I}{*} L + \rho_W \frac{\phi^H}{g} \underset{O}{*} S \right\rangle_o \tag{4.5}$$

With C given by Eq. (4.5), Eq. (4.3) is an integral equation for the unknown field $S(\theta, \phi, t)$ which we call the sea level equation. It is an integral equation since S appears not only on the left-hand side but also in the convolution integral on the right-hand side. Given the deglaciation history $L(\theta, \phi, t)$, and thus $M_I(t)$, and the potential perturbation Green's function ϕ^H for a specific viscoelastic model of the planet, we may invert this integral equation to find the history of RSL $S(\theta, \phi, t)$ at any point on the earth's surface.

This discussion should serve to make clear the basic structure of the isostatic adjustment problem. Two inputs to the theoretical model are required before the model can be employed to make a prediction. The first of these is a viscoelastic model of the planetary interior, whereas the second is a model of ice sheet disintegration. Neither of these functionals of the model is perfectly known *a priori*, and we are obliged to proceed iteratively to refine our knowledge of them. We will not provide a description here of the numerical methods required to solve the integral equation (4.3) or the generalization of of it which describes RSL variations produced by realistic deglaciation histories. Detailed descriptions of the numerical methods will be found in Peltier *et al.* (1978) and Wu and Peltier (1982b). Before describing the results which have been obtained through application of Eq. (4.3), we will discuss in the next subsection how one constructs first-guess approximations to the history of surface deglaciation. It is only because *a priori* knowledge of this functional of the model does exist that we may begin the iterative process which leads eventually to rather precise knowledge of the mantle viscosity profile.

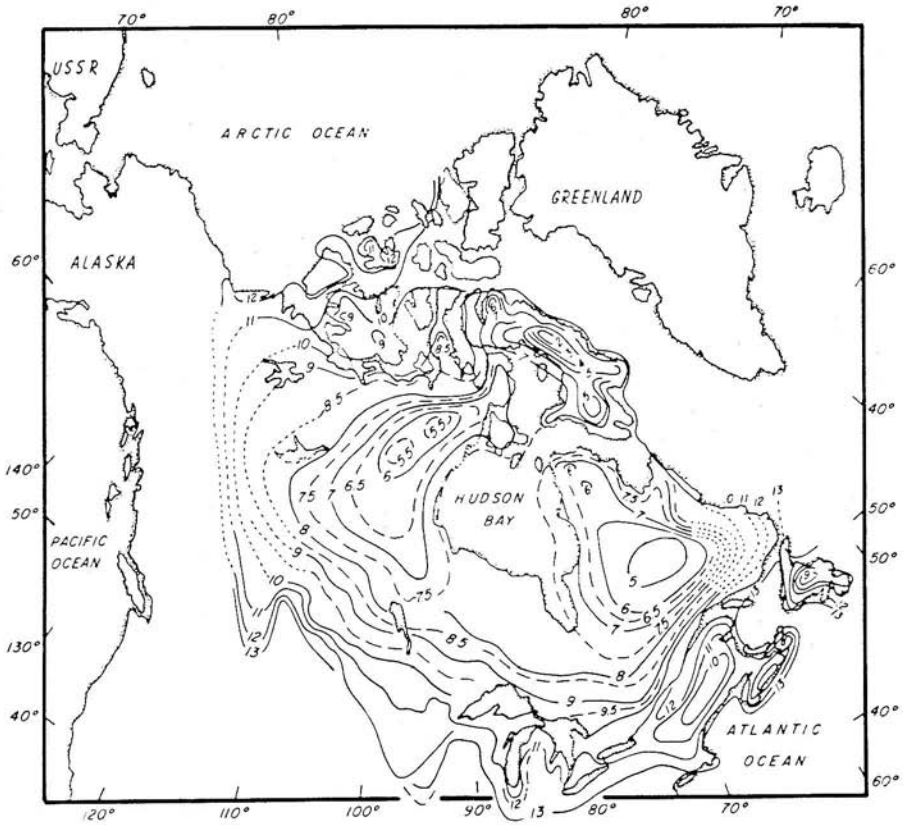

FIG. 19. Disintegration isochrones for the Laurentide ice sheet based upon the map in Bryson *et al.* (1969).

4.2. *Inputs to the RSL Calculation: The Deglaciation Chronology and Mantle Viscosity Profile*

Several distinct kinds of information are required to construct reasonable *a priori* models of the deglaciation histories of the major ice sheets which existed on the earth's surface 20.000 yr ago. Perhaps the most important piece of information is that concerning the location of the ice sheets themselves, and this is provided by ^{14}C-controlled locations of the terminal moraines of these ice masses. In Fig. 19 we show a map of disintegration isochrones based on that in Bryson *et al.* (1969) which shows the variation in space of the Laurentide ice margin during the deglaciation phase which began at about 18 kyr B.P. Information of the same type is also available for the Fennoscandia region. Besides the ice bound in these major Northern

Hemisphere continental complexes, there was also considerable mass contained in Alpine complexes in the Rocky Mountains, the Andes, and the European Alps. Indeed, it was on the basis of his observations of evidence of Alpine ice masses that Agassiz first put forward his arguments for the Ice Age itself. As a fraction of the ice bound in the Laurentide and Fennoscandian complexes, however, these Alpine contributions are very small indeed. This is not true of the additional mass which was lost from the Antarctic complex, however; evidence from this region suggests that as much as 15–20% of the total increase in ocean volume produced by deglaciation may have come from a large-scale melting event over the Ross Ice Shelf in West Antarctica.

In order to estimate the total volume of ice which was bound in the major complexes we are obliged to rely upon the RSL data themselves. Prior to the new understanding of these data which was realized through the theoretical model embodied in Eq. (4.3), it was assumed by virtually all scientists working in the field of Quaternary geomorphology that the rise of sea level in the global ocean produced by the melting of glacial ice was a constant independent of location. In the literature of the subject this concept is referred to as *eustatic sea level*, and there has been a great deal of effort expended to measure *the* eustatic sea level curve. On the basis of our previous discussion, of course, we know that this concept is of limited utility, since sea level cannot rise uniformly as the ice melts because this would generate a new ocean surface which was not an equipotential surface. In spite of this limitation, however, the variation of the increase of water depth as a function of time between sites at different geographical locations is not extreme if attention is focused upon sites which are sufficiently far removed from the ice sheets themselves. At such sites the oldest beach is inevitably at the greatest depth below present-day sea level, and the maximum submergence is on the order of 100 m. In Fig. 20 we show a typical eustatic sea level curve from Shepard (1963) which is based upon a particularly extensive RSL record from the Gulf of Mexico. These data extend back to 16 kyr B.P. and show an increase of water depth since that time of something in excess of 80 m. Compared to Shepard's data is the eustatic sea level curve based upon the mass loss history of the deglaciation model ICE-1 tabulated in Peltier and Andrews (1976).

The ICE-1 deglaciation model was constructed by combining Shepard's (1963) eustatic sea level curve with the disintegration isochrone map of Bryson *et al.* (1969) for the Laurentide ice sheet and equivalent data for Fennoscandia. What we did was simply to partition the total mass loss implied by Shepard's curve between the Laurentide and Fennoscandian ice sheets roughly in proportion to their surface areas on the basis of the assumption that the thickness profile of each ice sheet had the parabolic profile

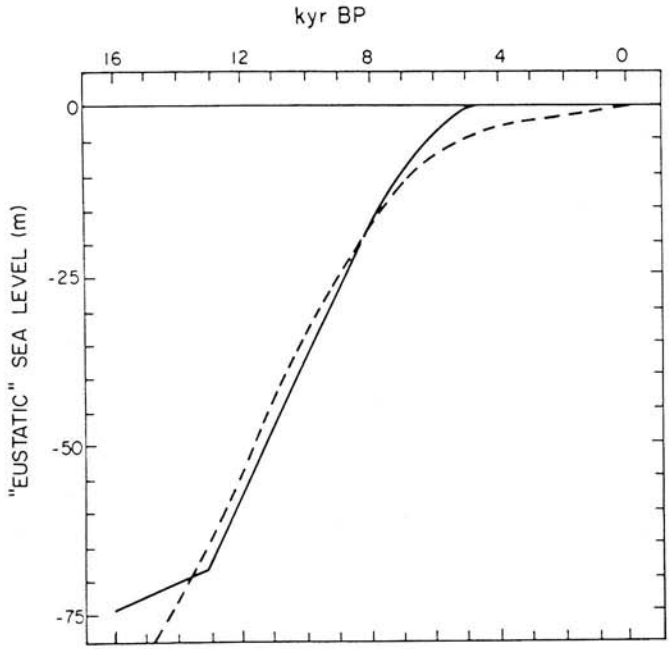

FIG. 20. Eustatic sea level curve from Shepard (1963) (dashed) compared to the mass loss history of the ICE-1 model tabulated by Peltier and Andrews (1976) (solid curve).

which obtains under the assumption of perfectly plastic behavior. Three time slices through a slightly modified ICE-2 chronology are shown for both the Laurentide and Fennoscandian complexes in Fig. 21. Most rapid disintegration occurs around 12 kyr B.P. as is evident from Shepard's eustatic curve shown in Fig. 20. The Laurentide history is quite complicated, since the ice center over Hudson Bay collapses first, leaving high stands of ice both to the east over Labrador–Ungava and to the northwest. It should be recognized, however, from the way in which the ICE-1(2) chronology was constructed, that it is to be considered a first approximation to the actual history of glacial retreat. It will have to be refined as we refine our knowledge of the mantle viscosity profile. The iterative process proceeds by fixing ICE-1 and determining a "best" $\nu(r)$, then fixing $\nu(r)$ and refining ICE-1, then refining $\nu(r)$, etc., until convergence is achieved. This method of attack is feasible only because we have a good *a priori* estimate of the deglaciation chronology in the form of the ICE-1 model.

In the following subsections we will discuss the predictions which are obtained for RSL history when the ICE-1 chronology is inserted into the sea level equation (4.3). By performing such calculations for several different

mantle viscosity profiles we will assess the extent to which RSL data may be employed to constrain this property of the earth's mantle.

4.3. Output from the RSL Calculation: Global Sea Level Histories

In Fig. 22 we show four time slices through a solution to Eq. (4.3) obtained for earth model L1 and a deglaciation history which is very similar to the ICE-1 history of Peltier and Andrews (1976). This new deglaciation history is called ICE-2 and has been tabulated in Wu and Peltier (1982b), where the slight differences between it and ICE-1 are also described. It was actually

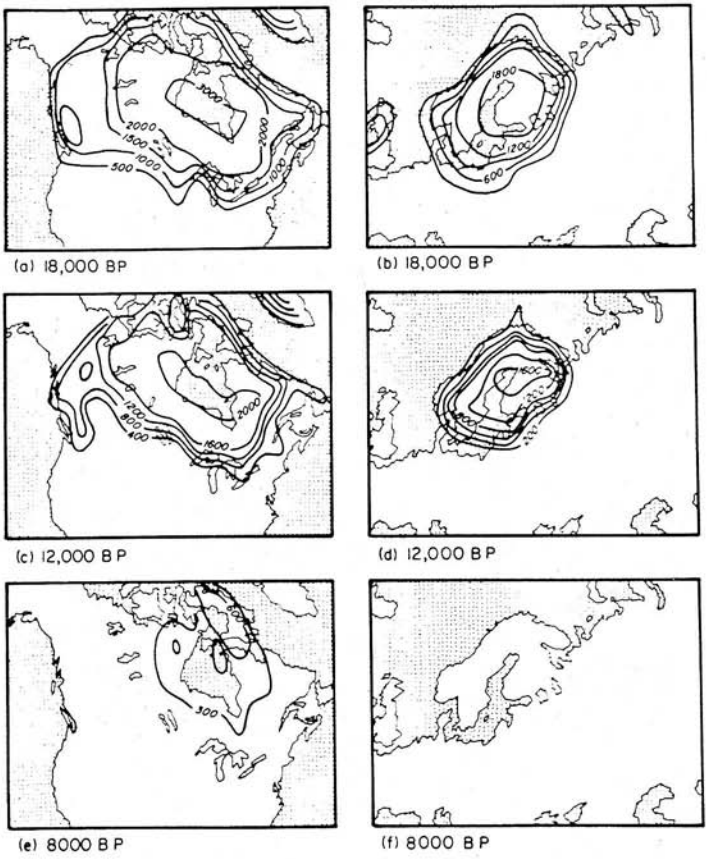

FIG. 21. Three time slices through the ICE-2 melting chronology tabulated in Wu and Peltier (1982b). Maps of ice sheet topography are shown for both the Laurentide (a, c, e) and Fennoscandia (b, d, f) regions.

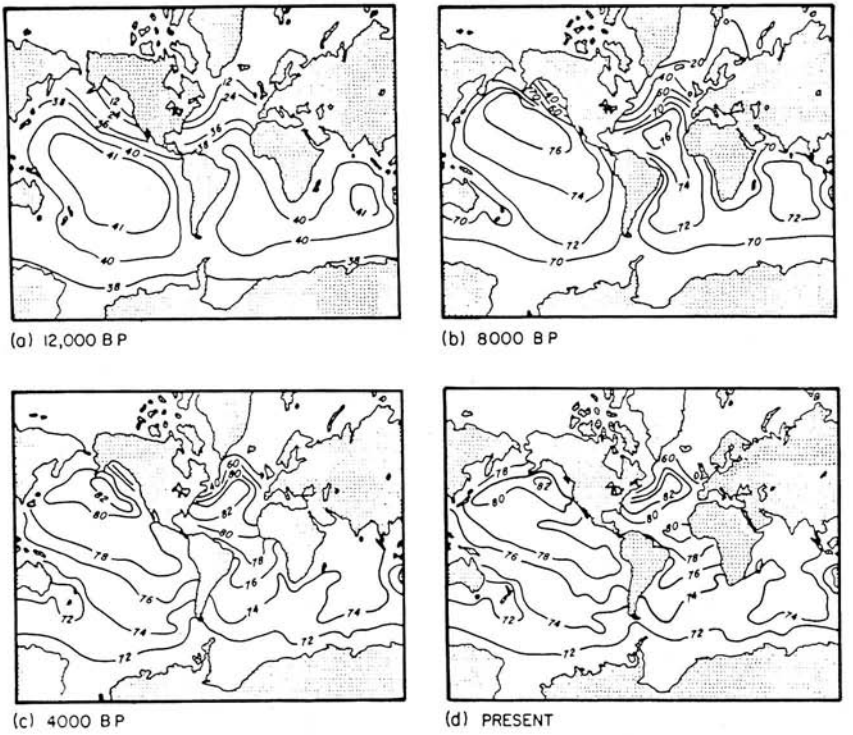

FIG. 22. Four time slices through the solution to the sea level equation for earth model L1 and deglaciation history ICE-2. At each point in the ocean basins the RSL variation is shown in meters.

constructed through the iterative adjustment process described in the last subsection. The global maps of the RSL rise $S(\theta, \phi, t)$ show several important characteristics. Most obvious is the fact that spatial variations of $S(\theta, \phi, t)$ are most rapid in the vicinity of the main deglaciation centers, which is hardly surprising since in this region the function varies from positive values corresponding to peripheral submergence of the land (rise of sea level) to large negative values where the land is uplifted. We have not contoured the negative $S(\theta, \phi, t)$ regions which cover the ice centers, since the amplitudes of emergence are so large that they would completely swamp the sea level variations in the global ocean in a constant-interval contour representation of the field. Inspection of Fig. 22 also shows that as uplift takes place in the once ice covered region a peripheral bulge of water initially propagates toward the ice centers from the far field. This is due to the corresponding migration of the peripheral bulge of the solid part of the planet which is

visible in the disk load response patterns shown in Fig. 17. Also of interest in Fig. 22 is the fact that the increase of water thickness in the far field of the ice sheets is not a strong function of spatial position. This demonstrates *a posteriori* the internal self-consistency of our use of far-field RSL data to estimate the integrated mass loss history of the main ice sheets.

Based upon such global RSL solutions, we may divide the surface of the world's oceans into a number of different zones, in each of which the RSL signature has a more or less characteristic form. The zone boundaries obtained from the RSL data in Fig. 22 for the ICE-2 deglaciation history and the L1 viscoelastic model of the interior are shown in Fig. 23. Zone I consists of the deglaciated regions in which the RSL record consists of continuous emergence following disappearance of the ice. Zone II is the region peripheral to the ice sheet in which all relict beaches are drowned and in which the record is one of monotonic submergence. The RSL signature at sites on the boundary between zones I and II turns out to be quite diagnostic of the viscosity of the deep mantle, as we will show. In this region observed RSL histories are such that, whereas no raised beaches presently exist, the initial sense of the vertical motion following melting was of emergence. This was later followed by submergence, however, so that the RSL histories in this region are not monotonic. The sea level histories in zone III are characterized by delayed emergence following the end of the deglaciation phase.

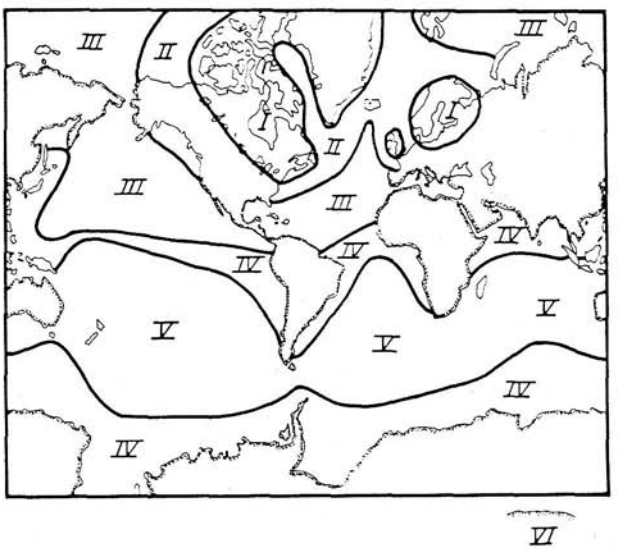

FIG. 23. Relative sea level zone boundaries for earth model L1 and deglaciation history ICE-2. The characteristic signatures of RSL within each of these zones are discussed in the text.

Figure 23 shows a much broader zone III than that found by Clark *et al.* (1978), presumably due to the presence of the lithosphere in our model which was absent in the previous calculations. Zone IV is a region of present-day emergence, which in Fig. 23 is seen to consist only of a fairly narrow region off the west coast of Africa. It is interesting to note that the observed RSL data along the west coast of Africa (Fauré, 1978) do show just this sort of transition from a region of submergence to a region of emergence and then to a region of submergence again in the vicinity of Dakar, Senegal as shown in Fig. 23. The signature of the RSL data in zone V is the appearance of a raised beach immediately after melting ceases. For viscoelastic model L1, Fig. 23 shows a smooth transition between zones III and V in the Pacific, with no zone IV separating them. Zone VI consists of all continental shorelines which are sufficiently remote from the main deglaciation centers. The RSL histories at sites in such regions are only very weakly dependent upon the mantle viscosity profile and are characterized by emergence forced by the offshore water load after melting stops. Such continental shorelines are on the bulge peripheral to the water load.

It must be kept clearly in mind that although the causes of the characteristic RSL signatures in zones III, V, and VI are somewhat different, the signatures themselves are really quite similar and it is often difficult in practice to assign a given site unambiguously to one of these regions. The utility of the classification of sites employed by Clark *et al.* (1978) is therefore not always evident. Nevertheless, the classification does reflect the RSL behavior as a function of distance from the load which is expected on the basis of the disk load calculations discussed in Section 3.7 and so should reflect the interior viscoelastic structure. In the absence of epeirogenic and tectonic processes, the far-field RSL data would probably be quite diagnostic of deep mantle viscosity, but unfortunately these sources of geological noise are important in many localities and the far-field data are not as useful as one might wish.

4.4. RSL Constraints on the Mantle Viscosity Profile When Initial Isostatic Equilibrium Is Assumed

We may obtain global solutions to the sea level equation such as that shown in Fig. 22 for arbitrary profiles of mantle viscosity and from them obtain predictions from the model of the RSL history to be expected at any point on the earth's surface. We seek to vary the profile in such a way as to obtain a "best fit" to the entire set of RSL data. Although this search procedure may be automated using the methods of Backus and Gilbert (1967, 1968, 1970), we have elected to proceed more cautiously at first in order to convince ourselves that a simple radially stratified model exists

which is capable of reconciling the majority of the observational data. Just as we have *a priori* knowledge of the deglaciation history, so we have *a priori* knowledge of the mantle viscosity profile due to the efforts which have been expended by previous investigators. Among these investigators there evolved a reasonably well developed consensus that the viscosity of the upper mantle is near 10^{21} Pa sec and that the thickness of continental lithosphere is near 120 km. The approach which we will adopt for purposes of the discussion in this article is to keep these properties of the viscoelastic model fixed and to focus our attention upon the question of the extent to which the rebound data are able to constrain the viscosity of the mantle beneath 670 km depth; that is, beneath the solid–solid structural phase transition which occurs there. Since we intend to concentrate the discussion upon the question of the viscosity of the lower mantle, we shall restrict our attention to data from sites near the Laurentide ice sheet. The locations of the sites in zone I from which ^{14}C-controlled RSL histories are available are shown in Fig. 24, whereas sites from zone II are shown in Fig. 25.

In Figs. 26, 27, and 28 we show comparisons of observed RSL data (hatched regions) with predictions of the gravitationally self-consistent viscoelastic model for three mantle viscosity profiles at several of these sites. The first two viscosity profiles are identical with models 1 and 2 shown on Fig. 11, whereas the third differs from model 2 only in that the lower mantle viscosity is 5×10^{22} Pa sec rather than 10^{22} Pa sec. All three models therefore differ from one another only in the viscosity beneath 670 km depth, these viscosities being 10^{21} Pa sec (10^{22} P), 10^{22} Pa sec (10^{23} P) and 5×10^{22} Pa sec (5×10^{23} P) for models 1, 2, and 3, respectively. Comparison of the model predictions with the observations at sites under the ice shown in Fig. 26 demonstrates that the best fit to the majority of the data is obtained with the uniform viscosity model 1, since only this model seems able to fit both the observed *amplitude* of emergence and the relatively low present-day emergence *rate*. The data at most sites show the relatively short relaxation time of about 2000 yr, which was stated previously to be characteristic of most Laurentide locations. The model with lower mantle viscosity of 10^{22} Pa sec in general predicts too great a present-day rate of emergence and too long a characteristic relaxation time, whereas the model with lower mantle viscosity of 5×10^{22} Pa sec fails to predict the total observed emergence and, where it does predict a reasonable present-day emergence rate, fails even more spectacularly to predict the observed relaxation time. The only exceptions to this general pattern are at a few sites in the southwest of Hudson Bay (e.g., Churchill), where some preference for the model with lower mantle viscosity of 10^{22} Pa sec is indicated.

The comparisons shown in Fig. 27 include sites which are close to the ice margin (N.W. Newfoundland, Prince Edward Island, Boston), and these

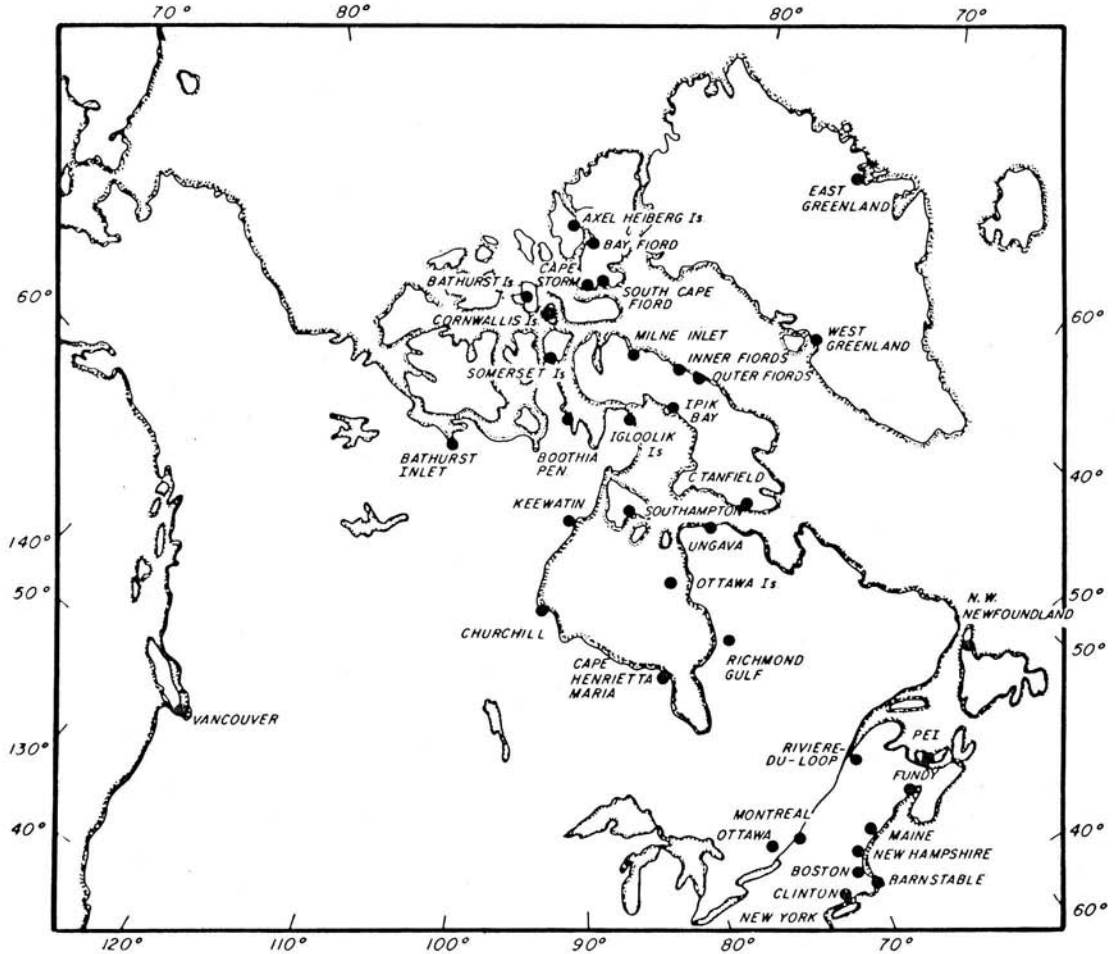

FIG. 24. Location map of Laurentide sites in zone I from which radiocarbon-controlled RSL histories are available.

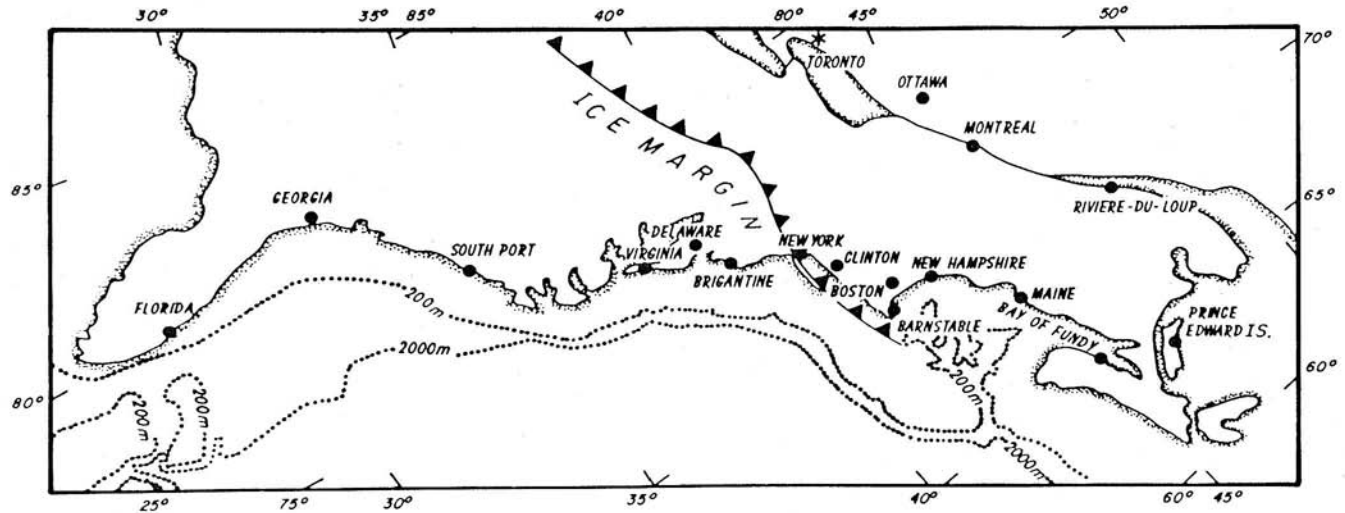

FIG. 25. Location map of Laurentide sites in zone II from which radiocarbon-controlled RSL histories are available.

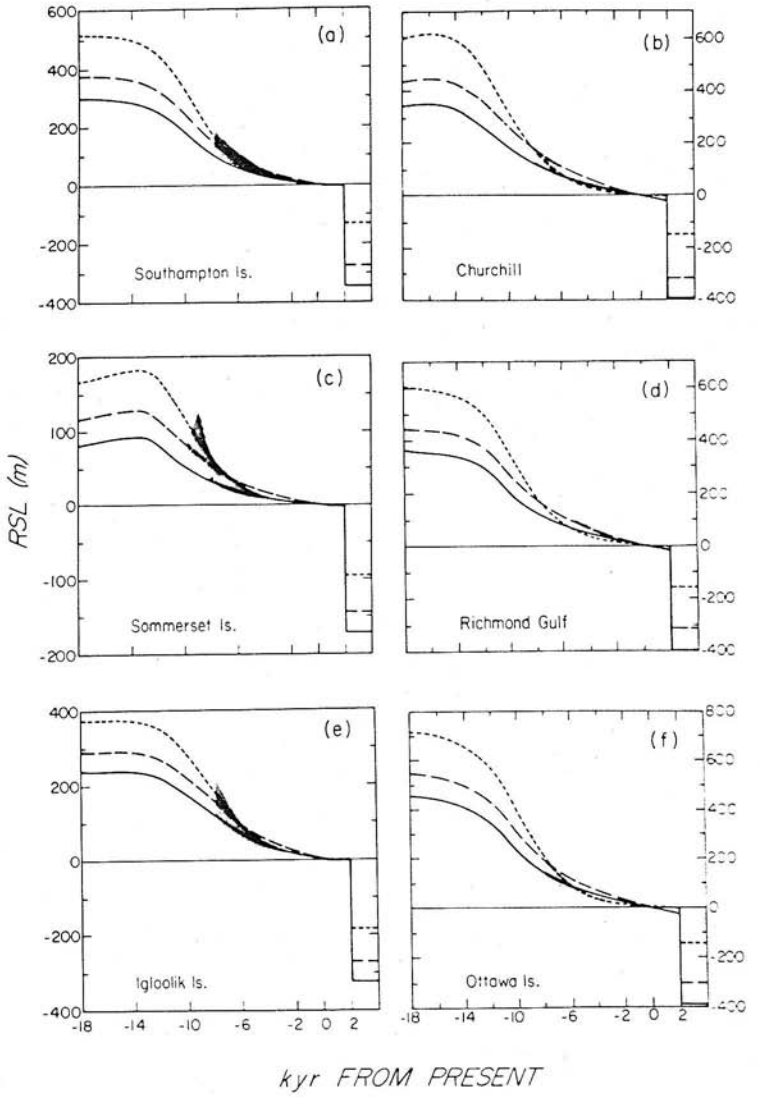

FIG. 26. Relative sea level curves from six sites in zone I near the Laurentide ice sheet. The hatched regions denote the radiocarbon-controlled RSL observations. The dashed, long-dashed, and solid curves are theoretical RSL predictions for models in which the lower mantle viscosity is 10^{22} P, 10^{23} P, and 5×10^{23} P, respectively. The horizontal lines drawn adjacent to the right-hand margin on each plate indicate the amount of uplift remaining for each of these viscosity models.

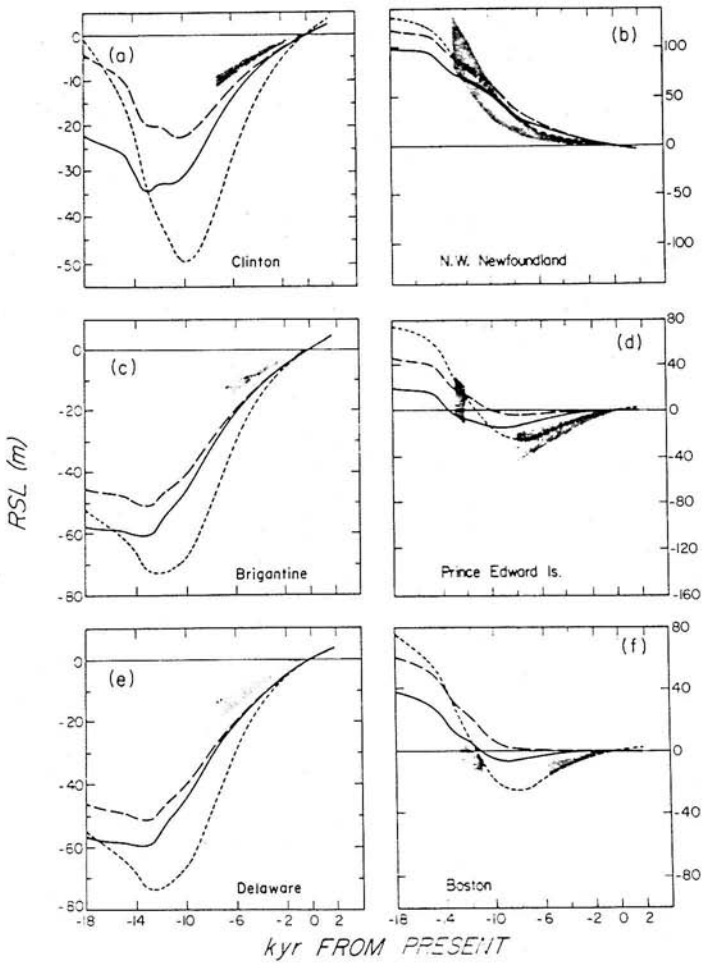

FIG. 27. Relative sea level curves for six sites along the eastern seaboard of North America. For locations see Figs. 24 and 25. Models and data are represented as in Fig. 26.

strongly reinforce the inference drawn on the basis of RSL comparisons near the ice sheet center. Models with any substantial increase of viscosity in the lower mantle fail to match the observations at such locations, since peripheral bulge migration is strongly inhibited in such models, and this is required in order to explain the nonmonotonic RSL histories at sites nearest the boundary between zones I and II (Prince Edward Island, Bay of Fundy, Boston, etc.).

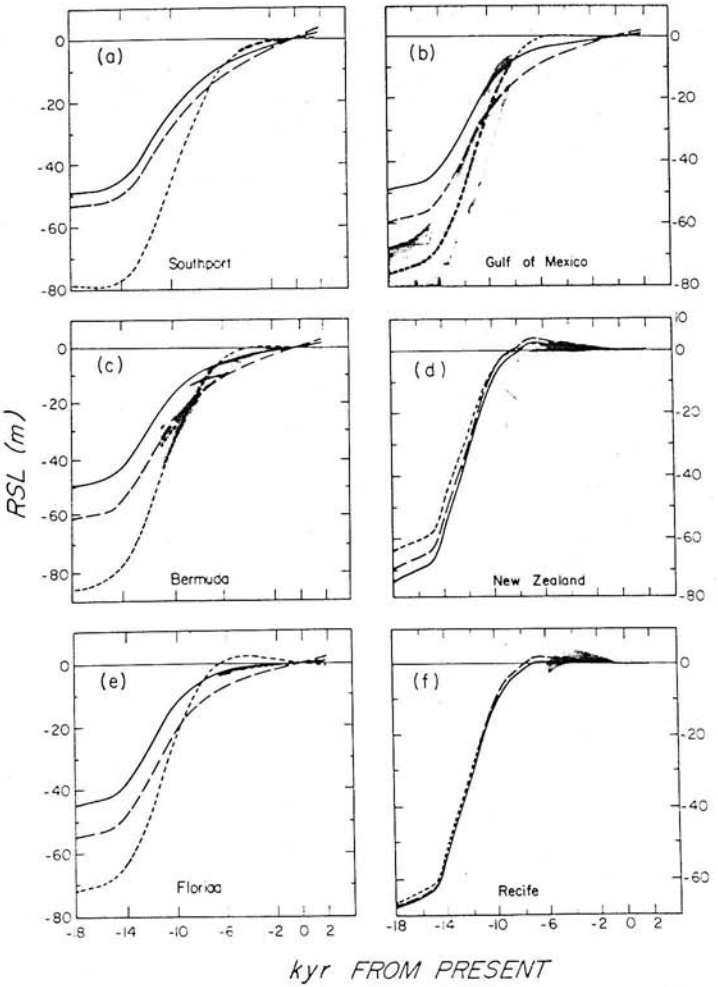

FIG. 28. Relative sea level curves for six sites at increasing distance from the Laurentide ice sheet. Models and data are represented as in Fig. 26.

Figure 28 and the remaining sites on Fig. 27 show comparisons at several of the locations along the East Coast of the United States which are shown on the map in Fig. 25 and at some sites which are considerably more distant from the center of deglaciation. In general, all viscosity models fail to reconcile the data at East Coast sites, since they generally predict excessive submergence (e.g., Southport, Brigantine, Clinton), although the model with

increased lower mantle viscosity of 10^{22} Pa sec is preferred. Both the uniform viscosity model and that with lower mantle viscosity of 5×10^{22} Pa sec are inferior. As discussed in Wu and Peltier (1982b), these misfits could be due to the operation of some epeirogenic process in this region such as that associated with offshore sedimentary loading (Newman *et al.*, 1980), or they could be due to error in the viscoelastic model. As shown in Wu and Peltier (1982b), it is not possible to remedy these misfits by inserting a low-viscosity zone into the model. One additional possibility, which turns out to be correct, is that the misfit could be offset by an increase in lithospheric thickness. Farther still from the Laurentide ice center in the Gulf of Mexico (Fig. 28), the uniform viscosity model is again preferred, since both models with increased lower mantle viscosity predict too little submergence. The same tendency is observed at Bermuda. The final plates in Fig. 28 illustrate comparisons at far-field sites in zone VI. These are for Recife, Brazil and South Island, New Zealand and illustrate the point made previously that the ICE-1(2) model predicts raised beaches to appear at such sites at 8 kyr B.P. rather than 6 kyr B.P., at which time they are actually observed. As suggested in Wu and Peltier (1982b), however, this misfit may be corrected simply by modifying the deglaciation history slightly to include the tail on the melt curve which is observed on the "eustatic" sea level history of Shepard (1963) shown previously in Fig. 20. Inspection of this figure shows that the ICE-1(2) histories are characterized by an abrupt cessation of melting at 5 kyr B.P. If the final disappearance of the Northern Hemisphere sheets were delayed somewhat from that assumed in ICE-1(2) or if some other source of meltwater were still active in the time subsequent to 5 kyr B.P. (such as West Antarctica, for example), then this misfit could be simply corrected.

With the few exceptions mentioned above, the RSL data from the Laurentide region quite strongly prefer the uniform viscosity model over models which have high lower mantle viscosity. As we will show in the following two sections of this article, this is a conclusion which is further reinforced when other data associated with isostatic adjustment are considered. The first such additional kind of information we will discuss is that contained in the variation of the surface gravitational acceleration over deglaciation centers.

5. Deglaciation-Induced Perturbations of the Gravitational Field

As mentioned in the introduction to this article, the apparent inability of previously constructed linear viscoelastic models of isostatic adjustment to simultaneously explain both RSL and free-air gravity data has led to

suggestions to the effect that the basic rheological constitutive relation on which such models are predicated could be completely in error. In this section we will show that when the new theory of glacial isostatic adjustment developed in Sections 3 and 4 is employed to predict the free-air gravity anomaly which should be observed over Hudson Bay, then we obtain agreement with the observed anomaly for the same mantle viscosity profile which is required to fit the RSL data. We are therefore able to fully resolve an important question which has remained unanswered in the literature, and at the same time to seriously undercut previous objections to the use of linear viscoelastic models and to the inference obtained from them that the viscosity of the mantle is rather uniform. The ability of the new theoretical model to solve the problem is due to the fact that it includes the complete spectrum of normal modes of viscous gravitational relaxation which is supported by the radial elastic structure of realistic earth models. As discussed in Section 3.6, the model with uniform mantle viscosity which so well explains the observed record of sea level variations during the past 20,000 yr, a record which is dominated by rather short relaxation times, also supports normal modes with long relaxation times due to the internal density jumps which are associated with the presence of solid–solid phase transitions at the base of the upper mantle. Although the sea level record is dominated by the shortest relaxation times in the complete spectrum, the free-air gravity anomaly depends critically upon the extent to which the modes with long relaxation time are excited. Because the relaxation spectrum of realistic viscoelastic earth models contains modes with relaxation times on the order of 10^5 yr, and since this time scale is of the same order as the time between successive interglacials (Broecker and Van Donk, 1970), we must also consider the validity of the assumption of initial isostatic equilibrium on the basis of which the previously described calculations of RSL history were performed. Before addressing these questions we will first describe the free-air gravity observations over the main centers of postglacial rebound.

5.1. *Satellite and Surface Observations of the Gravity Field over Deglaciation Centers*

In Fig. 29 we have reproduced a global map of geoidal heights based upon the GEM 10 data set and the spherical harmonic coefficients of degrees 2–22. This map represents mean sea level over the world's oceans, while over the continents the geoidal heights are those which would obtain if the continents were cut by a web of thin canals. The anomalies shown on this map are those referred to a reference sphere and are based almost entirely upon satellite observations, although some terrestrial data have also been

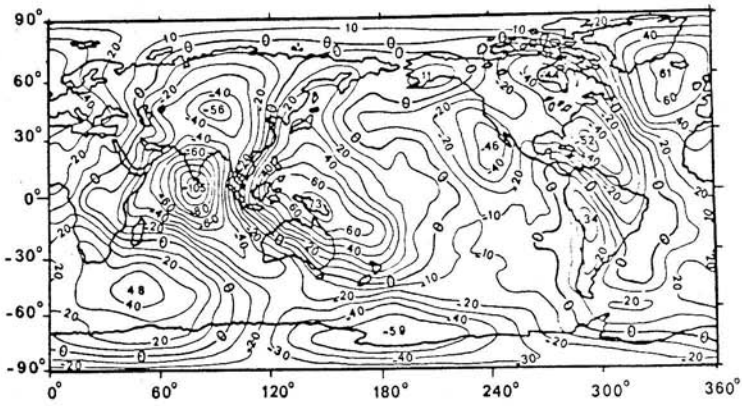

FIG. 29. Global map of geoidal heights based upon the GEM 10 data set and spherical harmonic coefficients of degrees 2–22.

included. Inspection of this map reveals the presence of a global pattern of anomalies with scales on the order of thousands of kilometers and amplitudes varying from −105 m over the Indian Ocean to +70 m over the southwest Pacific. Of particular interest to us for present purposes is the anomaly of −44 m over Hudson Bay. Although this anomaly is very well correlated with the previously shown map of Laurentide ice topography (Fig. 21), and is therefore most probably associated with deglacial forcing, when we seek a similar feature over Fennoscandia (top left-hand corner of the map) we find no negative anomaly present at all. The difficulty clearly has to do with the fact that the magnitude of the anomalies associated with deglaciation are on the same order as those associated with mantle convective processes. It might well be, as pointed out in Peltier (1980a) and previous papers, that the isostatic adjustment model can be used as a filter to remove from the global map of geoidal heights the anomalies which are known to have a deglacial cause and thereby to reveal more clearly the convection-related patterns. Before we can carry out this global filtering, however, we have to convince ourselves of the ability of the isostatic adjustment model to correctly predict the amplitude and form of the anomalies over the glaciation centers. In order to do this we will have to consider the more accurate representation of these anomalies which is obtained from surface data.

In Fig. 30 we show in parts a and b the free-air gravity anomaly maps constructed by Walcott (1970) and Balling (1980) for the Laurentide and Fennoscandia regions, respectively. The map for Laurentide is based on the surface data of Innes *et al.* (1968), which were averaged on 1° × 2° grid elements to remove the influence of local topographic variations and near-

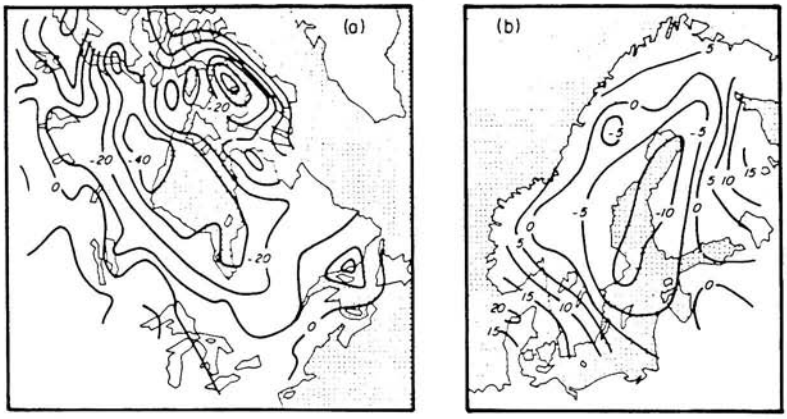

FIG. 30. Free-air gravity anomaly maps for the Laurentide (a) and Fennoscandia (b) regions. The contours are in mGal. Data sources are discussed in the text.

surface geological structure. Each of the grid elements typically contained about 100 separate observations over land and 40 observations over water (Hudson Bay). Inspection of Fig. 30a shows that the anomalous structure which remains consists of an elongated elliptical trough trending roughly NW with a peak amplitude near −35 mGal. Walcott (1972) has previously cautioned that since the Hudson Bay is itself a Phanerozoic basin, the anomaly actually associated with current glacial disequilibrium could be as much as 10 mGal more negative than shown in Fig. 30a. This must be considered somewhat speculative, however, and for the purposes of the following discussion we will generally assume that the anomaly to be fit by the isostatic adjustment model has its −30 mGal contour surrounding Hudson Bay.

Interpretation of the gravity field over Fennoscandia is considerably more complicated than it is for the Laurentide region, because of the combined effects of topography and local near-surface geology on the same spatial scale as that of the ice sheet itself and because the feature related to deglaciation seems also to be biased by the local long-wavelength background. The analysis of this field by Balling (1980) is the most careful which is presently available and is based upon the raw data of Honkasolo (1963). By direct regression analysis, Balling removed from the raw anomalies the spatial part which was linearly related to the topography to obtain the residual map shown in Fig. 30b, which reveals a peak anomaly somewhat in excess of −10 mGal which is very well correlated with the topography of Fennoscandian ice illustrated previously in Fig. 21. The analysis provided by Balling suggests that this anomaly has been biased by +5 to +10 mGal due to the large-scale variations, and he concludes that the anomaly rep-

resentative of the current degree of isostatic disequilibrium is between −15 and −20 mGal. Walcott (1972) accepts an estimate of −17 mGal for the magnitude of the anomaly related to deglaciation, and we will take this as the observed peak anomaly which our isostatic adjustment model must be expected to reproduce.

In the following subsection we will begin to test this model in terms of disk load approximations to the actual deglaciation chronologies.

5.2. *Disk Load Approximations and the Effect of Initial Isostatic Disequilibrium*

Just as disk load approximations to the actual deglaciation histories were applied in Section 3.6 to compute approximations to the RSL data in the form of histories of radial displacement, so here we will make use of the same methods to estimate the gravity anomalies to be expected from the more realistic calculations. Free-air gravity signals may be computed in exactly the same way as we previously computed radial displacement, the sole difference being that we employ the Green's function for the free-air anomaly given in Eq. (3.39). Convolution of this Green's function over a circular disk with parabolic height profile which approximates the Laurentide ice sheet produces the response shown in Fig. 31 when the impulse

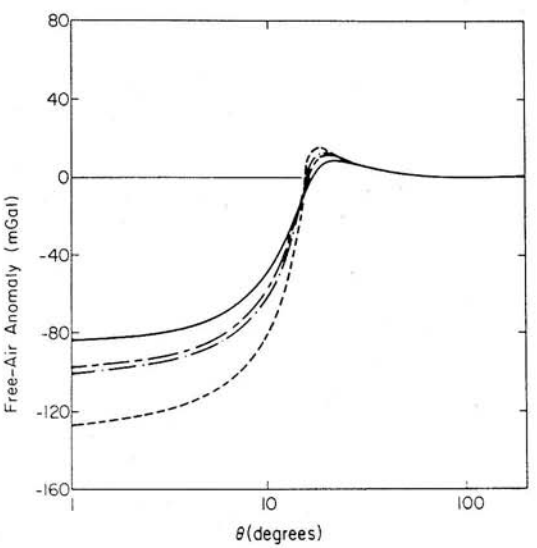

FIG. 31. Free-air gravity anomaly as a function of time forced by a parabolic disk load approximation to the Laurentide ice sheet which is applied instantaneously at $t = 0$. The times are (——) t = 4 kyr; (– – –) t = 8 kyr; (– · –) t = 12 kyr; (· · ·) $t = \infty$ kyr.

TABLE IVa. Δg FOR LAURENTIDE AND VISCOSITY MODEL L1

Time (kyr)	Δg: Load added at $t = 0$ (mGal)	Δg: Equilibrated load removed at $t = 0$ (mGal)	Δg: Nonequilibrium load removed at $t = 0$ (mGal)
0	0	−127	−99
4	−84	−43	−29
8	−98	−29	−16
12	−100	−27	−14
16	−127	−27	−14
∞	−127	0	0

response function used is that for viscosity model L1. This figure shows the time-dependent anomaly which would exist if the planet were initially in equilibrium and the load applied at $t = 0$; clearly the gravity anomaly reaches a maximum in the limit of infinite time. In order to obtain the anomaly which would be observed if the load were *removed* instantaneously, *after* having been resident on the surface for infinite time, we need only subtract from the results shown on Fig. 31 the infinite-time anomaly itself. The importance of having accurate calculations of the isostatic asymptotes of the Love number spectra (as discussed in Section 3.4) for the free-air gravity calculations should therefore be clear. Some numerical results for the time dependence of the peak anomaly produced by the Laurentide disk load are tabulated in Tables IVa and IVb for models L1 and L2 respectively. Since the phase of most rapid deglaciation occurs at about 12 kyr B.P. according to Shepard's eustatic curve (Fig. 20), inspection of this table shows that model L1 predicts the present-day anomaly reasonably well (−27 mGal) when initial isostatic equilibrium of the loaded surface is assumed. Model L2, however, the corresponding results for which are shown in Table IVb, predicts a present-day free-air anomaly of −64 mGal, which is so much larger than the observed anomaly of about −30 mGal (Fig. 30a) that the model must be completely rejected.

TABLE IVb. Δg FOR LAURENTIDE AND VISCOSITY MODEL L2

Time (kyr)	Δg: Load added at $t = 0$ (mGal)	Δg: Equilibrated load removed at $t = 0$ (mGal)	Δg: Nonequilibrium load removed at $t = 0$ (mGal)
0	0	−127	−86
4	−33	−94	−65
8	−51	−76	−53
12	−63	−64	−43
16	−71	−56	−36
∞	−127	0	0

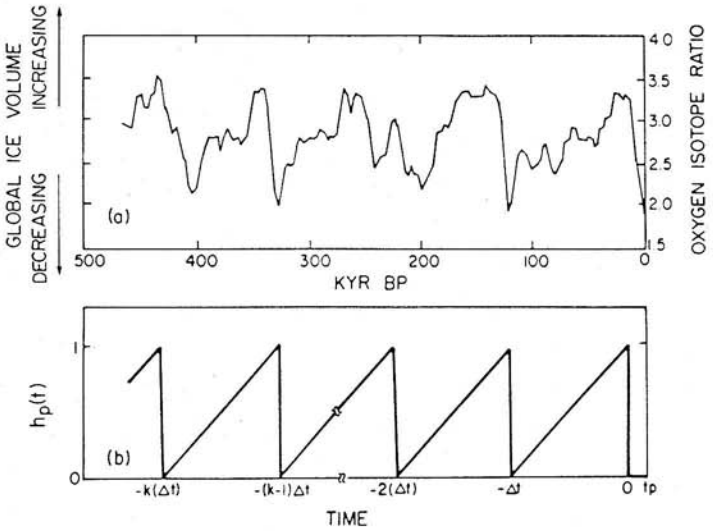

FIG. 32. (a) Oxygen isotope stratigraphy from a typical deep-sea sedimentary core showing the ratio $^{16}O/^{18}O$ as a function of time and the implied variation of continental ice volume. (b) A sawtooth approximation to this time series which accentuates the 10^5-yr periodicity in the record of ice volume fluctuations and the large discrepancy between the time scales of accumulation and disintegration.

These initial results serve to demonstrate that the free-air gravity anomaly expected for the uniform mantle viscosity model is very much larger than that predicted by previous viscoelastic theories of glacial isostasy. The reason for this was previously explained as being due to the fact that realistic viscoelastic models of the planet support modes of relaxation with much longer time scales than previously recognized. On the basis of the above comparisons of the predictions of models L1 and L2 it also seems quite likely that the observed free-air gravity anomaly over the Laurentide region will prove to be even more diagnostic of the viscosity of the deep mantle than the RSL data themselves. In order to make full use of this datum, however, we are forced to address the question of the validity of the assumption of initial isostatic equilibrium upon which the above-described disk load calculations were based.

In order to assess the validity of the assumption, however, we require direct information concerning the actual time scale of the glaciation cycle. It is fortunate for our purposes that such information has been recently forthcoming from studies of deep-sea sedimentary cores taken in the major ocean basins during the course of the Deep Sea Drilling Project (DSDP). The data of interest here are measurements of the ratio of the concentrations of the stable isotopes of oxygen ($^{18}O/^{16}O$) as a function of depth in such cores. Although it was originally believed (Emiliani, 1955) that the vari-

ability of this ratio was a direct reflection of Pleistocene temperatures, it was subsequently established (Imbrie and Kipp, 1971) that the isotopic ratio for the most part reflected the variation of Northern Hemisphere ice volume. Broecker and Van Donk (1970) were among the first to establish on the basis of these data that the Northern Hemisphere glacial–deglacial cycle is very nearly periodic with a time scale of approximately 10^5 yr. Kukla *et al.* (1981) have most recently reviewed the characteristic signature of ice sheet growth and disintegration which defines each cycle. This signature, which is also discussed in somewhat greater detail in Hays *et al.* (1976), is characterized by a very slow buildup of the major ice sheets over about 10^5 yr followed by an extremely rapid disintegration. This suggests that a reasonably good approximation to the long time scale ice volume fluctuations would be the sawtooth waveform shown in Fig. 32b which is compared to the $^{18}O/^{16}O$ record in Fig. 32a. Given this information on the previous history of loading and unloading of the Laurentide and Fennoscandia regions (there does not appear to have been any significant geographical migration of successive ice center locations) we may proceed to address the question of the importance of initial disequilibrium upon the inference of deep mantle viscosity from isostatic adjustment data.

As shown in Section 3, all of the viscoelastic impulse response Green's functions may be written in the form

$$G(\theta, t) = G^{E}(\theta)\,\delta(t) + \sum_{l=0}^{\infty} \sum_{j=1}^{M} r_j^l e^{-s_j^l t} P_l(\cos\theta) \tag{5.1}$$

where l is spherical harmonic degree, $1/s_j^l$ is the relaxation time for the jth mode of the lth harmonic, and r_j^l is the initial "viscous" amplitude. If we denote by $L(\theta, t)$ the load at location θ and time t then the response at time t is just

$$u(\theta, t) = \int_{-\infty}^{t} G(t - t') * L(t')\,dt' \tag{5.2}$$

where the $*$ denotes spatial convolution over the loaded surface. Suppose that at $t = 0$ the load at location θ is $h_0(\theta)$, whereas for $t < 0$ the "prehistory" of loading is $L_p(\theta, t)$, and for $t > 0$ until the present time the loading history may be represented by $h_0 + h(\theta, t)$, i.e.

$$\begin{aligned} L(\theta, t) &= L_p(\theta, t), & t < 0 \\ &= h_0 + h(\theta, t), & t \geq 0 \end{aligned} \tag{5.3}$$

with $L_p(\theta, 0) = h_0(\theta)$ and $h(\theta, 0) \equiv 0$. For $t > 0$ we may therefore expand Eq. (5.2) as

$$\begin{aligned} u(\theta, t) = &\int_{-\infty}^{0} G(t - t') * L_p(t')\,dt' + \int_{0}^{t} G(t - t') * h_0\,dt' \\ &+ \int_{0}^{t} G(t - t') * h(t')\,dt' \end{aligned} \tag{5.4}$$

Now the second term on the right-hand side of Eq. (5.4) may be identified with the spatial convolution of the Heaviside form of the Green's function with the initial surface load $h_0 * G^{\mathrm{H}}(t)$. The third term, on the other hand, is the response to the deglaciation phase of the load cycle. This term would be equal to $-h_0 * G^{\mathrm{H}}(t)$ if all the load were removed instantaneously. The first term on the right-hand side of Eq. (5.4) is the response due to the history of loading prior to $t = 0$. Using Eq. (5.2) it may be rewritten as (Wu and Peltier, 1982a)

$$\int_{-\infty}^{0} G(t - t') * L_{\mathrm{p}}(t')\, dt' = \sum_{l=0}^{\infty} \sum_{j=1}^{M} F_j^l(\theta) \frac{r_j^l}{s_j^l} e^{-s_j^l t} \tag{5.5}$$

where

$$F_j^l = \int_{-\infty}^{0} P_l * L_{\mathrm{p}}(t') s_j^l e^{s_j^l t'}\, dt' \tag{5.6}$$

Equation (5.6) may be considerably simplified if each location under the load has the same prehistory, since we may then write

$$L_{\mathrm{p}}(\theta, t) = h_0(\theta) h_{\mathrm{p}}(t)$$

in which case Eq. (5.5) is replaced by

$$\int_{-\infty}^{0} G(t - t') * L_{\mathrm{p}}(t')\, dt' = h_0 * \sum_l \sum_j f_j^l \frac{r_j^l}{s_j^l} e^{-s_j^l t} P_l \tag{5.7}$$

where

$$f_j^l = \int_{-\infty}^{0} s_j^l e^{s_j^l t'} h_{\mathrm{p}}(t')\, dt' \tag{5.8}$$

For such a simple model, the functions f_j^l contain all of the information concerning the prehistory of loading. If the ice sheet had remained on the surface for an infinite length of time prior to melting so that the system was in isostatic equilibrium at $t = 0$, then $h_{\mathrm{p}}(t) = H(t - t_\infty)$, where H is the Heaviside step function. With $t_\infty = -\infty$ it follows from Eq. (5.8) that $f_j^l \equiv 1$, and the total response may be written from Eq. (5.4) as

$$\tilde{u}(t) = h_0 * \sum_l \sum_j \frac{r_j^l}{s_j^l} e^{-s_j^l t} P_l + h_0 * G^{\mathrm{H}}(t) + \int_0^t G(t - t') * h(t')\, dt' \tag{5.9}$$

Using

$$G^{\mathrm{H}}(\theta, t) = G^{\mathrm{E}}(\theta) + \sum_l \sum_j \frac{r_j^l}{s_j^l} (1 - e^{-s_j^l t}) P_l$$

Eq. (5.9) may be rewritten as

$$\tilde{u}(t) = h_0 * \sum_l \sum_j \frac{r_j^l}{s_j^l} P_l + \int_0^t G(t - t') * h(t')\, dt' \tag{5.10}$$

or

$$\tilde{u}(t) = h_0 * G^{\mathrm{H}}(t = \infty) + \int_0^t G(t - t') * h(t')\, dt' \tag{5.11}$$

which shows that the isostatic response to the removal of an equilibrium load at $t = 0$ may be expressed as the sum of the infinite-time (initial) response and that forced subsequently. If the compensated load were removed instantaneously at $t = 0$ then the response for $t > 0$ from Eq. (5.11) would be

$$u(t) = h_0 * G^{\mathrm{H}}(t = \infty) - h_0 * G^{\mathrm{H}}(t) \tag{5.12}$$

This is the expression which was used to compute the gravity anomalies shown in column 3 of Tables IVa and IVb under the assumption that isostatic equilibrium prevails initially.

In order to assess the effect of initial disequilibrium, we may use the general expression (5.4), which gives

$$u(t) = h_0 * \sum_l \sum_j f_j^l \frac{r_j^l}{s_j^l} e^{-s_j^l t} P_l + h_0 * G^{\mathrm{H}}(t) + \int_0^t G(t - t') * h(t')\, dt' \tag{5.13}$$

which may be rewritten in the form

$$u(t) = \tilde{u}(t) - h_0 * E(t) \tag{5.14}$$

where E is the error or correction Green's function

$$E(\theta, t) = \sum_l \sum_j (1 - f_j^l) \frac{r_j^l}{s_j^l} e^{-s_j^l t} P_l \tag{5.15}$$

The total response in Eq. (5.14) may therefore be expressed as the sum of the response which would be observed if the load were initially in equilibrium [$\tilde{u}(t)$] and a correction due to the load prehistory which is expressed as the spatial convolution of the initial load over an "error" Green's function.

In order to determine $E(\theta, t)$ we need the f_j^l which are defined in Eq. (5.8) in terms of the prehistory of loading $h_{\mathrm{p}}(t)$. For the sawtooth prehistory shown in Fig. 32b this function is given by

$$h_{\mathrm{p}}(t) = \frac{t + k\tau}{\tau}, \qquad -k\tau \le t \le -(k-1)\tau \tag{5.16}$$

where $\tau = 10^5$ yr in the characteristic period of a single ice sheet advance. Substitution of Eq. (5.16) into Eq. (5.8) gives

$$\begin{aligned} f_j^l &= \sum_{k=1}^{N} \int_{-k\tau}^{-(k-1)\tau} s_j^l e^{s_j^l t'} \frac{t' + k\tau}{\tau}\, dt' \\ &= \left(e^{-s_j^l \tau} - \frac{1 - s_j^l \tau}{s_j^l \tau} \right) \frac{1 - e^{-N s_j^l \tau}}{1 - e^{-s_j^l \tau}} \end{aligned} \tag{5.17}$$

where N is the number of load cycles in the prehistory. Since the present ice age has continued for 2–3 million yr, a time short compared to the continental drift time scale of 10^8 yr on which significant changes of polar

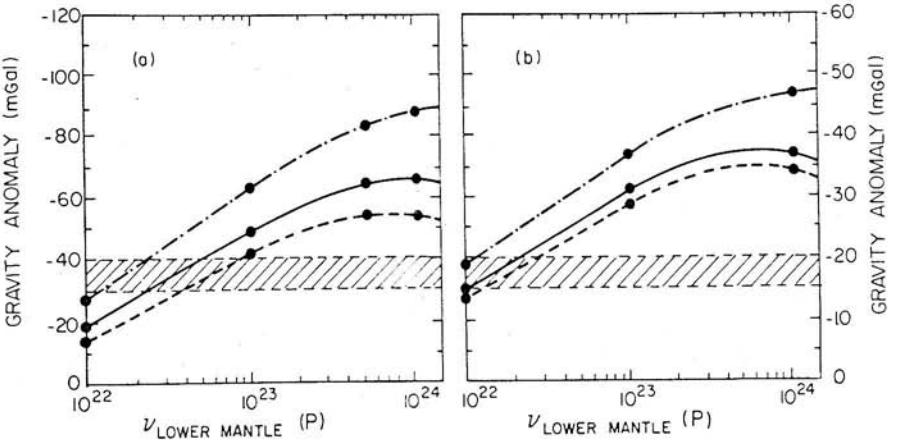

FIG. 33. (a) Present-day peak free-air gravity anomaly at the center of the disk model Laurentide load as a function of the viscosity of the mantle beneath 670 km depth. The viscosity of the upper mantle is held fixed at 10^{22} P. The dash-dotted curve is the prediction assuming initial isostatic equilibrium; the dashed curve includes the effect of initial isostatic disequilibrium but the computation has been done for fixed ice sheet radius. The solid curve is the predicted anomaly when the time dependence of ice sheet radius is accounted for under the assumption that the ice cap maintains an equilibrium plastic profile at all times. The hatched region shows the observed peak anomaly over Hudson Bay. (b) Precisely the same analysis for the Fennoscandia region.

continentality can be expected to have occurred, yet long compared to the duration of a given glacial epoch (10^5 yr), we may safely assume $N = 20$–30 in evaluating Eq. (5.7). We note from the form of Eq. (5.17) that if $s_j^l\tau$ is large, which is to say that the characteristic relaxation time is short compared to the time scale of ice sheet advance, then $f_j^l \approx 1$ and the mode (j, l) is very nearly in isostatic equilibrium at $t = 0$. If $s_j^l\tau \approx 1$ then $f_j^l \approx 0.58$, provided $N > 2$, and the response in this mode would be just that for a reduced load $0.58h_0(\theta)$ which was initially in equilibrium. If, however, $Ns_j^l\tau \ll 1$ then $f_j^l \approx Ns_j^l\tau/2$ and by $t = 0$ the response is but a small fraction of the equilibrium value.

In column 4 of Tables IVa and IVb we show the peak free-air gravity anomaly at the center of the model Laurentide disk as a function of time for models L1 and L2 including sawtooth prehistory with $\tau = 10^5$ yr and $N = 30$ ($N = 20$ gives almost identical results). Comparing columns 3 and 4 shows that the correction for prehistory at $t = 12$ kyr is about 13 mGal for L1 and 27 mGal for L2. The calculations therefore demonstrate that the effect of initial isostatic disequilibrium is extremely important insofar as free-air gravity anomaly calculations are concerned. In Fig. 33a we present the results of a more detailed investigation of the effect of initial disequilibrium on the free-air gravity anomaly to be expected over Hudson Bay.

This diagram shows the present-day peak free-air gravity anomaly at the center of the Laurentide model disk load as a function of the viscosity of the mantle beneath 670 km depth. The prediction is shown both including and excluding the effect of prehistory and is compared to the observed free-air anomaly of about −35 mGal (hatched region). Inspection of this figure shows that when initial isostatic equilibrium is assumed, the model with uniform mantle viscosity of 10^{22} P fits the observed free-air anomaly very well. Under this assumption, as the viscosity of the lower mantle increases the predicted free-air anomaly increases monotonically to approach an asymptotic value near 100 mGal. If the assumption of initial equilibrium were valid, therefore, the viscosity of the lower mantle could not be significantly in excess of the upper mantle value. Otherwise one would predict a free-air anomaly much larger than is observed.

Even with a lower mantle viscosity as high as 10^{23} P as in model L2, however, characteristic relaxation times are no longer short compared to the time scale of 10^5 yr which separates successive interglacials and the assumption of initial isostatic equilibrium is invalid. The second and third curves on Fig. 33a show the predicted present-day free-air gravity anomaly for the model Laurentide load including the influence of initial isostatic disequilibrium. In this case the predicted anomaly is not a monotonically increasing function of the deep mantle viscosity. Rather we may fit the observation for either of two widely spaced values of lower mantle viscosity, one near 3×10^{22} P and the other near 5×10^{25} P. The latter exists as a possible solution because, in the theoretical model, one may trade off the degree of initial disequilibrium against the magnitude of the viscosity in the lower mantle. To the extent that RSL data are relatively unaffected by initial isostatic disequilibrium, however, this solution may be completely ruled out on the basis of the preceding discussion of RSL data in Section 4, and the only acceptable solution is the lower value.

It is an extremely important property of the isostatic adjustment data set that RSL data and free-air gravity data complement each other in this way. The explanation of the complementary nature of these two types of data is to be found in the fact that sea level histories are effectively measurements of radial displacement relative to the zero datum established by local present-day mean sea level. These data therefore provide no information concerning the amount of uplift (submergence) which has yet to take place before isostatic equilibrium is restored. The free-air gravity anomaly, on the other hand, is an absolute measurement of the degree of current disequilibrium, and it is for this reason that the two types of observation are influenced to a completely different extent by initial isostatic disequilibrium. This may be shown algebraically by using Eq. (5.14) to compute

$$u(t) - u(t_p) = \tilde{u}(t) - \tilde{u}(t_p) - h_0 * [E(t) - E(t_p)] \tag{5.18}$$

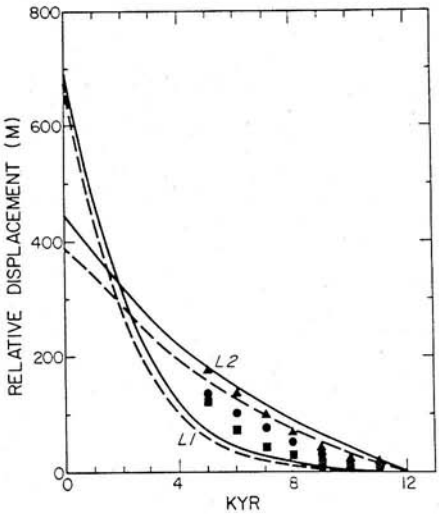

FIG. 34. Radial displacement response at the center of the Laurentide model disk load for viscoelastic models L1 and L2. The solid curves are for calculations done under the assumption of initial isostatic equilibrium, whereas the dashed curves include the degree of initial disequilibrium implied by the oxygen isotope data. Also shown on this figure are data from three sites around Hudson Bay: (▲) data from Castle Island; (●) data from Churchill; (■) data from the Ottawa Islands.

where t_p is the present time, so that Eq. (5.18) gives the response relative to a zero datum at present and therefore correctly mimics RSL information. The correction of the relative displacement response for the effect of initial disequilibrium is given by the third term on the right-hand side of Eq. (5.18) in the form of a convolution of the initial load over a difference of error Green's functions. From Eq. (5.15) the expression in square brackets in Eq. (5.18) is

$$E(t) - E(t_p) = \sum_{l=0}^{\infty} \sum_{j=1}^{M} (1 - f_j^l) \frac{r_j^l}{s_j^l} e^{-s_j^l t} [1 - e^{-s_j^l (t_p - t)}] P_l \qquad (5.19)$$

which is obviously zero for $t = t_p$. Comparison of Eq. (5.19) with Eq. (5.15) shows that every term in Eq. (5.19) is smaller than the corresponding term in Eq. (5.15) by the factor $\{1 - \exp[-s_j^l(t_p - t)]\}$. The magnitude of the effect is shown in Fig. 34, where we plot the relative radial displacement response at the center of the Laurentide disk for models L1 and L2 both including and excluding the effect of initial isostatic disequilibrium (solid and dashed lines respectively). Inspection of this figure clearly shows that the effects of initial disequilibrium upon the predictions of either viscosity model are much less than the differences in response due the viscosity models themselves. This is an extremely important point since it assures

us that viscosity models rejected on the basis of RSL calculations done assuming initial isostatic equilibrium cannot be brought back into contention by invoking this effect. Also shown on Fig. 34 are the RSL data from the Ottawa Islands in Hudson Bay and from two other sites near the center of rebound. These data all lie between the predictions of models L1 and L2, implying that the lower mantle viscosity is between that in these two models. This is the same conclusion reached on the basis of the previously discussed free-air gravity data which prefer a value of the lower mantle viscosity near 3×10^{21} Pa sec.

Figure 33b shows a comparison of disk load predictions of the peak free-air gravity anomaly, with and without the effect of initial disequilibrium, for the model Fennoscandian load. Inspection of this figure confirms the conclusions reached on the basis of the Laurentide analysis. When the effect of initial isostatic disequilibrium is included, the model with lower mantle viscosity of about 2×10^{22} P predicts the observed present-day free-air anomaly of about -17 mGal quite accurately. The fact that both the Laurentide and Fennoscandia data require the same contrast of viscosity across the phase transition at 670 km depth in the mantle strongly reinforces the necessity of including this feature in the viscosity profile, establishes the feature as a global property of the real earth, and reinforces our "faith" in the assumptions upon which our realistic viscoelastic models of the earth are based.

The model which we have employed here to investigate the influence of initial isostatic disequilibrium upon free-air gravity and RSL predictions assumes, through the expression $L_p(\theta, t) = h_0(\theta)h_p(t)$, that the ice sheet radius remains constant while its volume expands and contracts. This is of course not strictly true, since ice sheets expand and contract in their horizontal dimensions as volume increases and decreases. As discussed in Wu and Peltier (1982b), however, when one uses the flow law of ice to fix the variations of ice sheet scale given the characteristic volume fluctuations shown in Fig. 32b, one finds that the assumption of fixed ice sheet radius actually tends to exaggerate somewhat the importance of initial isostatic disequilibrium. This reference should be consulted for a more detailed analysis of this effect. In Fig. 33a,b calculations of the peak free-air anomalies at the center of the Laurentide and Fennoscandia disks are also shown which include the influence of expansion and contraction of the disk radius and which demonstrate this effect.

5.3. Free-Air Anomalies from the Self-consistent Model

Figure 35a.b shows free-air gravity maps for the Laurentide region predicted from the gravitationally self-consistent theory for viscoelastic models L1 and L2, respectively. All of these calculations have been done under the

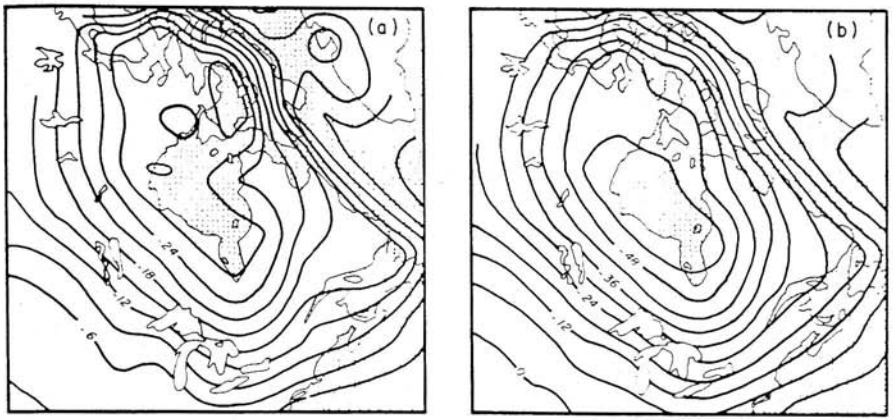

FIG. 35. Predicted present-day free-air gravity maps for the Laurentide region. Parts (a) and (b) are calculations based upon viscoelastic models L1 and L2, respectively. Both calculations assume that isostatic equilibrium prevails initially.

assumption that isostatic equilibrium prevails initially, and comparison of the peak anomalies on these maps with the corresponding disk load predictions in Fig. 33a shows that the disk load approximations are extremely accurate. Therefore, none of the arguments based upon the disk load analyses will require substantial modification in consequence of application of this more accurate model to calculation of free-air gravity anomalies. As discussed in Wu and Peltier (1982b), this general conclusion also applies when the effect of initial isostatic disequilibrium is included. The fact that the free-air gravity anomalies predicted by the new theory did fit the observations over the Laurentide region was first demonstrated in Peltier (1981a).

5.4. *Gravity Field Constraints on the Mantle Viscosity Profile*

The few results discussed in the preceding subsections suffice to make the important point that the new theory of isostatic adjustment is able to simultaneously explain both observed RSL histories and free-air gravity anomalies associated with the main centers of Pleistocene deglaciation. No previous analysis of postglacial rebound has achieved this rather important goal. The fact that our realistic linear viscoelastic models are able to reconcile both data sets simultaneously means that there is no evidence in the adjustment data themselves for non-Newtonian or other exotic material behavior. The crucial ingredient which was missing in all previous formulations of the theory is the set of modes with long relaxation times which is

supported by the radial inhomogeneity of the elastic structure of realistic earth models. Of particular importance in this respect are the density jumps in the transition region due to the olivine → spinel and the spinel → perovskite + magnesiowustite phase transitions. With the elastic structure fixed to that of model 1066B of Gilbert and Dziewonski (1975), which was itself based upon the totality of elastic gravitational free oscillations data, our isostatic adjustment calculations show that the free-air gravity anomaly is a particularly sensitive measure of the viscosity of the lower mantle. When the upper mantle viscosity is fixed to 10^{21} Pa sec the free-air data require a lower mantle viscosity very near 3×10^{21} Pa sec, with the Laurentide data apparently providing the most sensitive estimate of this number. The RSL calculations discussed in Section 4 show that this viscosity profile is completely acceptable to the RSL data. In the next section we will go on to consider a third set of isostatic adjustment data which are able to provide an extremely useful further corroboration of the validity of this inferred viscosity profile.

6. Deglaciation-Induced Perturbations of Planetary Rotation

Given the mass contained in the Laurentian and Fennoscandian ice complexes it should not be too surprising that their melting may have induced very substantial variations in the moment of inertia tensor of the planet. Since the net angular momentum of the solid earth + ice + water system must be conserved during the internal mass redistributions associated with glaciation and deglaciation, it is clear that the changes of the inertia tensor produced by mass redistribution must be accompanied by changes in the angular velocity vector of the system as a whole. As we will show in the following subsections these changes in the angular velocity vector are astronomical observables which may be invoked to constrain the mantle viscosity profile since the history of surface loading is known.

6.1. The Historical Records of Polar Motion and l.o.d. Variation

Since about A.D. 1900 the International Latitude Service (ILS) and more recently the International Polar Motion Service (IPMS) have maintained a set of photo zenith tube (pzt) stations which have provided a more or less continuous record of the monthly mean motion of the rotation pole relative to the conventional international origin (CIO). These polar motion data are shown in Fig. 36, which is based upon the reduction of ILS data by Vincente and Yumi (1969, 1970) as described in Dickman (1977). The upper and lower time series, respectively, show the polar motion along the y and x

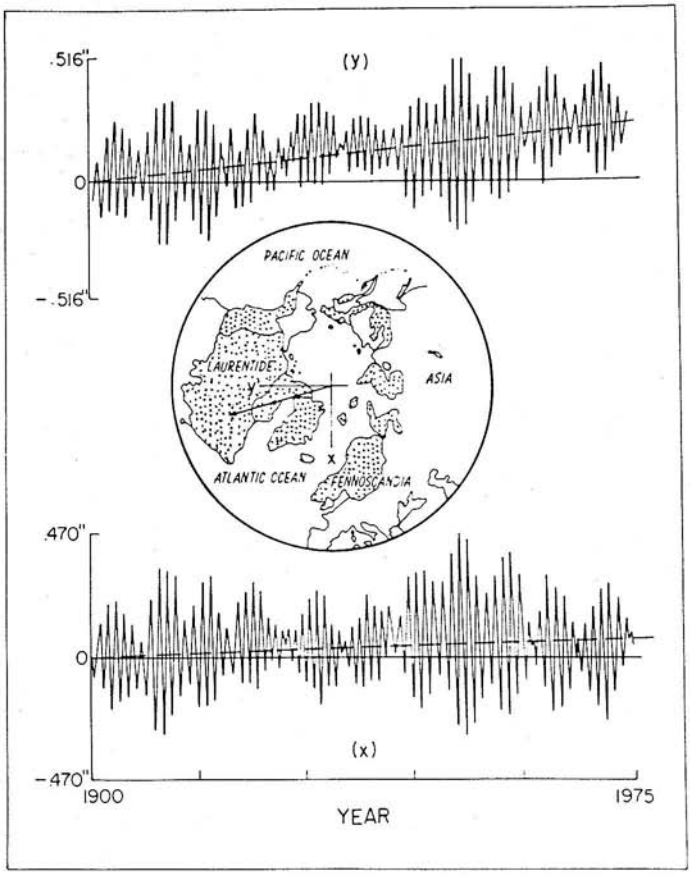

FIG. 36. Polar motion time series for the motion of the rotation pole in the x and y coordinate directions relative to the CIO. The geographic orientation of the coordinate system is shown on the inset polar projection which also shows the location of the Wurm–Wisconsin ice sheets (stippled) at the last glacial maximum. The arrow drawn from the CIO shows the direction of the drift of the rotation pole implied by the secular trend in the ILS pole path which is evident in both the x and y coordinate directions. The rate of drift is about $1''/10^6$ yr.

axes of the CIO coordinates, and the geographic location of these axes is shown on the polar projection at the center of the figure. The x axis passes along the Greenwich meridian, and the y axis along the meridian at long 90° W. Inspection of the polar motion time series shown in this figure shows it to be dominated by a sequence of beats separated by a period of 7 yr. This is precisely the temporal behavior which is expected due to the superposition of the 14-month free Eulerian nutation (Chandler wobble) and the 12-month annual wobble. These oscillatory motions are superimposed,

however, upon a secular drift of the pole with respect to the coordinate system fixed relative to the surface geography. The direction of the mean motion of the pole is shown by the arrow drawn from the center of the CIO system on the polar projection in the center of Fig. 36. That it is directed toward the centroid of the ancient Laurentide ice sheet should make us suspicious that the drift is deglaciation induced. As we will show, this suspicion turns out to be warranted. Given the rather large difference between the mass of the Laurentian and Fennoscandian ice sheets it should hardly be surprising that the Fennoscandian load, which is of smaller mass and centered at higher latitude, does not significantly influence the response. The observed rate at which the rotation pole is drifting toward Hudson Bay is very near $1°/10^6$ yr, and this is the observation which we will attempt to fit with our isostatic adjustment model.

Of equal interest to the above-described mean motion of the pole for our present purposes are historical observations of variations of the length of day (l.o.d.). It is well known that the rotation of the earth is generally decreasing with time at a rate of $(1100 \pm 100)''/\text{century}^2$ (e.g., Lambeck, 1980), due mostly to the torque exerted on the earth by the moon through the agency of lunar ocean tidal dissipation. In order to ensure conservation of angular momentum of the earth–moon system this decrease in the rate of the earth's rotation is accompanied by an increase of the earth–moon distance. Although it is now understood that the current rate of lunar tidal dissipation is anomalously high and unrepresentative of the past because the ocean basins are currently almost resonant with the tidal forcing (Hansen, 1982), the l.o.d. variation forced by lunar tidal friction certainly dominates the observed variation of this quantity now. Besides the l.o.d. change forced by tidal torque, it has been possible to extract from the astronomical record a component of the net l.o.d. change which is not attributable to this cause. This observation is normally referred to as the nontidal acceleration of rotation and has been measured using various methods to obtain the results listed in Table V. The observation by Currot (1966) is consistent with that of Dicke (1966) and is based upon an analysis of ancient solar eclipse data. Based upon an assumption of constant lunar tidal acceleration, one may predict from the orbital equations when each of the ancient solar eclipses should have occurred. Knowledge of when they actually occurred provides a measure of the deceleration of rotation which is not attributable to the operation of tidal torques. Müller and Stephenson (1975) reanalyzed the ancient eclipse data analyzed by Newton (1972), keeping only the observations corresponding to total eclipses or for which the deviation from totality was explicitly declared. The measurement in the table by Morrison (1973) was based upon observed lunar occultations over the time period

TABLE V. MEASUREMENTS OF THE NONTIDAL COMPONENT OF THE ACCELERATION OF ROTATION

Source	Value ($\dot{\omega}_3/\Omega$)
Currot (1966)	$(0.7 \pm 0.3) \times 10^{-10}$ yr^{-1}
Müller and Stephensson (1975)	$(1.5 \pm 0.3) \times 10^{-10}$ yr^{-1}
Morrison (1973)	$(2.9 \pm 0.6) \times 10^{-10}$ yr^{-1}
Lambeck (1977)	$(0.69 \pm 0.3) \times 10^{-10}$ yr^{-1}

1663–1972. It differs significantly from the others. Lambecks's (1977) number was obtained from the difference between the value of the net acceleration given by Müller (1975) and the mean value for the tidal acceleration obtained from an ocean model and astronomical and satellite observations.

In the following subsections we will show that both the secular drift of the ILS–IPMS pole path and the nontidal acceleration of the earth's rotation are effects due to Pleistocene deglaciation. We will furthermore demonstrate that these observations may be employed to constrain the viscosity of the earth's mantle and thus to provide valuable confirmation of the validity of the profile of viscosity deduced on the basis of the previously discussed analyses of RSL and free-air gravity data.

6.2. *The Theory of Deglaciation-Forced Rotational Effects*

If the earth is subject to no external torque, then the principle of angular momentum conservation takes the form of the following Euler equations (e.g., Goldstein, 1980):

$$\frac{d}{dt}(J_{ij}\omega_j) + \epsilon_{ijk}\omega_j J_{kl}\omega_l = 0 \tag{6.1}$$

where the angular velocity ω is referred to a coordinate system whose axes coincide with the initial direction of the principal axes of inertia of the deformable body with moment of inertia tensor J_{ij}. In Eq. (6.1) ϵ_{ijk} is the Levi–Civita alternating tensor. If we can determine the $J_{ij}(t)$ which are produced by the Pleistocene glacial cycle, then Eq. (6.1) could be solved for the unknown ω_i since they would then degenerate to a set of three simultaneous ordinary differential equations. In fact, the inertia tensor J_{ij} contains contributions from two sources which are of interest to us here due, respectively, to the effect of the deformation produced by the basic rotation and that associated with the response of the planet to surface loading by the ice sheets. We will proceed to calculate these distinct contributions.

6.2.1. Perturbations of Inertia Due to Variable Rotation. In order to compute the rotational deformation we will employ the formalism of tidal Love numbers in combination with MacCullagh's formula as described in Jeffreys (1970). If the earth is subjected to a disturbing potential of the form

$$\phi_2(r, s) = \sum_{l=0}^{\infty} \Phi_{2l}(r, s) P_l(\cos\theta) \tag{6.2}$$

where s is the Laplace transform variable, r is the distance from the center of mass, and P_l is the usual Legendre polynomial, this potential will elicit a response $\phi_1(r, s)$ such that

$$\phi_1(r, s) = \Phi_{2l}(r, s) k_l^{\mathrm{T}}(r, s) \tag{6.3}$$

where k_l^{T} is the so-called tidal Love number, which differs from our previously defined load Love number $k_l(r, s)$ in that it is computed for zero normal stress boundary conditions. If the applied potential is the centrifugal potential ψ associated with rotation then

$$\psi = \tfrac{1}{2}[\omega^2 r^2 - (\omega_i x_i)^2] \tag{6.4}$$

which can be split into two terms (e.g., Munk and MacDonald, 1960) as

$$\psi = \tfrac{1}{3}\omega^2 r^2 + \chi \tag{6.5}$$

where

$$\chi = \tfrac{1}{6}[\omega_1^2(x_2^2 + x_3^2 - 2x_1^2) + \cdots - 6\omega_1\omega_2 x_1 x_2] \tag{6.6}$$

is a spherical harmonic of degree two and where the dots denote additional terms obtained by cyclic permutation of the indices. The external gravitational potential V produced by this contribution to the centrifugal potential is, from Eq. (6.3),

$$V = (a/r)^5 \chi(t) * k_2^{\mathrm{T}}(t) \tag{6.7}$$

where the $*$ denotes convolution in time. Now the tidal Love number $k_2^{\mathrm{T}}(t)$ may be obtained from the equivalent time-independent expression for an elastic earth by direct application of the principle of correspondence. For an incompressible, homogeneous earth the elastic tidal Love number (e.g., Munk and MacDonald, 1960) is

$$k_2^{\mathrm{T}} = \frac{3/2}{1 + \bar{\mu}} \tag{6.8}$$

where $\bar{\mu} = 19\mu/2\rho g a$, with μ the elastic shear modulus, ρ the density, a the earth radius, and g the surface gravitational acceleration. For the Maxwell earth the Laplace transform domain expression for the elastic shear modulus (see Section 2) is

$$\mu(s) = \frac{\bar{\mu} s}{s + \bar{\mu}/\nu} \tag{6.9}$$

The Laplace inverse of Eq. (6.8) is then

$$k_2^{\mathrm{T}}(t) = \frac{3/2}{1 + \bar{\mu}} [\delta(t) + \bar{\mu}\gamma e^{-\gamma t}] \tag{6.10}$$

where $\gamma = (\mu/\nu)/(1 + \bar{\mu})$ is the inverse relaxation time of the $l = 2$ harmonic component of the deformation and where ν, as before, is the viscosity of the homogeneous earth model. Introducing the explicit expressions for ϕ and k_2^{T} into MacCullagh's formula we get

$$(G/2r^5)[C_{11}(x_2^2 + x_3^2 - 2x_1^2) + \cdots - 6C_{12}x_1x_2] = (a/r)^5 \chi(t) * k_2^{\mathrm{T}}(t) \tag{6.11}$$

where it has been assumed that $I\,\delta_{ij} + C_{ij}$ are the elements of the inertia tensor of the rotationally deformed sphere. Invoking the fact that a solid harmonic will produce deformations which leave the trace of the inertia tensor C_{ij} invariant (e.g., Rochester and Smylie, 1974), we may equate like terms on each side of Eq. (6.11), using Eq. (6.6) to obtain

$$C_{ij}(t) = \frac{a^5}{2G(1 + \bar{\mu})} \left[\omega_i(t)\omega_j(t) - \frac{\omega^2(t)}{3}\,\delta_{ij} + \bar{\mu}\gamma \int_{-\infty}^{t} \left\{ \omega_i(t')\omega_j(t') - \frac{\omega^2(t')}{3}\,\delta_{ij} \right\} e^{-\gamma(t-t')}\,dt' \right] \tag{6.12}$$

It is a consequence of the incompressibility of the model that the term $\omega^2 r^2/3$ in Eq. (6.5) contributes nothing to the response. To obtain the total inertia of the rotating sphere we have to add to Eq. (6.12) the inertia which the sphere would have in the absence of rotation. This is obtained by assuming that the effect of rotation is to change the moment about the polar axis by an amount $2\Delta/3$ and about the two orthogonal equatorial axes by $-\Delta/3$ (e.g., Burgers, 1955), where Δ is unknown. If we insist that the resulting principal moments equal the observed values C and A then we get the moment of inertia of the nonrotating sphere as

$$I = A + (C - A)/3 \tag{6.13}$$

The total inertia tensor may then be written as

$$J_{ij}(t) = I\,\delta_{ij} + C_{ij}(t) + I_{ij}(t) \tag{6.14}$$

where the I_{ij} are the contributions due to loading effects.

6.2.2. Perturbations of Inertia Due to Surface Mass Loading. The contributions to I_{ij} are due to the ice sheets themselves and to the induced

deformation. Rather than analyze the response to a realistic unloading event such as that described by the ICE-2 model discussed in Section 4, we will content ourselves here with an analysis of disk load approximations to such histories. Since the actual forcing is dominated by the large-scale Laurentide sheet, whose geometry is well known, and since the polar motion depends only upon the $l = 2$ component of the response to this forcing, the disk load approximation will be a rather accurate one. The strategy which we will adopt to calculate the I_{ij} will be to take advantage of the symmetry of the circular cap by calculating I_{ij} in a coordinate system which has the cap on its polar axis; if this inertia tensor is called I'_{ij} then we can find I_{ij} from I'_{ij} by multiplying with an appropriate rotation matrix.

Now an ice sheet with angular radius α and mass M may be described by the following surface density (Farrell, 1972):

$$\sigma^{\mathrm{ICE}}(\theta) = \frac{M}{4\pi a^2}\left[P_0 + \sum_{l=1}^{\infty} \frac{(2l+1)(1+\cos\alpha)}{l(l+1)} \frac{\partial P_l(\cos\alpha)}{\partial \cos\alpha} P_l(\cos\theta)\right] \quad (6.15)$$

where θ is the angular distance from the center of the cap. We may force our simple disk load to mimic a closed hydrological cycle by assuming that there is a defect of mass in a global ocean outside the ice sheet which is of magnitude $-M$ distributed over the area $2\pi a^2(1 + \cos\alpha)$. This global ocean has surface density

$$\sigma^{\mathrm{OC}}(\theta) = \frac{M}{4\pi a^2}\left[-P_0 + \sum_{l=0}^{\infty} \frac{(2l+1)(1-\cos\alpha)}{l(l+1)} \frac{\partial P_l(\cos\alpha)}{\partial \cos\alpha} P_l(\cos\theta)\right] \quad (6.16)$$

Conservation of mass is then assured because the surface integral of $\sigma(\theta) = \sigma^{\mathrm{ICE}} + \sigma^{\mathrm{OC}}$ vanishes.

In the coordinate system $x_1x_2x_3$ which has the center of the ice cap along the x_3 axis and distance a from the origin, the perturbations of inertia due to $\sigma(\theta)$ are

$$I'_{11} = \frac{a^2}{3} L_2 \qquad I'_{22} = \frac{a^2}{3} L_2 \qquad I'_{33} = -\frac{2a^2}{3} L_2 \quad (6.17a)$$

where

$$L_2 = a_2 \int_0^{2\pi} \int_{-1}^{+1} P_2(x)\sigma(x, \phi) f(s)\, dx\, d\phi \quad (6.17b)$$

and we have inserted a factor $f(s)$ which depends upon the Laplace transform variable s in order to introduce a time dependence into the forcing function. To the I'_{ij} in Eq. (6.17a) we must add the perturbation associated with the deformation of the earth due to loading.

The deformation-induced perturbations may be calculated directly from the definition of the moment of inertia tensor $I_{ij}(t)$ as

$$I_{ij}(t) = \int_v \rho_0(r)[x_l(t)x_l(t)\,\delta_{ij} - x_i(t)x_j(t)]\,d^3x \tag{6.18}$$

where $\rho_0(r)$ is the (in general) radially stratified density field, and $\mathbf{x}$ denotes the position vector of the mass element with density ρ_0 which may be expanded as

$$\mathbf{x} = \bar{\mathbf{x}} + \mathbf{u}(\mathbf{x}, t) \tag{6.19}$$

where $\bar{\mathbf{x}}$ denotes the initial equilibrium position of the mass element, and $\mathbf{u}$ the deformation-related displacement from initial equilibrium. Linearization of Eq. (6.18) in the perturbations from equilibrium gives

$$I'_{ij}(s) = \int_v \rho_0(r)(2\bar{x}_i u_l\,\delta_{ij} - \bar{x}_i u_j - \bar{x}_j u_i)\,dv \tag{6.20}$$

To evaluate Eq. (6.20) for disk load forcing we need the displacement vector $\mathbf{u} = u_r\hat{e}_r + u_\theta$, which from Section 3 may be written as

$$\mathbf{u} = \sum_{l=0}^{\infty}\left[U_l(r, s)P_l(\cos\theta)\hat{e}_r + V_l(r, s)\frac{\partial P_l(\cos\theta)}{\partial\theta}\,\hat{e}_\theta\right] \tag{6.21}$$

Substituting Eq. (6.21) into Eq. (6.20) and evaluating for $I'_{33}(s)$ gives

$$I'_{33}(s) = 2\int_0^a\int_0^{2\pi}\int_0^{\pi}\rho_0 r^3[u_r(\theta, r, s)\sin^2\theta + u_\theta(\theta, r, s)\sin\theta\cos\theta]\sin\theta\,d\theta\,d\phi\,dr \tag{6.22}$$

The functions u_r and u_θ, for a load of arbitrary surface density σ, may be expressed in the form of convolution integrals as

$$u_r(\theta, \phi, r, s) = \int_0^{2\pi}\int_0^{\pi} G^{\mathrm{R}}(\beta, r, s)\sigma(\theta', \phi', s)a^2\sin\theta'\,d\theta'\,d\phi' \tag{6.23a}$$

$$u_\theta(\theta, \phi, r, s) = \int_0^{2\pi}\int_0^{\pi} G^{\mathrm{T}}(\beta, r, s)\sigma(\theta', \phi', s)a^2\sin\theta'\,d\theta'\,d\phi' \tag{6.23b}$$

where G^{R} and G^{T} are Green's functions for radial and tangential displacement which have spherical harmonic decompositions

$$G^{\mathrm{R}}(\theta, r, s) = \sum_{l=0}^{\infty} G_l^{\mathrm{R}}(r, s)P_l(\cos\theta) \tag{6.24a}$$

$$G^{\mathrm{T}}(\theta, r, s) = \sum_{l=0}^{\infty} G_l^{\mathrm{T}}(r, s)\frac{\partial P_l(\cos\theta)}{\partial\theta} \tag{6.24b}$$

Substitution of Eqs. (6.24) and (6.23) in Eq. (6.22) followed by application

of the addition theorem for spherical harmonics yields (for the homogeneous sphere)

$$I'_{33}(s) = -\frac{16\pi\rho_0}{5}\int_0^a\int_0^{2\pi}\int_{-1}^{+1} r^3\left[\frac{G_2^{\mathrm{R}}(r,s)}{3} + G_2^{\mathrm{T}}(r,s)\right] \times P_2(x')a^2\sigma(x',\phi',f)s\,dx'\,d\phi'\,dr \quad (6.25)$$

For the incompressible homogeneous sphere the parameters G_2^{R} and G_2^{T} may be determined from the analysis in Wu and Peltier (1982a) as

$$G_2^{\mathrm{R}} = \frac{1}{\epsilon + \mu\delta}(d_1 r^3 + d_2 r)\left(1 + \frac{\bar{\mu}\gamma}{s+\gamma}\right) \quad (6.26a)$$

$$G_2^{\mathrm{T}} = \frac{1}{\epsilon + \mu\delta}\left(\tfrac{5}{6}d_1 r^3 + d_2 r\right)\left(1 + \frac{\bar{\mu}\gamma}{s+\gamma}\right) \quad (6.26b)$$

where $\epsilon = \delta\pi G\rho_0^2/3$, $\delta = 19/a^2$, $d_1 = 2G\rho_0/a^5$, $d_2 = -16G\rho_0/3a^3$. Substitution of Eq. (6.26) into Eq. (6.25) then gives the analytic result

$$I'_{33}(s) = -\frac{8\pi\rho_0}{15}a^5\frac{d_1a^2 + d_2}{\epsilon + \mu\delta}\frac{1 + \bar{\mu}\gamma}{s+\gamma}L_2(s) \quad (6.27)$$

where $L_2(s)$ is given by Eq. (6.17b). Now we may make use of the fact (Wu and Peltier, 1982a) that the surface load Love number for the homogeneous viscoelastic sphere is

$$k_2(s) = \frac{3}{5}\frac{M_e}{\epsilon + \mu\delta}(d_1a^2 + d_2) \quad (6.28)$$

to write

$$I'_{33}(s) = -\tfrac{2}{3}a^2L_2(s)k_2(s) \quad (6.29a)$$

For the incompressible sphere the trace of the inertia tensor is invariant, so that

$$I'_{11} = I'_{22} = -I'_{33}/2 \quad (6.29b)$$

The total perturbations of inertia due to surface loading are found simply by adding the contribution from the deformation (6.29) to the direct contribution (6.17a) to obtain

$$\begin{aligned} I'_{11}(s) &= \frac{a^2L_2}{3}[1 + k_2(s)]f(s) \\ I'_{22}(s) &= \frac{a^2L_2}{3}[1 + k_2(s)]f(s) \\ I'_{33}(s) &= -\frac{2a^2L_2}{3}[1 + k_2(s)]f(s) \end{aligned} \quad (6.30)$$

where $k_2(s)$ for the homogeneous incompressible model may also be obtained from the general expression for $k_l(s)$ given by Wu and Peltier (1982a)

as

$$k_l(s) = -1 - \frac{\mu(s)(2l^2 + 4l + 3)}{a^2\beta(s)} \tag{6.31}$$

where

$$\beta(s) = a^{-1}[l\rho_0 g_0 + \frac{\mu(s)}{a}(al^2 + 4l + 3)]$$

Expression (6.31) emphasizes the fact that for the homogeneous incompressible model $k_2(s) \rightarrow -1$ as $s \rightarrow 0$. In the next subsection we will see that properties of realistic earth models which force this asymptotic value of $k_2(s)$ to differ from -1 will have important consequences for true polar wandering on the time scale of the Ice Age itself.

6.2.3. Solution of the Euler Equations for the Deglaciation-Induced Polar Motion: The Homogeneous Earth Model. Given the perturbations of inertia due to rotational forcing C_{ij} defined in Eq. (6.12) and the perturbations $I_{ij} = R_{ijkl}I'_{kl}$ from Eq. (6.30) (where R_{ij} is the matrix of the similarity transformation which rotates I'_{ij} into the principal axis system) we have completely specified the J_{ij} in Eq. (6.14) which are required in the Euler equations (6.1). These dynamical equations are clearly highly nonlinear in general and therefore difficult to solve. Sabadini and Peltier (1981) have described a numerical scheme which can be used to solve these nonlinear equations, however, and have employed the exact solution to verify the validity of an approximation scheme proposed by Munk and MacDonald (1960). This approximation scheme is valid as long as the axes of figure and rotation do not wander too far from the reference pole and is based upon linearization of Eq. (6.1) in the small quantities $m_i = \omega_i/\Omega$ (where Ω is the initial angular velocity) and I_{ij}/C where C, as previously, is the principal moment of inertia of the planet. Application of this linearization scheme to Eq. (6.1) leads to the following simple algebraic system in the Laplace transform domain of the imaginary frequency s:

$$\left(\frac{i}{\sigma_r}s + 1\right)m(s) = \psi(s) + \phi(s) \tag{6.32}$$

where $\sigma_r = \Omega(C - A)/A$ is the Chandler wobble frequency for the rigid earth and where $m(s) = m_1(s) + im_2(s)$, in which $m_1(s)$ and $m_2(s)$ are the direction cosines of the rotation axis in the $x_1x_2x_3$ system and ψ and ϕ are the following "excitation functions" due, respectively, to the rotational deformation and the surface load:

$$\psi(s) = \frac{k_2^T(s)}{k_f}m(s) \tag{6.33a}$$

$$\phi_1(s) = \frac{I_{13}(s)}{C - A} + \frac{[sI_{23}(s) - I_{23}(t = 0)]}{\Omega(C - A)} \tag{6.33b}$$

$$\phi_2(s) = \frac{I_{23}(s)}{C - A} + \frac{[sI_{13}(s) - I_{13}(t = 0)]}{\Omega(C - A)} \tag{6.33c}$$

where $\phi(s) = \phi_1(s) + i\phi_2(s)$ and where $k_f = 0.934$ is the so-called fluid Love number associated with the centrifugal deformation (Lambeck, 1980). In this scheme the solution to Eq. (6.32) describes the polar motion, whereas the l.o.d. variations are determined by the following decoupled equation for $m_3(s)$:

$$m_3(s) = \phi_3(s) = -\frac{I_{33}(s)}{C} \tag{6.34}$$

If in Eq. (6.10) we replace the factor 3/2 by the factor $k_f = 0.934$ for the real earth, then

$$k_2^T(s) = \frac{k_f}{1 + \bar{\mu}}\left(1 + \frac{\bar{\mu}\gamma}{s + \gamma}\right) \tag{6.35}$$

and the solution of Eq. (6.32) may be well approximated (Munk and MacDonald, 1960) as

$$m(s) = -\frac{i\sigma_r}{\gamma - i\sigma_0}\left(\frac{\gamma}{s} - \frac{i\sigma_0}{s + \gamma - i\sigma_0}\right)\phi(s) \tag{6.36}$$

where $\sigma_0 = \sigma_r\bar{\mu}/(1 + \bar{\mu})$ is the Chandler frequency of the homogeneous elastic earth. Inspection of Eq. (6.36) shows that the solution to the polar motion problem *apparently* consists of the superposition of two normal modes with imaginary frequencies $s = 0$ and $s = i\sigma_0 - \gamma$ determined by the locations of the poles of $m(s)$ in the complex s plane. This led Sabadini and Peltier (1981) to approximate the solution of Eq. (6.36) by neglecting the second term in parentheses on the right-hand side on the basis of the argument that the high-frequency Chandler wobble described by this term should not be efficiently excited by the slowly varying ice sheet loads which contribute to the excitation spectrum $\phi(s)$. This argument turns out to be incorrect, as has recently been pointed by Peltier and Wu (1982), though Sabadini *et al.* (1982a,b) have continued to employ it. When the second term in parentheses is neglected, the time domain solutions are radically different from those which include its influence, even when the final solution is subjected to a running average over the period $2\pi/\sigma_0$ to remove explicit appearance of the Chandler wobble. The reason is clearly (in retrospect!) that this term makes an important nonzero contribution to the mean motion of the pole. The results obtained in the papers of Sabadini *et al.* (1982a,b) are therefore completely erroneous.

To understand the source of this error from an algebraic point of view,

we may substitute Eqs. (6.30) and (6.33) directly into Eq. (6.36), assuming that the rotational forcing is produced by a single circular ice cap whose center lies an angular distance θ (say) from the CIO. If the coordinate direction "1" is assumed to point toward the glaciation center then the explicit form of Eq. (6.36) is

$$m(s) = \frac{-i\sigma_0}{\gamma - i\sigma_0}\left(\frac{\gamma}{s} - \frac{i\sigma_0}{s + \gamma - i\sigma_0}\right)[1 + k_2(s)](\phi_1^0 + i\phi_2^0)f(s) \tag{6.37}$$

where

$$\phi_1^0 = \frac{a^2 \sin\theta\cos\theta}{(C - A)} L_2^1 \qquad \phi_2^0 = -\frac{a^2 \sin\theta\cos\theta}{\Omega(C - A)} L_2^1$$

where $L_2^1 = L_2/f(s)$ from Eq. (6.17b) and the surface load Love number $k_2(s)$ is taken to be given by

$$k_2(s) = \frac{-(1 - l_s)}{(1 + \bar{\mu})}\left[1 + \frac{\bar{\mu}\gamma}{s + \gamma}\right] \tag{6.38}$$

which differs from the exact expression for the homogeneous model (6.28) in the appearance of the small positive parameter l_s, which is the so-called isostatic factor discussed in Munk and MacDonald (1960). Its introduction in Eq. (6.38) enables the homogeneous earth model to mimic realistic models of the earth in the sense that

$$\lim_{s \to 0} [1 + k_2(s)] = l_s \neq 0 \tag{6.39}$$

Realistic earth models have $l_s \neq 0$ because of the presence of the surface lithosphere and of internal density stratification, but the former effect is most important. Although we will not give the algebraic details of the Laplace inversion of Eq. (6.37) here, it can be accomplished analytically. The exact solution for the mean motion of the pole (i.e., Chandler wobble filtered) for an arbitrary time dependence of the ice sheet loading and unloading $f(t)$, is found to be such that

$$\dot{\bar{m}}_1(t) = \frac{\Omega}{A\sigma_0}[\gamma(1 + \bar{\mu})P_1 f(t) + (P_1 + P_2)\dot{f}(t)] \tag{6.40}$$

where $\dot{\bar{m}}_1(t)$ is the speed of polar wander in the direction of the centroid of the ice sheet, positive being toward and negative away from this direction. The parameters P_1 and P_2 which appear in Eq. (6.40) are defined as

$$P_1 = \frac{A\sigma_0}{\bar{\mu}} \frac{l_s}{\bar{\mu}} \frac{a^2 \sin\theta\cos\theta\, L_2^1}{(C - A)} \tag{6.41}$$

$$P_2 = \frac{\bar{\mu}}{l_s} P_1 \tag{6.42}$$

It is useful to consider the solutions (6.40) for the following two different choices of the time history $f(t)$.

Case A

In this example we take

$$\begin{aligned} f(t) &= 0, && t \le a \\ &= \frac{(t-a)}{(b-a)}, && a \le t \le b \\ &= 1, && t \ge b \end{aligned} \tag{6.43}$$

From Eq. (6.40) the solution in this case is

$$\begin{aligned} \dot{m}_1(t) &= 0, && t < a \\ &= \frac{\Omega}{A\sigma_0}\left[\frac{P_1 + P_2}{b-a} + \gamma(1+\bar{\mu})P_1\frac{t-a}{b-a}\right], && a \le t \le b \\ &= \frac{\Omega}{A\sigma_0}\gamma(1+\bar{\mu})P_1, && t > b \end{aligned} \tag{6.44}$$

This corresponds to the situation in which a disk load is removed from the surface over the time interval $(b-a)$ at a uniform rate. The assumption is that the load was initially in isostatic equilibrium. It is clear from Eq. (6.44) that $\dot{m}_1$ is nonzero for $t > b$ only because $l_s \neq 0$ [see Eq. (6.41)]. This model is essentially identical to that of Nakiboglu and Lambeck (1980), although these authors did not employ our simple disk load approximation to the melting history. Both $f(t)$ and $\dot{m}(t)$ for this model are shown in Fig. 37a. Since $\gamma = (\mu/\nu)/(1+\bar{\mu})$ depends upon the viscosity ν and $\dot{m}_1$ is an observable ($\dot{m}_1 \approx 1°/10^6$ yr from Fig. 36), we may invert Eq. (6.44) for $t > b$ to obtain ν. This gives $\nu \approx 6 \times 10^{20}$ Pa sec with $l_s \approx 0.006$ (Munk and MacDonald, 1960), essentially identical to the value inferred by Nakiboglu and Lambeck (1980) on the basis of a much more complicated model of the deglaciation history. In fact Nakiboglu and Lambeck (1980) employed the ICE-1 model of Peltier and Andrews (1976) in their calculations. This serves to demonstrate the adequacy of the disk load disintegration model for the polar wander analysis and reveals the basic physics clearly.

Case B

Since we know from the oxygen isotope stratigraphy in deep-sea sedimentary cores that the main ice sheets of the Pleistocene have periodically appeared and disappeared with a time scale of about 10^5 yr, it is quite clear that the simple unloading model of case A is something of an oversimplification. In order to determine the way in which a load cycle modifies the

solution (6.44) we will consider the history

$$\begin{aligned} f(t) &= \frac{(t-a)}{(b-a)}, \qquad a \le t \le b \\ &= \frac{(t-c)}{(b-c)}, \qquad b \le t \le c \\ &= 0, \qquad \text{otherwise} \end{aligned} \tag{6.45}$$

which consists of a single loading epoch for $a \le t \le b$ and a single unloading epoch for $b \le t \le c$. Substitution of Eq. (6.45) into Eq. (6.40) gives the explicit solution

$$\begin{aligned} \dot{\bar{m}}(t) &= \frac{\Omega}{A\sigma_0}\frac{(P_1+P_2)}{(b-a)} + \gamma(1+\bar{\mu})P_1\frac{(t-a)}{(b-a)}, \qquad a \le t \le b \\ &= \frac{-\Omega}{A\sigma_0}\frac{(P_1+P_2)}{(c-a)} + \gamma(1+\bar{\mu})P_1\frac{(t-c)}{(c-b)}, \qquad b \le t \le c \\ &= 0, \qquad \text{otherwise} \end{aligned} \tag{6.46}$$

which is plotted along with $f(t)$ itself in Fig. 37b. It is quite clear from the form of Eq. (6.40) that no matter how many cycles of the form (6.45) may have preceded the single cycle we have analyzed, the solution within each cycle is completely oblivious of the others since the system has no memory. Therefore, if a large number of cycles of this form have occurred prior to the time $t = c$ and if the ice sheet is not actively accumulating for $t > c$, then Eq. (6.46) show that $\dot{\bar{m}}(t) \equiv 0$. Since we are presently living in precisely such a time, we see that the homogeneous viscoelastic model of the planet which we have been considering up to now in this section is *completely incapable* of delivering accord with the observed secular drift of the pole which is revealed by the ILS data shown in Fig. 36. This is completely contrary to the result obtained in Sabadini and Peltier (1981), but their results are invalid because of the neglect of the second term in parentheses on the right-hand side of Eq. (6.36).

The above-discussed results for cases A and B show that the homogeneous viscoelastic model of the earth is completely incapable of delivering accord with the observations. The analysis of Nakiboglu and Lambeck is incorrect because the actual history of loading is cyclic and the case B results show that the predicted speed of polar wander for the present day in such a case is identically zero. This clearly raises the embarrassing question of whether our hypothesis that the secular drift seen in the ILS pole path is in fact due to Pleistocene deglaciation. In the next subsection we will show that this hypothesis is correct but the viscoelastic stratification of the real earth must be taken into account since it contributes in a crucial way to the forced polar motion which is observed in the astronomical data.

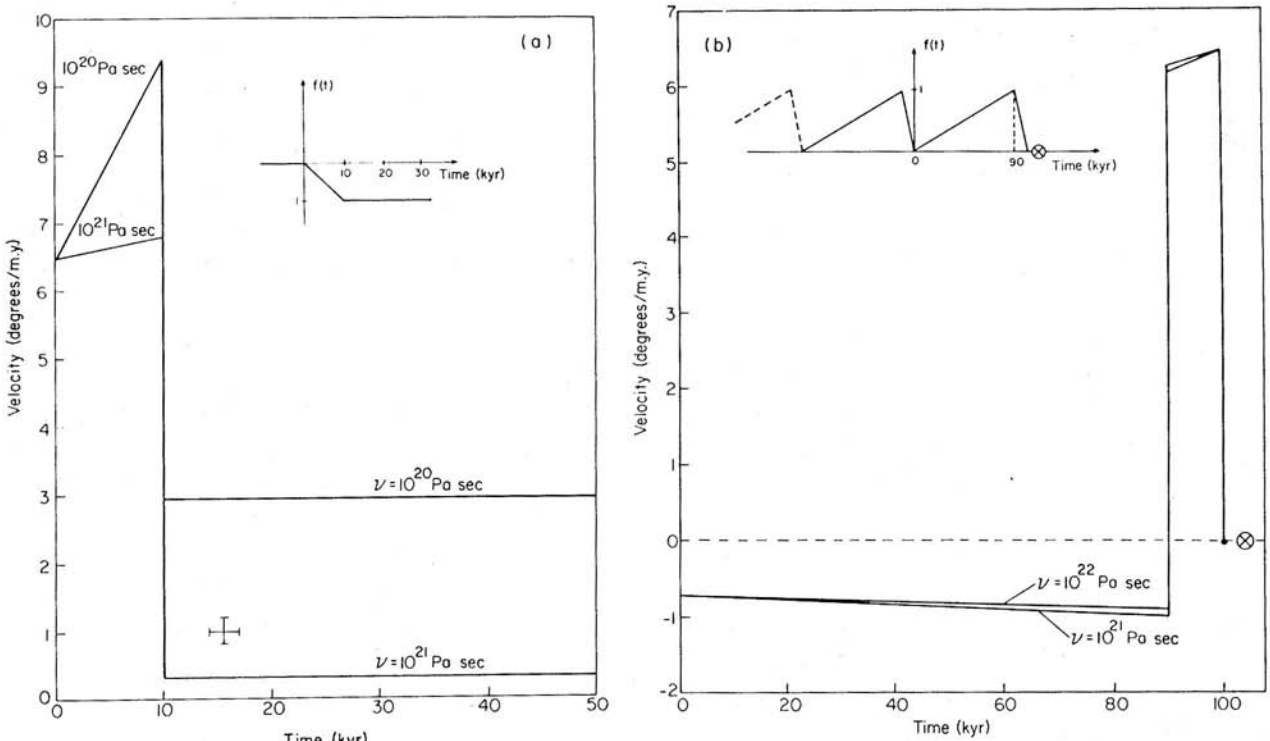

FIG. 37. (a) Predicted polar wander speed for the Nakiboglu and Lambeck (1980) model of deglaciation. The observed $1°/10^6$ yr secular drift in the ILS pole path is shown by the cross. (b) Predicted polar wander speed for a sawtooth load cycle. Both calculations are for the homogeneous earth model.

6.2.4. Solution of the Euler Equations for the Deglaciation-Induced Polar Motion: Stratified Viscoelastic Models. As can be shown in a rather straightforward fashion, all of the preceding analysis up to and including Eq. (6.34) will continue to hold for layered viscoelastic models so long as we replace the load and tidal Love numbers $k_2(s)$ and $k_2^T(s)$ by their equivalents for the layered model under consideration. Analysis in preceding sections of this article then shows that the tidal Love number may be written in general in the form

$$k_2^T(s) = k_2^{TE} + \sum_{j=1}^{M} \frac{t_j}{s + s_j} \tag{6.47}$$

With $k_f = k_2^T(0) = k_2^E + \Sigma_{j=1}^M (t_j/s_j)$ required for insertion into Eq. (6.32) from Eq. (6.33a), we may rewrite Eq. (6.47) as

$$k^T(s) = k_f - s \sum_{j=1}^{M} \frac{t_j/s_j}{s + s_j} \tag{6.48}$$

We may similarly manipulate the general expression for the surface load Love number

$$k_2(s) = k_2^E + \sum_{j=1}^{M} \frac{r_j}{s + s_j} \tag{6.49}$$

by defining

$$1 + k_2(0) = l_s \tag{6.50}$$

for the layered model, to write

$$1 + k_2(s) = l_s - \sum_j \frac{r_j}{s_j} \frac{s}{s + s_j} \tag{6.51}$$

Using Eqs. (6.48) and (6.51) in the Euler equation (6.32) along with the definition of ψ in Eq. (6.33a) and the ϕ appropriate for a circular disk load as in the last subsection, the equation which replaces Eq. (6.37) for this general case is

$$m(s) = \frac{-i\sigma_r[1 - i(s/\Omega)][1 + k_2(s)]\phi_1^0 f(s)}{s[1 - (i\sigma_r/k_f)\ \Sigma_{j=1}^M\ (t_j/s_j)/(s + s_j)]} \tag{6.52}$$

Since $s_j \ll \sigma_r$, $s \ll \sigma_r$, $(t_j/s_j)/k_f \lesssim O(1)$, and $[\sigma_r/(s + s_j)][(t_j/s_j)/k_f] \gg 1$, Eq. (6.52) reduces directly to

$$\bar{m}(s) = \frac{k_f(1 - (is/\Omega)][1 + k_2(s)]\phi_1^0 f(s)}{s\ \Sigma_j\ (t_j/s_j)/(s + s_j)} \tag{6.53}$$

Since

$$\phi_1^0 = \frac{a^2 \sin\theta \cos\theta\ L_2^1}{C - A} = \frac{\Omega}{A\sigma_r} a^2 \sin\theta \cos\theta\ L_2^1$$

and

$$\frac{\sigma_0}{\sigma_r} = \frac{k_f - k_2^{TE}}{k_f} = \frac{\sum (t_j/s_j)}{k_f}$$

we may define

$$\beta_j = \frac{t_j/s_j}{\sum (t_j/s_j)}$$

to reduce Eq. (6.53) to the form

$$\bar{m}(s) = \frac{\Omega}{A\sigma_0} \frac{a^2 \sin\theta \cos\theta \, L_2^1}{\Sigma_j \beta_j/(s + s_j)} \left(\frac{1}{s} - \frac{i}{\Omega}\right)[1 + k_2(s)]f(s) \tag{6.54}$$

Defining $\alpha = a^2 \sin\theta \cos\theta \, L_2^1 l_s$, the real part of Eq. (6.54) is

$$\bar{m}_1(s) = \frac{\Omega}{A\sigma_0} \frac{\alpha}{\Sigma_j \beta_j/(s + s_j)} \frac{[1 + k_2(s)]}{l_s s} f(s) \tag{6.55}$$

Note that for the homogeneous earth $\alpha = (1 + \bar{\mu})P_1$ and $s_j = \gamma$ with $j = 1$ (i.e., 1 mode). In this case Eq. (6.55) reduces exactly to the $\bar{m}_1(s)$ obtained from Eq. (6.37) by approximating $-i\sigma_r/(\gamma - i\sigma_0) \approx 1$, and similarly replacing the second term in parentheses on the right-hand side of Eq. (6.37) as $-i\sigma_0/(s + \gamma - i\sigma_0) \approx 1$ (not 0, as assumed in Sabadini and Peltier, 1981). It is this $\bar{m}_1(s)$ which gives the $\bar{m}_1(t)$ implied by Eq. (6.40). Now the Laplace transform domain solution (6.55) may be inverted analytically, although the algebra is extraordinarily tedious and will not be given here. The time domain solution requires knowledge of the roots $-\lambda_i$ of the degree $M - 1$ polynomial

$$\begin{aligned} P_{M-1}(s) &= \sum_{j=1}^{M} [\beta_j \prod_{i \neq j} (s + s_i)] \\ &= \prod_{i=1}^{M-1} (s + \lambda_i) \end{aligned} \tag{6.56}$$

which may be determined numerically with any conventional root-finding algorithm since the s_i are known. The *exact* inverse of Eq. (6.55) yields a function $\bar{m}_1(t)$ whose time derivative is

$$\begin{aligned} \dot{\bar{m}}_1(t) = \frac{\Omega\alpha}{A\sigma_0} \Bigg\{ \Bigg[1 - \sum_{j=1}^{M} \frac{(r_j/s_j)}{l_s} \Bigg] \dot{f}(t) - \frac{q(0) f(t)}{\prod_i \lambda_i} \\ + \sum_{i=1}^{M-1} \left[\frac{q(-\lambda_i)}{\lambda_i \prod_{j \neq i} (\lambda_j - \lambda_i)} + \sum_{j=1}^{M} \frac{(r_j/s_j)}{l_s} \frac{R_j(-\lambda_i)}{\prod_{k \neq i} (\lambda_k - \lambda_i)} \right] \frac{d}{dt} (f * e^{-\lambda_i t}) \Bigg\} \end{aligned} \tag{6.57}$$

in which $q(s) = s(s + \lambda_i)\cdots(s + \lambda_{M-1}) - (s + s_1)\cdots(s + s_M)$ and

$$R_j(s) = \prod_{i=1}^{M-1} (s + \lambda_i) - \prod_{i \neq j} (s + s_i)$$

Clearly the general solution (6.57) differs in an extremely important way from the equivalent solution for the homogeneous model expressed in Eq. (6.40). The important difference is the presence of the third term on the right-hand side, which consists of a sum of terms which are each proportional to the time rate of change of the convolution of $f(t)$ with a decaying exponential. The presence of this term indicates that stratified viscoelastic models will exhibit an instantaneous response which includes a contribution from the forcing applied at all past times. Each of the $M - 1$ terms in the sum therefore represents a memory of the past state of the system, and it is this history-dependent term, which is clearly absent from the homogeneous solution (6.40), which will allow the layered viscoelastic model to fit the observed polar wander in the ILS pole path even when the load is cyclic. The correct solution [Eq. (6.57)] for the layered viscoelastic model is completely different from that found in Sabadini *et al.* (1982a,b). Their solution is obtained by neglecting s with respect to s_j in the denominator of Eq. (6.54), which amounts to assuming that the earth behaves as a fluid insofar as the rotational response is concerned, which is itself consistent with the assumption in Sabadini and Peltier (1981) and the neglect of the second term in parentheses on the right-hand side of Eq. (6.36). That the assumption is physically incorrect follows simply from the recognition that both the tidal and surface load Love numbers, k_2^T and k_2 respectively, have precisely the same spectrum of decay times as stated in Eqs. (6.47) and (6.44). The set s_j ($j = 1, M$) for k_2^T is the same as the set s_j for k_2. Since k_2^T and k_2 determine the time dependence of the response to tidal forcing and surface loading, respectively, it is quite clear that there is a basic inconsistency in assuming the fluid limit for one and not for the other. The correct solution to the polar wander equations for models with arbitrary viscoelastic layering is that given by Eq. (6.57), which is valid for arbitrary $f(t)$.

As in Section 5, we determine $f(t)$ by invoking the oxygen isotope data shown previously in Fig. 32a: however, we will employ the slightly more complicated waveform shown in Fig. 38a. which differs from that shown in Fig. 32b in that the deglaciation phase of the load cycle is assumed to take place over a finite rather than an infinitesimal time interval. Although this does not produce any marked effect on the results we have included it as a better approximation to the actual $^{18}O/^{16}O$ data. Each of the cycles of this wave shape has a mathematical form described by Eq. (6.45). To determine the solution for this excitation we simply substitute $f(t)$ into Eq. (6.57). If there have been N previous load cycles of the form (6.45) then

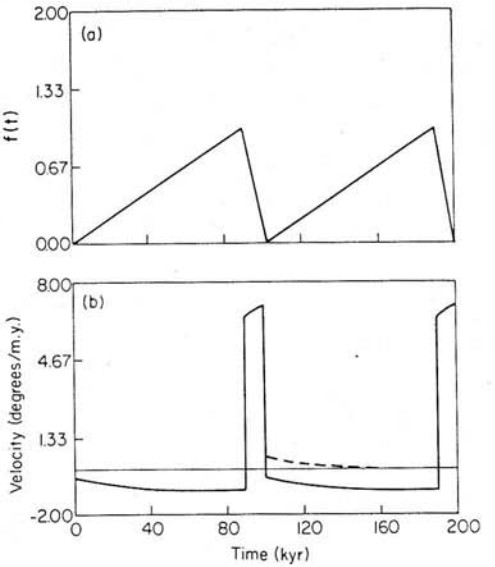

FIG. 38. (a) The sawtooth approximation to the load history which is employed in all of the calculations in this section. (b) The prediction of polar wander speed as a function of time during the cycle for viscoelastic model I. The dashed line is the speed which is predicted on the basis of the assumption that no glaciation occurs subsequent to the last deglaciation event.

each of the convolution integrals in Eq. (6.57), during and after the current load cycle, is given by expressions of the following form:

(i) During the glaciation phase

$$\frac{d}{dt}(f * e^{-\gamma t}) = -\beta e^{-\gamma t} + \frac{1 - e^{-\gamma(t-\Delta t)}}{\gamma\, \Delta T} \tag{6.58a}$$

(ii) During the deglaciation phase

$$\frac{d}{dt}(f * e^{-\gamma t}) = -\beta e^{-\gamma t} + e^{-\gamma(t-\Delta t)}\left[\frac{e^{\gamma \Delta T} - e^{\gamma(t-\Delta T)}}{\gamma\, \Delta t} - \frac{1 - e^{\gamma \Delta T}}{\gamma\, \Delta T}\right] \tag{6.58b}$$

(iii) For $f \equiv 0$ following the latest deglaciation event (i.e., today)

$$\frac{d}{dt}(f * e^{-\gamma t}) = -\beta e^{-\gamma t} \tag{6.58c}$$

The parameter β has the following definition:

$$\beta = \left[\frac{e^{-\gamma \Delta T} - 1}{\gamma\, \Delta T} + \frac{e^{\gamma \Delta T} - 1}{\gamma\, \Delta t}\right]\left[\frac{1 - e^{-\gamma N(\Delta T - \Delta t)}}{1 - e^{-\gamma(\Delta T - \Delta t)}}\right] \tag{6.58d}$$

while Δt and ΔT are, respectively, the duration of the deglaciation and glaciation phases of the load cycle. The oxygen isotope and other geophysical data suggest $\Delta t \approx 10^4$ yr and $\Delta T \approx 9 \times 10^4$ yr. These are the numerical values of the parameters which we have employed in constructing Fig. 38 and in all of the calculations to be described here. The complete solution for the polar motion of a stratified viscoelastic model forced by N cycles of glaciation and deglaciation is obtained simply by substituting terms of the form (6.58) into Eq. (6.57), where γ is replaced by the appropriate λ_i for each term. Since the 10^5-yr cycle has dominated the climate record only through the Pleistocene period, which began about 2×10^6 yr B.P., and since it is essentially absent from the record prior to about 3×10^6 yr B.P., we have assumed the conservative $N = 30$ in our calculations.

For an earth model with 1066B elastic structure, a constant mantle viscosity of 10^{21} Pa sec, an inviscid core, and a lithosphere of thickness 120 km, the variation of polar wander speed $\dot{\tilde{m}}_1$ is shown in Fig. 38b as a function of time through the load cycle. At a time like the present, of hiatus in the load cycle, the solution follows the dashed rather than the solid curve. The polar wander speed for the inhomogeneous model no longer drops to zero immediately when the load is removed. This is due to the presence of the history terms in Eq. (6.57) which are entirely a consequence of the viscoelastic layering of the earth model which, as we have seen previously, is responsible for supporting a multiplicity of normal modes of viscous gravitational relaxation for each spherical harmonic degree in the deformation. The second point to note from Fig. 38 is that the predicted magnitude of the present-day polar wander velocity is of the same order as that observed astronomically. Furthermore, the direction of the predicted mean motion is toward the centroid of the disk load (i.e., positive), which is also in accord with the observed apparent motion's being in the direction of Hudson Bay. It is clear that we may expect to constrain the parameters of the stratified model by fitting it to the rotation data.

On the basis of the above discussion it should be clear that the polar motion data will be explicable in terms of glacial forcing only because the real earth is viscoelastically layered. As shown in Section 5, the layering was also required in order to understand the free-air gravity anomalies observed over present-day centers of postglacial rebound. In that application we showed that the most important features of the layering were the density discontinuities across the phase boundaries located in the mantle transition zone at 420 km and 670 km depth, and that the observed free-air gravity anomaly provided a high-quality constraint on the viscosity of the lower mantle. It might be naively expected that the rotation data would be sensitive only to the mean viscosity of the mantle, since they depend only upon the

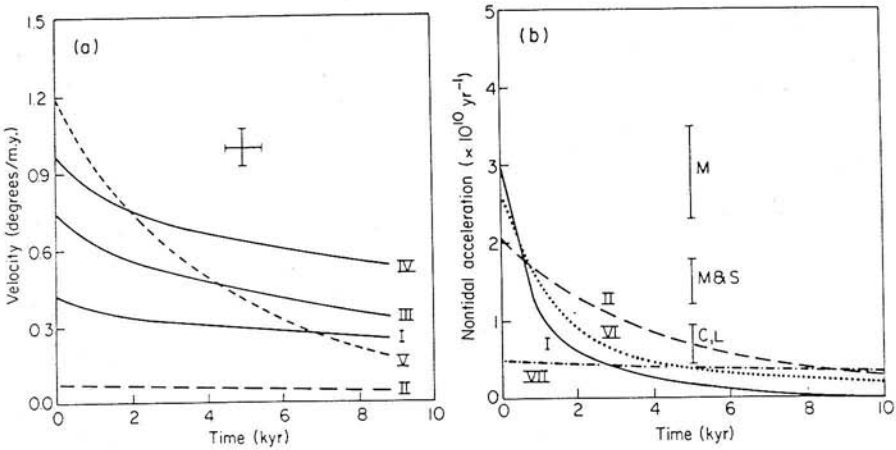

FIG. 39. (a) Prediction of polar wander speed as a function of time for the five realistic viscoelastic models (I–V) discussed in the text. The observed speed of polar wander in the ILS data ($1°/10^6$ yr) is shown on the figure. (b) Predictions of the nontidal acceleration of rotation for the realistic viscoelastic models I–VII. Various of the observational estimates of this parameter are shown on the figure.

degree-two harmonic of the deformation, and that the long-wavelength undulation should sample the mantle throughout its volume. This expectation turns out to be only partly borne out by calculation. Of equal importance to the results, as we shall see, is the magnitude of the isostatic factor l_s which is defined for the layered model in Eq. (6.50). Since the magnitude of the isostatic factor is controlled principally by the thickness of the surface lithosphere, the predicted polar motion is very sensitive to this feature of the viscoelastic layering. This may perhaps have been anticipated on the basis of the important role which l_s was shown to play for the homogeneous model analyzed in the last subsection.

Figure 39a illustrates a sample of the results obtained with the complete theory for several different stratified viscoelastic models. This plate shows the speed of polar wander as a function of time since the end of the last deglaciation phase for five different layered models (I–V), whose properties are listed in Table VI. Models I and II both have 120-km-thick lithospheres and 1066B elastic structures and differ from one another only in their lower mantle viscosities, which are 10^{21} Pa sec and 10^{22} Pa sec for models I and II, respectively. Since the observed present-day speed of polar wander is $1°/10^6$ yr it is quite clear that the model with high lower mantle viscosity is more strongly rejected by the rotation data than is the uniform viscosity model I. However, it is equally true that the model preferred by the sea level

and gravity data, essentially model I, does *not* provide an acceptable fit to the rotation data. It predicts a present-day speed of polar wander of only about $0.3°/10^6$ yr, which is only a third of the observed speed. Clearly, reducing the viscosity of the lower mantle somewhat further would further increase the predicted speed, but we would then be unable to satisfy the gravity anomalies observed over Fennoscandia and Laurentia as shown in Section 5 of this paper. Our first recourse must then be to increase l_s by increasing the thickness of the lithosphere while maintaining the viscosity of the mantle equal to that of model I. Models III and IV have lithospheric thicknesses of 195 km and 245 km, respectively. Inspection of Fig. 39a shows that the model with the thickest lithosphere comes closest to fitting the astronomical observation of present-day polar wander speed (extrapolation suggests that a best fit occurs with $L \approx 300$ km). However, this thickness is considerably greater than that suggested by some other lines of evidence, and it is important to inquire whether there may be other geophysical data which could be invoked in support of this number.

There are in fact several lines of evidence that suggest a value of L, at least for continental lithosphere, which is as high as this. The most important of these data, insofar as we are concerned here, consists of a subset of the RSL histories which were discussed in Section 4. There it was shown that RSL data from sites along the eastern seaboard of the United States, to the south of the location of the ice margin at 18 kyr B.P. (which was near Boston), all differ systematically from the predictions made on the basis of viscoelastic model I. The theoretical model predicts much more submergence at these sites than is actually observed. It should be fairly obvious intuitively that it is in just this peripheral region that the flexure of the lithosphere is most extreme and therefore in just this region that the theoretical predictions will be most sensitive to lithospheric thickness. When

TABLE VI. PROPERTIES OF THE LAYERED MODELS EMPLOYED IN THE ROTATION CALCULATIONS

Model	Lithospheric thickness L (km)	Isostatic factor (l_s)	Upper mantle viscosity (Pa sec)	Lower mantle viscosity (Pa sec)
I	120	0.0091	10^{21}	10^{21}
II	120	0.0091	10^{21}	10^{22}
III	195	0.0156	10^{21}	10^{21}
IV	245	0.0209	10^{21}	10^{21}
V	120	0.0091	2×10^{20}	2×10^{20}
VI	120	0.0091	10^{21}	3×10^{21}
VII	120	0.0091	10^{21}	10^{23}

RSL predictions are made for models with increasing values of L it is found that the variance between observation and theory is reduced to zero at edge sites with a value of L very near that suggested by the preceding analysis of the polar motion data. The details of this analysis will be presented elsewhere. It should also be clear that this increase of the value of L from that in model I will not change any of the results for RSL and free-air gravity at sites inside the ice margin. This expectation is also borne out by direct calculation. We will return to discuss the meaning of this large value for the lithospheric thickness in Section 6.3.

On the basis of the above analysis we may take it as established that the polar wander observed in the ILS pole path is a memory of the planet of the glaciation cycle to which the continents of the Northern Hemisphere have been subjected for at least the past 2×10^6 yr. In fact, there is yet another astronomical observation which may be invoked to check the result obtained from the analysis of the polar motion. This is the so-called nontidal component of the acceleration of rotation. This observation, discussed in Munk and MacDonald (1960) and more recently in Lambeck (1980), may be obtained through an analysis of the historical variations of l.o.d. by subtracting from the data the variation expected on the basis of the assumption that the lunar tidal torque has not changed significantly. When one does this one obtains a residual which yields an acceleration of rotation corresponding to the values of $\dot{\omega}_3/\Omega$ listed in Table V which have been obtained by various authors using different methods of analysis. The theoretical prediction of $\dot{m}_3$ follows immediately through Laplace inversion of Eq. (6.34) with the appropriate $I_{33}(s)$ inserted on the right-hand side. Now $I_{33}(s)$ for the disk load approximation of the melting history is given by

$$I_{33}(s) = (a^2/3)(1 - 3\cos^2\theta)(1 + k_2)L_2^1 f(s) \tag{6.59}$$

with

$$1 + k_2(s) = l_s - \sum_j \frac{r_j}{s_j} \frac{s}{s + s_j}$$

as in Eq. (6.51). The Laplace inverse of $I_{33}(s)$ is clearly

$$I_{33}(t) = \frac{a^2}{3}(1 - 3\cos^2\theta)L_2^1\left[\left(l_s - \sum_j \frac{r_j}{s_j}\right)f(t) + \sum_j r_j f(t) * e^{-s_j t}\right] \tag{6.60}$$

and from Eq. (6.34) we have

$$\dot{m}_3 = -I_{33}(t)/C \tag{6.61}$$

Figure 39b compares the prediction (6.61) to the observations for the same set of stratified viscoelastic models as were discussed in the context of our previous considerations of the polar motion observations. We have

also used the same cyclic $f(t)$ used to construct Fig. 39a and evaluated the contribution from the history integrals $f(t) * e^{-s_j t}$ on the basis of the assumption that there have been 30 previous cycles in the load history, each of duration 10^5 yr. From the structure of the solution (6.60, 6.61) we see that it will not be sensitive to the isostatic factor l_s, since this appears only in the first term in the square brackets on the right-hand side of Eq. (6.60) where it multiplies $f(t)$. Since $f(t) \equiv 0$ now, l_s will not contribute to the observed nontidal acceleration of rotation. This explains why models I, III, and IV in Figure 39b predict essentially the same present-day nontidal acceleration of rotation (only the curve for model I is shown explicitly). These models essentially differ only in the thickness of their lithospheres and therefore only in their l_s values. A more detailed analysis of the solution space for a range of models which all have a lithospheric thickness of 120 km and differ from one another only in the value of the mantle viscosity beneath 670 km depth was presented in Wu and Peltier (in preparation). This shows that there are in fact two values of the deep mantle viscosity which are equally acceptable to this datum, one near 10^{21} Pa sec, which is that which accords with the polar wander requirements, and one much higher near 3×10^{22} Pa sec, which is completely rejected by all of the previously discussed information (i.e., RSLs, free-air gravity anomalies, and polar wander speed). The double-root structure of the nontidal l.o.d. solution was first pointed out in Sabadini and Peltier (1981), whose analysis of this datum does not suffer from the error made in connection with the polar wander analysis. The fact that model II is preferred over model I in Fig. 39b is a consequence of the fact that both the Antarctic and Fennoscandian ice sheets have been omitted in our analysis. When these ice masses are included, the uniform viscosity model is again preferred by the observations.

One additional global observable which we can predict reasonably accurately on the basis of the disk load model of the glaciation history which we have employed for all of our previous analyses of rotational dynamics concerns the time dependence of the second-degree component in the spherical harmonic expansion of the earth's gravitational potential field. This is conventionally denoted by $\dot{J}_2$. The Green's function for the perturbation of gravitational potential for a mass point is given in Eq. (3.40). This determines the potential with respect to a point on the free surface of the model since it includes the contribution from the Love number for radial displacement h_l. Relative to the earth's center of mass the potential perturbation due to the point-mass load is

$$J(\theta, t) = \frac{ag}{M_e} \sum_{l=0}^{\infty} [1 + k_l(t)] P_l(\cos\theta) \tag{6.62}$$

which we will assume is to be evaluated on the earth's surface. Convolution of this Green's function over the circular disk load produces a perturbation of potential which has a second-degree harmonic amplitude of

$$\Delta J_2(s) = \sqrt{\frac{4\pi}{5}} \frac{ag}{M_e} M \cos\alpha \, P_2(\cos\Theta)[1 + k_2(s)]f(s) \tag{6.63}$$

This may be simply inverted to the time domain to give ΔJ_2, whose time derivative is

$$\Delta \dot{J}_2(t) = ag \sqrt{\frac{4\pi}{5}} \frac{M \cos\alpha \, P_2(\cos\Theta)}{M_e} \times \left\{ \left[l_s - \sum_j \frac{r_j}{s_j} \right] \dot{f}(t) - \sum_j r_j \frac{d}{dt} (f * e^{-s_j t}) \right\} \tag{6.64}$$

Following the last cycle of loading, $\dot{f}(t) \equiv 0$ and the time derivative of the convolution integral in Eq. (6.64) is given by Eq. (6.58c), so that

$$\Delta \dot{J}_2(t) = -ag \sqrt{\frac{4\pi}{5}} \frac{M \cos\alpha \, P_2(\cos\Theta)}{M_e} \sum_j r_j \beta_j e^{-s_j(t+\Delta t)} \tag{6.65}$$

Evaluation of Eq. (6.65) for the realistic stratified viscoelastic models discussed previously in this subsection gives the results listed in Table VII. Although $\dot{J}_2$ has not yet been extracted from the satellite orbital data, the increasingly high accuracy with which J_2 itself is being determined promises that this will soon be possible. This observation will then provide us with another means of constraining the viscoelastic layering of the earth and serve as a cross-check on inferences made on the basis of the previously discussed polar wander and l.o.d. observations.

6.3. *Polar Motion and l.o.d. Constraints on the Earth's Viscoelastic Stratification*

Our previously discussed analyses of RSL and free-air gravity data showed that these data implied a viscosity profile for the planet such that ν was essentially infinite in a relatively thin surface "lithosphere" and that this was underlain by an upper mantle in which the viscosity was very near 10^{21} Pa sec. Across the phase transition at 670 km depth the combined RSL and free-air gravity data required an increase of viscosity but by no more than a factor of perhaps two. The viscosity of the lower mantle according to these data is then about 2×10^{21} Pa sec, or very nearly the same as that of the upper mantle.

TABLE VII. PREDICTIONS OF PRESENT-DAY $\dot{J}_2$

Model	$\dot{J}_2$ (m^2 sec^{-3})
I	0.3032×10^{-10}
II	0.1096×10^{-9}
IV	0.1777×10^{-10}
V	0.4141×10^{-12}
VI	0.6160×10^{-10}
VII	0.6035×10^{-10}

The polar motion and l.o.d. analyses discussed in the last subsection have added somewhat to the further refinement of this picture. In the first instance they are also quite sensitive to the viscosity of the lower mantle and also insist upon a value near that (i.e., low) preferred by the RSL and free-air gravity data. This is useful corroboration. The observation of polar wander speed, in addition to this sensitivity to the deep structure, was also shown to be particularly sensitive to the thickness of the lithosphere. In order to fit the data with a fixed mantle viscosity of 10^{21} Pa sec we were obliged to employ a lithospheric thickness in excess of 245 km, which is considerably in excess of that which most would consider reasonable as a measure of the average lithospheric thickness for the entire planet. Although there is very good evidence from RSL data in the region peripheral to the Laurentide ice sheet that the thickness of the continental lithosphere is in fact on this order, it is a number which is quite impossible to accept for oceanic lithosphere which is well constrained seismically and through studies of the flexure and gravity anomalies associated with seamounts and guyots. These data constrain the thickness of the oceanic lithosphere to be less than or equal to about 120 km. The explanation of this apparent inconsistency may be found in the way in which the lateral heterogeneity of lithospheric thickness is sampled by the rotational response. Work on this issue is ongoing.

6.4. *Secular Instability of the Rotation Pole*

As demonstrated in Fig. 38, the Pleistocene glacial cycle excites a true wander of the rotation pole relative to the surface geography due to the perturbations of inertia associated with the ice load and with the load- and rotation-induced deformations. This polar motion in fact consists of two parts, the first being a slow oscillation of the pole about the initial equilibrium position, and the second a slow unidirectional drift of the equilibrium position itself. In order to demonstrate that the equilibrium position of the

pole does in fact execute a slow mean drift we may simply average our previously derived solutions over the period of a single glacial cycle. We will consider the homogeneous and stratified cases separately under cases 1 and 2 below.

Case 1. Mean wander speed for the homogeneous model.

If we denote by '$\sim$' the average over a single glaciation–deglaciation cycle and assume the sawtooth cycle described by Eq. (6.45), averaging of Eq. (6.40) gives the result

$$\begin{aligned} \dot{\tilde{m}}_1(t) &= \frac{\Omega}{A\sigma_0}\gamma(1+\bar{\mu})P_1\tilde{f}(t) \\ &= \gamma\frac{1+\bar{\mu}}{\bar{\mu}}\frac{a^2\sin\theta\cos\theta}{C-A}\frac{L_2^1}{2}l_s \end{aligned} \tag{6.66}$$

which is obviously nonzero only because $l_s \neq 0$. Since this number is exactly one-half the instantaneous speed of wander which would be observed following removal of an equilibrated load which is given by the expression for $t > b$ in Eq. (6.44), and since this has been plotted for various values of the viscosity of the model in Fig. 37a, we see that $\dot{\tilde{m}}_1(t) \approx -0.18°/10^6$ yr. which is near the value of $-0.2°/10^6$ yr found by Sabadini and Peltier (1981). In fact, Eq. (6.62) is identical to Eq. (57) of Sabadini and Peltier (1981), so that their calculation of the mean drift speed was not in error even though their calculation of the time-dependent polar motion was completely erroneous. This number of $-0.2°/10^6$ yr is sufficiently large that it could conceivably be important to the mechanism of climatic change itself and might in fact be observable in the paleomagnetic record as a residual true polar wander (TPW) after the data are corrected for the known drifts of the continents relative to the hot-spot frame. The question is at least sufficiently interesting that we should proceed to examine the magnitude of $\dot{\tilde{m}}_1(t)$ for realistic stratified viscoelastic models of the planet. We note further that the mean speed is negative [θ in Eq. (6.62) is negative], so that on the average the Hudson Bay region is moving slowly toward the equator at the computed rate.

Case 2. Mean wander speed for stratified viscoelastic models.

The mean speed of polar wander over the Ice Age cycle for layered models may be determined by direct averaging of Eq. (6.57). Since $\dot{\tilde{f}} \equiv 0$, this average may be written

$$\dot{\tilde{m}}_1(t) = \frac{\Omega\alpha}{A\sigma_0}\left\{-\frac{q(0)}{\prod_i \lambda_i}\tilde{f}(t) + \sum_{i=1}^{M-1}\left[\frac{q(-\lambda_i)}{\lambda_i \prod_{j\neq i}(\lambda_j - \lambda_i)} + \sum_{j=1}^{M}\frac{r_j/s_j}{l_s}\frac{R_j(-\lambda_i)}{\prod_{k\neq i}(\lambda_k - \lambda_i)}\right]\frac{\tilde{dh}_i}{dt}\right\} \tag{6.67}$$

where each of the terms $\tilde{dh}_i/dt$ has the explicit form

$$\begin{aligned}\frac{\tilde{dh}_i}{dt} = &-\beta\frac{(1-e^{-\lambda_i\Delta T})}{\gamma\,\Delta T} + \frac{1}{\gamma\,\Delta T} - \frac{e^{-\lambda_i\Delta t}}{\gamma^2(\Delta T)^2}(1-e^{-\lambda_i\Delta T}) \\ &- \frac{\beta}{\gamma\,\Delta t}e^{-\lambda_i\Delta T}(1-e^{-\lambda_i\Delta t}) + \frac{e^{\lambda_i\Delta t}(1-e^{-\lambda_i\Delta t})}{\gamma^2(\Delta t)^2} \\ &- \frac{e^{\lambda_i(\Delta t-\Delta T)}}{\lambda_i\,\Delta t} - \frac{e^{\lambda_i(\Delta t-\Delta T)}}{\gamma^2\,\Delta t\,\Delta T}(1-e^{\lambda_i\Delta T})(1-e^{-\lambda_i\Delta t})\end{aligned} \tag{6.68}$$

which is clearly nonzero. The factor β is the same as in Eq. (6.58d) and accounts for the memory of the system of the past N cycles. Because the two terms in Eq. (6.68) which contain β do not cancel, it is clear that the average speed of polar wander over each cycle will be a function of time. In Fig. 40 we show a plot of the mean speed of polar drift, and the angular drift itself, as a function of the cycle number in the load history for one of the previously described viscoelastic models. For model I the average speed over 30 cycles of the periodic sawtooth history is $\sim 0.005°/10^6$ yr, which is about two orders of magnitude *less* than the mean drift speed given by Eq. (6.66) for the homogeneous model. The effect of the viscoelastic layering of the planet upon the predicted drift speed is therefore extremely important. To understand how this comes about we may simply inspect the dominant term in Eq. (6.67), which is proportional to the first term in brackets on the right-hand side. For the homogeneous model this term is simply $-\gamma\tilde{f}(t)$, whereas for a three-mode layered model it is

$$F = -\frac{s_1 s_2 s_3}{\lambda_1\lambda_2}\tilde{f}(t) \tag{6.69}$$

Since the three-mode model is a good approximation to the spectrum of model I, if we associate s_1, s_2, and s_3 with the M0, C0, and M1 modes, respectively, inspection of Eq. (6.69) immediately explains the slow drift speed obtained for the layered model. For model I we have $s_1 = 2.763$, $s_2 = 0.3746$, $s_3 = 5.318 \times 10^{-4}$, $\lambda_1 = 1.438$, and $\lambda_2 = 0.0421$. Since $\tilde{f}(t) = 0.5$, evaluation of Eq. (6.69) gives $F = -4.59 \times 10^{-3}$ whereas for the layered model $-\gamma\tilde{f}(t) = -4.6$. It is quite clear then that $|F| \ll |-\gamma\tilde{f}(t)|$

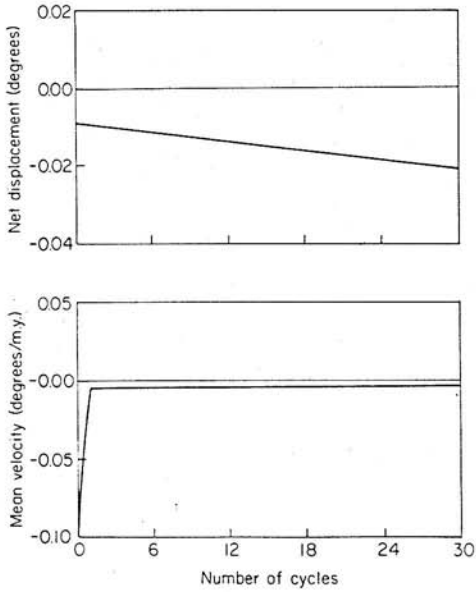

FIG. 40. (a) Net angular deflection of the rotation pole relative to the surface geography for viscoelastic model I. (b) Variation of the "mean" speed of polar wander as a function of the number of the glaciation–deglaciation cycle.

because of the long relaxation time s_3^{-1} associated with the M1 mode. Insofar as the mean drift speed is concerned, this slowest decaying mode is therefore the rate-controlling mechanism. This can be understood physically by recognizing that in order to effect a mean drift of the rotation pole relative to the geography, the equatorial bulge associated with the basic rotation must execute the same net drift and this occurs at a rate governed by the spectrum of the degree-two harmonic. As we have seen, this contains at least one important mode with an extremely long relaxation time. This long relaxation time appears to stabilize the system.

That realistic layered viscoelastic models should be rotationally stable to cyclic ice sheet forcing is in contradiction to the recent claims to the contrary which have appeared in Sabadini *et al.* (1982a,b). Their calculations are, however, marred by the mathematical error mentioned previously and are therefore misleading. It does not seem that the analysis of the recent paleomagnetic record by McElhinny (1973) and Jurdy and van der Voo (1974), as revised by Morgan (1981) and Jurdy (1981), which suggests the existence of as much as 10°–15° of net TPW since the Cretaceous, could then be explained by ice sheet forcing.

In the next section we will focus upon an attempt to understand the mechanism of climatic change which is responsible for the observed 10^5-yr glaciation cycle.

7. Glacial Isostasy and Climatic Change: A Theory of the Ice Age Cycle

There are at least two major unsolved problems connected with variations of global atmospheric climate on the time scale of 10^4–10^7 yr. The first of these problems has to do with the question of the origin of ice ages. That is, how and why do ice ages such as the one which has marked the present Pleistocene period originate? Although the geological record shows evidence of several such periods during the past few billion years, they nevertheless appear to be somewhat unusual. Since the current ice age has lasted only about 2×10^6 yr, and since no substantial change of the degree of polar continentality can have occurred on this time scale, it appears that polar continentality alone cannot provide the explanation for ice age occurrence. The question remains open. In this section we will address a second important question, which concerns the explanation of the almost periodic succession of ice sheet advances and retreats which has characterized the present ice age and which is illustrated so clearly in the record of $^{18}O/^{16}O$ variations obtained from deep-sea sedimentary cores. An example of one such oxygen isotope stratigraphy from Shackleton and Opdyke (1973) was reproduced in Fig. 32a and has been employed in our theoretical analysis of the adjustment process in order to provide control on the characteristic time scale of ice sheet advances and retreats required to estimate the importance of deviations from initial isostatic equilibrium. In this section we will argue that the observed quasi-periodic oscillation of the main Northern Hemisphere ice sheets revealed by these data is due to the excitation, by fluctuations in the effective insolation, of a systemic free relaxation oscillation which is supported in crucial part by the process of glacial isostatic adjustment.

7.1. Oxygen Isotope Stratigraphy and the Observed Spectrum of Climate Fluctuations on the Time Scale 10^4–10^6 Years: The Milankovitch Hypothesis

Analysis of oxygen isotopic records such as that shown in Fig. 32a has recently led to an intense revival of interest in the astronomical theory of

the ice ages which was so strongly advocated by Milankovitch (1941) but which had also been discussed earlier by Adhémar, von Humbolt, and Croll (e.g., see Imbrie and Imbrie, 1978, for an interesting nontechnical discussion). The astronomical theory of long time scale paleoclimatic fluctuations asserts that the observed oscillations of Pleistocene climate are controlled entirely by changes in the effective insolation received by the earth. Variations in the radiation intensity are governed by the temporal changes in the parameters of the earth's orbit produced by the varying gravitational attraction of other planets in the solar system. Milankovitch's contribution to this idea was to perform the first laborious set of calculations to determine, as a function of latitude and season, the time variations of insolation which would have been produced over the past several hundred thousand years of orbital history. His calculations have been superseded in the more recent literature, however, first by Vernekar (1972, 1974) and more recently by Berger (1978). Figure 41 is redrawn from Birchfield and Weertman (1978) and shows a power spectrum of the insolation time series of Berger (1978) for lat 60° N, which is near the latitude of the maximum thickness of Laurentide ice. The spectrum of insolation variations clearly contains energy at three very well defined periods, these being 19,000, 23,000, and 41,000 yr. The first two peaks are due to the precession of the equinoxes, whereas the third is due to the periodic variation of orbital obliquity. It is crucial for our present purposes to note that there is essentially *no* variance in the insolation time series at a period of 10^5 yr, yet by inspection of Fig. 32a we can see, even visually, that the history of ice volume fluctuations is dominated by a periodic oscillation on this time scale. The ideas which we will develop in this section are concerned with an attempt to explain how the

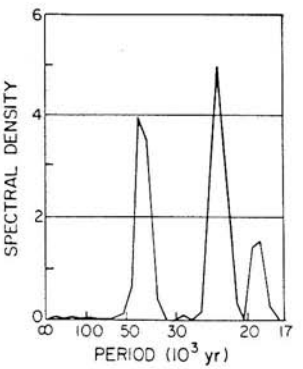

FIG. 41. Power spectrum of the insolation time series of Berger (1978) for 60° latitude. Note the absence of energy at periods near 10^5 yr.

astronomical forcing on the precession and obliquity time scales might be transformed into a response which is dominantly on the time scale of 10^5 yr. To understand this we will clearly have to invoke nonlinear processes. Before discussing the model which we have developed to resolve this problem, however, it is useful to attempt to quantify the extent of the dominance of the 10^5-yr oscillation in the stratigraphic record of oxygen isotopic variability.

In Fig. 42 we show a sequence of plots of the isotopic ratio $^{18}O/^{16}O$ as a function of depth in centimeters in several Pacific and Atlantic deep-sea cores based upon data in Imbrie *et al.* (1973) and Shackleton and Opdyke (1973, 1976) as composited in Oerlemans (1980). In order to transform these isotopic depth series into time series we have to be able to locate at least one time horizon at some depth in the core, and the only method by which it has proved possible to do this is by locating the depth of occurrence

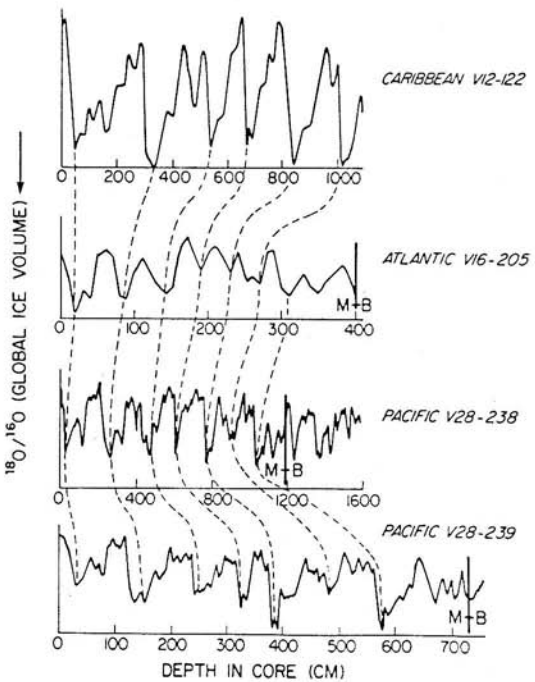

FIG. 42. A comparison of oxygen isotope records from four different deep-sea sedimentary cores based upon data from Imbrie *et al.* (1973) and Shackleton and Opdyke (1973, 1976). The heavy vertical bars marked M–B denote the depth corresponding to the Matuyama–Brunhes boundary of age 730 (±20) kyr.

of the faunal extinctions which mark the last change in polarity of the earth's magnetic field. This occurred 730,000 yr B.P. (Cox and Dalrymple, 1967; Mankinen and Dalrymple. 1979) with an error which is at most ±20,000 yr and is called the Matuyama–Brunhes transition. This horizon has now been located in a reasonable number of sedimentary cores and, subject to the assumption of constant sedimentation rate at each site, leads to a linear mapping of the depth scale to a time scale. For the records shown in Fig. 42, on which the dashed lines join constant time horizons, it is quite clear that the rate of sedimentation varies from site to site. Clearly the cores from sites characterized by high rates of sedimentation will preserve a higher resolution record of the climatic variability than will cores from sites with low sedimentation rates. The sedimentation rate in core V28-238 is about 2 cm/10^3 yr, whereas that in core V28-239 is closer to 1 cm/10^3 yr.

The most useful representation of the time series obtained by transformation of the data to the time domain is in terms of the quantity $\delta^{18}O$, which is simply the variation in the concentration of ^{18}O measured in parts per thousand relative to the ^{16}O concentration. It is quite generally accepted, as argued in Shackleton (1967) and Shackleton and Opdyke (1973), that this isotopic anomaly (measured in foraminifera tests contained in the sediments) provides a direct measure of the ice bound in continental ice complexes. Time series of this isotopic anomaly from cores V28-238 and V28-239 are shown in detail in Birchfield *et al.* (1981), and in Fig. 43 we show reproductions of the power spectra of these time series from this paper. These spectra show in a completely unambiguous way that the variance in the ice volume record is dominantly contained in the oscillation with period 10^5 yr, a fact which was first established by Hays *et al.* (1976), who performed similar analysis on the data extracted from core RC11-120, which was also

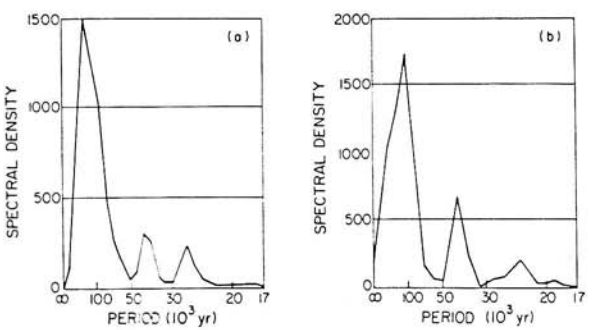

FIG. 43. Power spectra of the $\delta^{18}O$ time series from Pacific cores V28-238 (a) and V28-239 (b) reproduced from Birchfield *et al.* (1981). Note the dominance of the spectral peak near a period of 10^5 yr.

analyzed by Shackleton (1977). Besides the dominant oscillation at 10^5-yr period, however, the spectra clearly show statistically significant variance at the astronomical periods of ~41,000 and ~23,000 yr. Hays *et al.* (1976) argued on the basis of similar power spectra which they obtained from core RC11-120 and one other that the results demonstrated the validity of the astronomical theory of the ice ages. They certainly do establish that the cryosphere responds to the astronomical forcing, since both the precession and obliquity periods do appear in the power spectra of $\delta^{18}O$. However Hays *et al.* (1976) were not able to explain why the dominant cryospheric response consisted of a quasi-periodic 10^5-yr oscillation when the astronomical forcing contained no power at this period (Fig. 41). Birchfield *et al.* (1981) have recently proposed a model which attempts to explain this observation, and although it achieved very limited success, it is nevertheless instructive since it does contain what appear to be the main physical ingredients which are required to understand the phenomenon.

7.2. A Preliminary Model of the Pleistocene Climatic Oscillation

The model of Pleistocene climate proposed by Birchfield *et al.* (1981) basically consists of a model for ice sheet flow, which is forced by a particular accumulation function, coupled to a model of glacial isostatic adjustment. The model is used to describe the expansion and contraction of a circumpolar ring of ice whose northern boundary is constrained to the coast of the polar sea (Fig. 44). The model consists of the following simultaneous partial differential equations:

$$\frac{\partial h}{\partial t} = \frac{\lambda}{r^4 \sin\theta} \frac{\partial}{\partial \theta}\left[\sin\theta\, H^5 \left(\frac{\partial h}{\partial \theta}\right)^3\right] - \tau^{-1}h + q^{-1}h + A \tag{7.1}$$

$$\frac{\partial h'}{\partial t} = -q^{-1}h^1 + \tau^{-1}h \tag{7.2}$$

In these equations $h(\theta, t)$ is the height of the ice sheet above sea level (where θ is the latitude), $H(\theta, t)$ is ice sheet thickness, and $h'(\theta, t)$ is the depth to bedrock below sea level. Equations (7.1) and (7.2) also contain several important parameters which Birchfield *et al.* (1981) specify as

$$\tau = \frac{2\nu k_H}{\rho g} \tag{7.3a}$$

$$q = \frac{2\nu k_H}{\Delta\rho g} \tag{7.3b}$$

$$\lambda = \tfrac{1}{5}(\rho g)^3 \hat{c} \tag{7.3c}$$

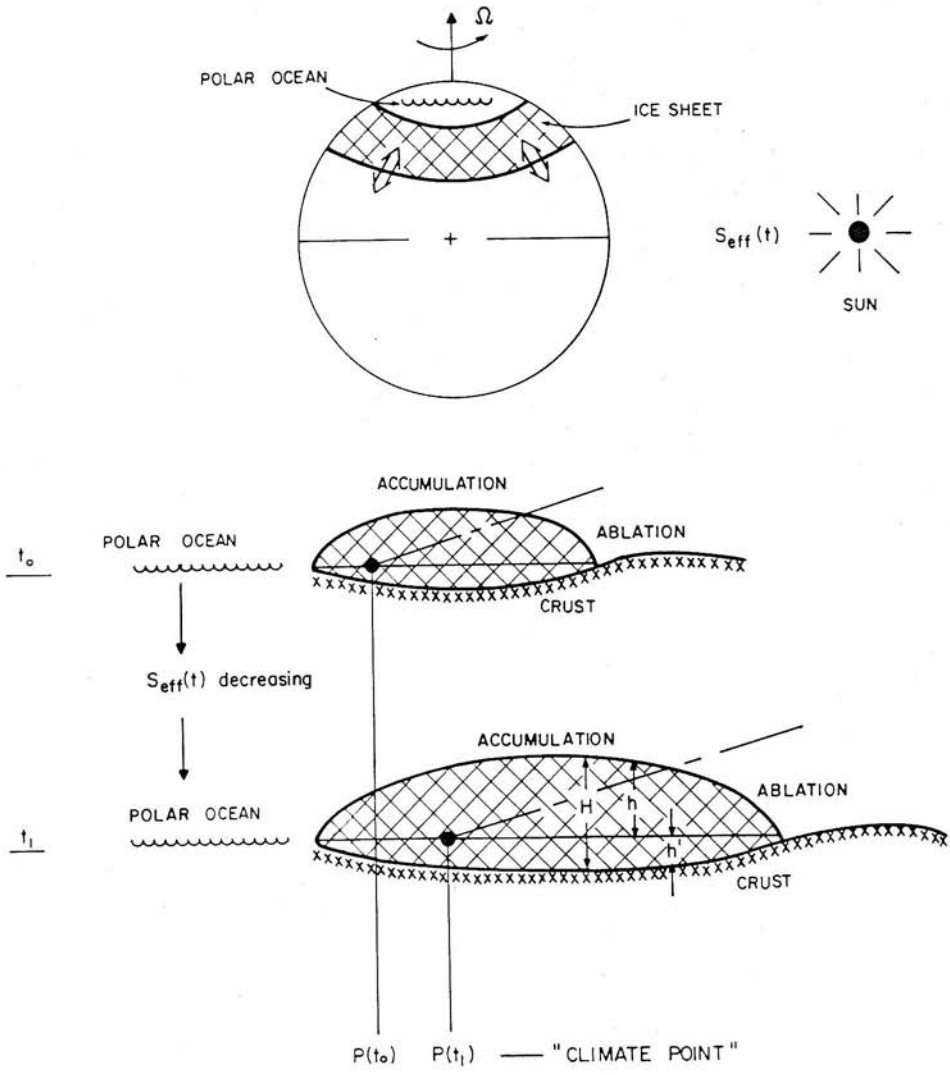

FIG. 44. Schematic diagram for the paleoclimatic model which consists of an active ice sheet driven by variations of the effective insolation as modified by the process of isostatic adjustment.

In Eq. (7.3a). τ is the relaxation time for a harmonic deformation of wave number k_H (Haskell, 1937) of a plane half-space with constant viscosity ν and density ρ. The parameter q in Eq. (7.3b) is a time scale which depends upon the density difference $\Delta\rho$ between ice and rock, while λ in Eq. (7.3c)

arises from use of the Glen flow law (e.g., Paterson, 1981) to describe the ice flux supported by a given surface slope $\partial h/\partial\theta$. The final crucial ingredient in the Birchfield *et al.* (1981) model is the accumulation function A through which the feedback loop in the model is connected. Birchfield *et al.* assume that the accumulation rate A depends upon the height of the ice sheet above sea level and take this dependence to be of the form

$$\begin{aligned} A &= a(1 - bh) > 0, \quad \text{above the firn line} \\ A &= a'(1 - bh) < 0, \quad \text{below the firn line} \end{aligned} \tag{7.4}$$

where $a > 0$ and $a' < 0$ are accumulation and ablation rates, respectively, at mean sea level. The firn line (e.g., Paterson, 1981) is the intersection of the snow line with the ice sheet and separates the zones of ablation and accumulation. Birchfield *et al.* (1981) introduce solar forcing into their model by direct variation of the latitudinal location of the snow line by an amount proportional to the insolation anomaly. They compute the shift in latitude δx from the expression

$$\delta x = -C\,\delta Q \tag{7.5}$$

where δQ is the insolation anomaly, and determine the constant C from the present day insolation gradient as

$$C = \frac{1}{(dQ/dx)} \tag{7.6}$$

Birchfield *et al.* (1981) describe several numerical experiments in which the model (7.1, 7.2) is integrated forward in time using Berger's (1978) insolation anomaly time series and the parameter values

$$\begin{aligned} \tau &= 1 \times 10^{-23}\ \text{sec}^{-1}\ \text{Pa}^{-3} \qquad a = 1.2\ \text{m/yr} \\ C &= 43.35\ \text{W/m}^2\ \text{km} \qquad a' = -2.7\ \text{m/yr} \end{aligned} \tag{7.7}$$

They have also assumed a constant value for τ in Eq. (7.3a) of

$$\tau = 3000\ \text{yr} \tag{7.8}$$

based upon the time scale which is observed to dominate the RSL records in Hudson Bay and Fennoscandia. They therefore implicitly employ a constant effective scale for the ice sheet, in spite of the fact that its actual scale is time dependent. Forward integration of this model leads to a prediction of the time variation of ice sheet volume which may be compared directly to the observed time series of $\delta^{18}O$. In Fig. 45 we have reproduced a power spectrum from their paper of the ice volume history predicted by the model. Although the response does contain significant power at the lower frequency end of the spectrum, there does not exist a sharp line at a period of 10^5 yr

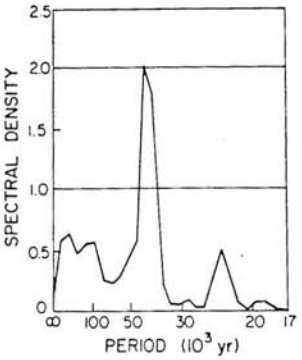

FIG. 45. Power spectrum of the ice volume time series predicted by the model of Birchfield *et al.* (1981). Note that although there is some energy in the low-frequency region of the spectrum, it is overwhelmed by that at the period of the astronomical forcing and is rather diffuse rather than concentrated in a well-defined spectral line.

and the response at the input obliquity period strongly dominates, with the response at the precession period also evident and of strength equal to that at low frequency.

Birchfield *et al.* (1981) attempt to reconcile the unsatisfactory result shown in Fig. 43 by arguing that the spectrum should actually have a "red noise" background added to it which would of course produce a relative enhancement of the power at low frequency. This argument is of course entirely *ad hoc*, and it would be much more satisfactory if it were possible to design a model which could deliver a much closer facsimile of the observed signal of ice volume fluctuations.

A suggestion as to how this problem might be resolved is contained in Oerlemans (1980), who employs a model which is virtually identical to that in Birchfield *et al.* (1981). The only significant difference is in fact that Oerlemans has treated the constant relaxation time τ in Eq. (7.3a) to be a variable rather than a fixed parameter. Figure 46 shows a result obtained by Oerlemans (1980) with a model forced at a single period of 20 kyr (approximately equal to the precession period) both excluding and including the effect of isostatic adjustment under the ice load and for various choices of the isostatic adjustment time scale τ. This figure establishes the adjustment time τ as a crucial variable in the model. When the adjustment time is short the response is almost entirely on the time scale of the forcing (the result obtained by Birchfield *et al.*, 1981). On the other hand, when the time scale is long, $\tau \gtrsim 10$ kyr, the ice volume builds up slowly and then

collapses after about 10^5 yr, in the way which is suggested by the $^{18}O/^{16}O$ data. Oerlemans (1980) describes a sequence of Milankovitch experiments which are somewhat indecisive since they do seem to indicate a fairly pronounced sensitivity to the choice of τ.

We are therefore at something of an impasse. The careful ice volume predictions by Birchfield *et al.* (1981), based upon a value of τ which is obtained from the sea level data, show that the model fails to predict the observed oscillation. The initial calculations of Oerlemans (1980), however, which use a relaxation time very much in excess of that implied by the sea level record, seem to suggest that an oscillation of the observed type is supported under such conditions. These results suggest an explanation in terms of a more accurate description of the isostatic adjustment process in the model. We have shown in the preceding sections of this paper that the sea level record is sensitive only to the shortest relaxation times in the

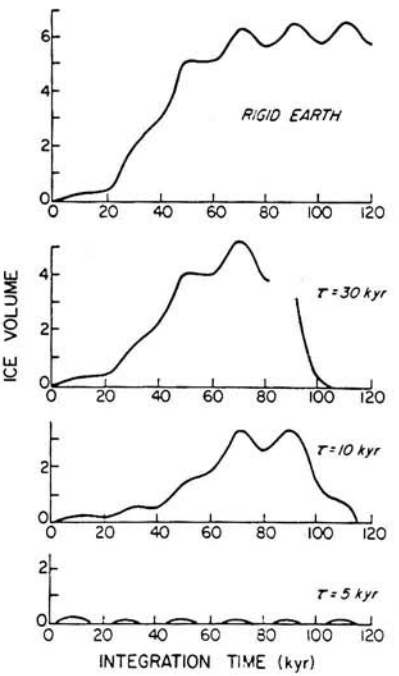

FIG. 46. Time series of ice volume fluctuations predicted by the model of Oerlemans (1980) for several different values of the isostatic adjustment time scale τ. Note that as τ increases the model seems to sustain an oscillation with a time scale near 10^5 yr although there is no forcing at this period.

relaxation spectrum of a realistic earth model. We have furthermore shown that such relaxation spectra also contain certain modes of relaxation with long characteristic relaxation time which are supported by the internal density jumps in the mantle at the olivine → spinel and the spinel → post-spinel phase boundaries. Just as these modes are required to explain the observed gravity anomalies over the centers of rebound, they may also be necessary to understand the oscillatory nature of the Pleistocene climate cycle. In order to test this hypothesis we are obliged to develop a much more accurate model of the coupling between ice flow and glacial isostatic adjustment than that which is embodied in Eqs. (7.1) and (7.2). This is described in the next subsection.

7.3. *A Spectral Model with Isostatic Adjustment: The Feedback between Accumulation Rate and Ice Sheet Topographic Height*

The new model which we will develop here is based upon the same equation for the flow of a thin ice sheet which underlies Eq. (7.1) and can be expressed in the form

$$\frac{\partial H}{\partial t} = -\frac{1}{r \sin\theta}\frac{\partial}{\partial \theta}(\sin\theta\, U) + A(\theta, t) \tag{7.9}$$

where the ice flux U is given by

$$U = \frac{1}{5}\hat{c}(\rho g)^3 H^5 \left(-\frac{1}{r}\frac{\partial h}{\partial \theta}\right)^3$$

which derives from the Glen flow law (Paterson, 1981), where again h is the height of the ice above sea level and H is its thickness. It is useful to expand $H = h + h'$ as before and to rewrite Eq. (7.9) in the form of a nonlinear diffusion equation as

$$\frac{\partial h}{\partial t} = \frac{1}{r \sin\theta}\frac{\partial}{\partial \theta}\left(\sin\theta\, K \frac{\partial h}{\partial \theta}\right) - \frac{\partial h'}{\partial t} + A(\theta, t) \tag{7.10}$$

where the nonlinear diffusion coefficient which determines the rate of flow of the ice sheet is

$$K = \frac{1}{5}\hat{c}(\rho g)^3 \frac{H^5}{r^3}\left(\frac{\partial h}{\partial \theta}\right)^2 \tag{7.11}$$

Our generalization of the model embodied in Eqs. (7.1) and (7.2) will be to derive a new equation for h' to replace Eq. (7.2) which gives a more accurate description of the process of glacial isostatic adjustment. In Section

3 we showed that the radial displacement $h'(\theta, \lambda, t)$ produced by an arbitrary ice sheet of thickness $H(\theta, \lambda, t)$ could be obtained by direct convolution of the surface load and the Green's function for radial displacement defined in Eq. (3.38). This may be expressed as

$$h'(\theta, \lambda, t) = \int dt' \iint d\Omega' \, u_r(\theta/\theta', \lambda/\lambda', t/t')\rho_I H(\theta', \lambda', t') \tag{7.12}$$

Use of the Love number expansion for u_r in terms of Legendre polynomials, the spherical harmonic decomposition of H for an axially symmetric load, and the addition theorem and orthogonality properties of spherical harmonics, reduces Eq. (7.12) to the form

$$\begin{aligned} h'_l(t) = {} & \frac{a}{m_e} \frac{4\pi}{(2l+1)} \sum_j r_j^l e^{-s_j^l t} \int_{-\infty}^{t} dt' e^{s_j^l t'} H_l(t') a^2 \rho_I \\ & + \frac{a}{m_e} \frac{4\pi}{(2l+1)} q_l^E H_l(t) a^2 \rho_I \end{aligned} \tag{7.13}$$

where q_l^E have been used here to denote the elastic Love numbers, and the H_l are the spherical harmonic amplitudes in the decomposition of ice thickness. Now Eq. (7.13) may be converted to an exact differential equation to replace the approximate equation (7.2) by direct time differentiation to obtain

$$\begin{aligned} \frac{\partial h'_l}{\partial t} = {} & \frac{a}{m_e} \frac{4\pi}{(2l+1)} \sum_j (-r_j^l s_j^l) \, e^{-s_j^l t} \int_{-\infty}^{t} dt' \, e^{s_j^l t'} H_l(t') a^2 \rho_I \\ & + \frac{a}{m_e} \frac{4\pi}{(2l+1)} \sum_j r_j^l \, H_l(t) a^2 \rho_I + \frac{a}{m_e} \frac{4\pi}{(2l+1)} q_l^E \frac{dH_l}{dt} a^2 \rho_I \end{aligned} \tag{7.14}$$

A spectral form of Eq. (7.10) may be derived to accompany Eq. (7.14) by expanding $H = h + h'$, K, h, and A in terms of Legendre polynomials. When these expansions are substituted into Eq. (7.10) and this equation multiplied through by P_e and integrated from $\cos\theta = -1$ to $\cos\theta = +1$ we obtain the following spectral form of the nonlinear diffusion equation:

$$\frac{\partial h_l}{\partial t} + \frac{\partial h'_l}{\partial t} = B_{lmn} K_m(t) h_n(t) + A_l(t) \tag{7.15}$$

where the interaction matrix B_{lmn} is

$$\begin{aligned} B_{lmn} = -\frac{(2l+1)}{2a} \int_{-1}^{+1} dx \, P_l(x) \Bigg[& \frac{x}{(1-x^2)^{1/2}} P_m(x) P_n(x) \\ & + P'_m(x) P'_n(x) + P_m(x) P''_n(x) \Bigg] \end{aligned} \tag{7.16}$$

which has elements which depend only upon the basis functions P_l and which may be computed once and for all.

The model embodied in Eqs. (7.14) and (7.15) is a spectral model which replaces Eqs. (7.1) and (7.2) and which, although it contains the same physics as the original model, embodies a much more accurate description of the isostatic adjustment process which appears to be crucial to understanding the nature of the 10^5-yr oscillation in the continental ice volume record of the Pleistocene period. Although we will not describe here a set of Milankovitch experiments with this model, we will, in the next subsection, provide a preliminary analytic exploration of its basic properties which leads to a particularly simple expression for the period of the free relaxation oscillation which the model supports.

7.4. *An Analysis of the Properties of a Reduced Form of the Spectral Model*

The complexity of the isostatic adjustment equation (7.14) is almost entirely due to the fact that each harmonic amplitude of the deformation has several modes of relaxation accessible to it. In this subsection we will focus on the reduced form of the model which obtains when each harmonic decay may be approximated by a single exponential relaxation. This approximation reduces Eqs. (7.14) and (7.15), after considerable algebra, to

$$\frac{\partial h_l}{\partial t} = \frac{1 - C_l q_l^{\mathrm{E}}}{1 - 2C_l q_l^{\mathrm{E}}} B_{lmn} K_m(t) h_n(t) + \frac{1 - C_l q_l^{\mathrm{E}}}{1 - 2C_l q^{\mathrm{E}}} A_l(t) - C_l s^l \frac{q_l^{\mathrm{E}} + r^l/s^l}{1 - 2C_l q_l^{\mathrm{E}}} h_l(t) + \frac{1 - C_l(q_l^{\mathrm{E}} + r^l/s^l)}{1 - 2C_l q_l^{\mathrm{E}}} h_l'(t) \tag{7.17}$$

$$\begin{aligned}\frac{\partial h_l'}{\partial t} = &- \frac{C_l q_l^{\mathrm{E}}}{1 - 2C_l q_l^{\mathrm{E}}} B_{lmn} K_m(t) h_n(t) - \frac{C_l q_l^{\mathrm{E}}}{1 - 2C_l q_l^{\mathrm{E}}} A_l(t) \\ &+ \left[\frac{C_l r^l}{1 - C_l q_l^{\mathrm{E}}} + \frac{C_l q_l^{\mathrm{E}} s^l}{1 - C_l q_l^{\mathrm{E}}} + \frac{C_l^2 q_l^{\mathrm{E}} s^l (q_l^{\mathrm{E}} + r^l/s^l)}{(1 - C_l q_l^{\mathrm{E}})(1 - 2C_l q_l^{\mathrm{E}})} \right] h_l(t) \\ &+ \left[\frac{-s^l}{1 - C_l q_l^{\mathrm{E}}} + \frac{C_l r^l}{1 - C_l q_l^{\mathrm{E}}} + \frac{C_l q_l^{\mathrm{E}} s^l}{1 - C_l q_l^{\mathrm{E}}} \right. \\ &\left. - \frac{C_l q_l^{\mathrm{E}} s^l}{1 - C_l q_l^{\mathrm{E}}} \frac{1 - C_l(q_l^{\mathrm{E}} + r^l/s^l)}{1 - 2C_l q_l^{\mathrm{E}}} \right] h_l(t)\end{aligned} \tag{7.18}$$

which may be enormously reduced if we neglect the elastic part of the response entirely by taking $q_l^{\mathrm{E}} = 0$. This approximation was also invoked

in Birchfield *et al.* (1981) in writing Eq. (7.2) and reduces our spectral equations (7.17) and (7.18) to the set

$$\partial h_l/\partial t = B_{lmn}K_m(t)h_n(t) - C_l r^l h_l + s^l[1 - C_l(r^l/s^l)]h'_l + A_l(t) \quad (7.19)$$

$$\partial h'_l/\partial t = C_l r^l h_l + (-s^l + C_l r^l)h'_l \quad (7.20)$$

in which the constants C_l are defined by

$$C_l = \frac{a}{m_e}\frac{4\pi}{(2l+1)}\rho_1 a^2 \quad (7.21)$$

The nature of the simplified spectral model embodied in Eqs. (7.19) and (7.20) is most clearly revealed by differentiating Eq. (7.19) with respect to t and substituting from Eq. (7.20) to eliminate h' completely. This leads to the following second-order equation for $h_l(t)$:

$$\frac{\partial^2 h_l}{\partial t^2} + \frac{s^l \partial h_l}{\partial t} = B_{lmn}\left[\frac{\partial}{\partial t} + s^l C_l r^l\right]K_m h_n + \left[\frac{\partial}{\partial t} + s^l C_l r^l\right]A_l \quad (7.22)$$

which is relatively innocuous until one introduces the crucial feedback between ice sheet height and accumulation rate which is described by Eq. (7.4). We may rewrite Eq. (7.4) in the form

$$A = a(1 - bh) + E(h) \quad (7.23)$$

where E is a term that is nonzero only below the firn line. Now the Legendre decomposition of Eq. (7.23) gives (for $l \neq 0$)

$$A_l = -abh_l + E_l \quad (7.24)$$

which reduces Eq. (7.22) to the form

$$\frac{\partial^2 h_l}{\partial t^2} + [s^l + ab]\frac{\partial h_l}{\partial t} + ab[s^l + C_l r^l]h_l = B_{lmn}\left[\frac{\partial}{\partial t} + s^l + C_l r^l\right]K_m h_n + \left[\frac{\partial}{\partial t} + s^l C_l r^l\right]E_l \quad (7.25)$$

which is now clearly seen to be the equation for a damped simple harmonic oscillator which is forced by a nonlinear term on the right-hand side, which will input energy to the oscillator at frequencies both higher and lower than those contained in the astronomical forcing, and by the term in E_l, which contains the astronomical forcing itself and some additional but weak h_l dependence. The hypothesis which we wish to put forward here is that the Pleistocene ice age cycle is simply the free relaxation oscillation described by the weakly nonlinear damped simple harmonic oscillator equation (7.25).

With ω_0^2 the squared free oscillation frequency and λ the damping coefficient of the oscillator, Eq. (7.25) may be rewritten as

$$\frac{\partial^2 h_l}{\partial t^2} + 2\lambda \frac{\partial h_l}{\partial t} + \omega_0^2 h_l = B_{lmn}\left[\frac{\partial}{\partial t} + s^l - C_l r^l\right] K_m h_n + \left[\frac{\partial}{\partial t} + s^l - C_l r^l\right] E_l \tag{7.26}$$

where

$$\omega_l^2 = ab[s^l - C_l r^l] \tag{7.27a}$$

$$2\lambda = s^l + ab \tag{7.27b}$$

All of the parameters a, b, s^l, r^l, and C_l are reasonably well known for the geophysical system so that we are in a position to inquire as to whether Eq. (7.26) allows a free oscillation and to determine how close this might be to critical damping. We note first that $\omega_l^2 > 0$ as long as $s^l > C_l r^l$. Now C_l is defined in Eq. (7.21) and may be rewritten as

$$C_l = \frac{3}{(2l+1)} \frac{\rho_I}{\rho_E} \tag{7.28}$$

where ρ_I and ρ_E are the densities of ice and rock respectively. Also, for a homogeneous earth model with density ρ_E, Wu and Peltier (1982a) show that

$$\frac{r^l}{s^l} + q_l^E = \frac{2l+1}{3} \tag{7.29}$$

so that ω_l^2 is positive (with q_l^E small) if $\rho_I/\rho_E < 1$, which is of course true. The squared eigenfrequency of the oscillation ω_l^2 is therefore always greater than zero. Using Eqs. (7.28) and (7.29) we may reexpress Eq. (7.27a) as

$$\omega_l^2 = abs^l(1 - \rho_I/\rho_E) \tag{7.30}$$

on the basis of which we note that as the relaxation time of isostatic adjustment $\tau^l = (s^l)^{-1}$ decreases, the frequency of the oscillation increases. If we insert into Eq. (7.30) the parameters employed by Birchfield *et al.* (1981) which give $ab = 2.76 \times 10^{-4}$ yr^{-1} and $\tau^l = 3 \times 10^3$ yr we predict a period for the oscillation of

$$T_l = \frac{2\pi}{\omega_l} \approx 25{,}000 \text{ yr} \tag{7.31}$$

which is far too low to explain the observed ice cover fluctuation. In order to increase the period of the free relaxation oscillation we need to increase the effective relaxation time of isostatic adjustment. Equally important to

the correct prediction of the period of the oscillation, however, is the extent to which the oscillation is damped. Inspection of Eq. (7.27b) shows that the strength of the damping to which the oscillator is subject decreases as the relaxation time for isostatic adjustment increases, implying that it will be much simpler to sustain a large-amplitude oscillation of low frequency than one of high frequency. Since $ab = 2.76 \times 10^{-4}$ yr^{-1} from Birchfield *et al.*'s data and $s^I = 3.3 \times 10^{-4}$ yr^{-1} we can considerably reduce the damping by increasing the isostatic adjustment time scale. To see how close the system in Birchfield *et al.* (1981) is to critical damping we simply compare λ to ω_0. For their parameters we find

$$\lambda \approx 3.1 \times 10^{-4} \text{ yr}^{-1} \qquad \omega_0 = 2.5 \times 10^{-4} \text{ yr}^{-1} \tag{7.32}$$

so that the system is in fact overdamped and would respond only sluggishly to forcing at the natural oscillation frequency. With the approximation $\rho_I/\rho_E \ll 1$, critical damping with $\lambda \simeq \omega_0$ is obtained for $s^I = ab$ and subcritical damping for $s^I < ab$. The relaxation time $\tau_c = (ab)^{-1}$ is about 3600 yr. Unless the isostatic adjustment time scale is much in excess of this value the damping in the system will be too strong to sustain an oscillation. This provides a very nice explanation as to why Oerlemans (1980) required a relaxation time in excess of about 10^4 yr before any relaxation oscillation was excited by the solar forcing. With $\tau_I = 10^4$/yr we predict a T_I of approximately 5×10^4 yr, which increases to 10^5 yr for $\tau_I = 4 \times 10^4$ yr.

Because the parameters a and b are reasonably well known from meteorological observations and the viscoelastic properties of the earth are equally well constrained by geophysical observations, our physical model of the Pleistocene climatic oscillation which is embodied in Eqs. (7.14) and (7.15) has no adjustable parameters. On the basis of the analysis of a simplified version of the general model discussed in this subsection, we have good reason to believe that it will be able to explain the observed oscillation when the required Milankovitch experiments are performed with it. In order to deliver the observed periodic fluctuation, however, we must rely upon the same long relaxation time modes of realistic viscoelastic earth models which were required to explain the free-air gravity data discussed in Section 5. Only from these modes can we obtain the long characteristic relaxation times which are required to support the observed oscillation.

8. Conclusions

In the main body of this paper we have provided a systematic development of the new theoretical model which has been designed to describe the

phenomena which are associated with glacial isostatic adjustment. This model is based upon a linear viscoelastic constitutive relation between stress and strain, which I have referred to as the generalized Burgers relation, that appears to be uniformly valid in time in the sense that it reconciles not only long time scale adjustment data but also the observations of body wave and free oscillation seismology. In the low-frequency limit which is visible to postglacial rebound, the model behaves like a Maxwell solid so that time-dependent processes are eventually governed by a Newtonian viscous response. By fitting the model to the observables of glacial isostatic adjustment we may infer the variation of mantle viscosity with depth. There are three complementary kinds of data which have proved to be most useful for this purpose: (1) radiocarbon-controlled histories of RSL, (2) surface and satellite observations of the "anomalous" gravitational field related to deglaciation centers, and (3) certain observed properties of the variation of the earth's rotation.

The principal success of the new theoretical model lies in its ability to explain simultaneously the RSL and free-air gravity data. No previous model of glacial isostasy has ever been successful in this regard. The success of the new theory with respect to these two sets of data is based upon the fact that realistic viscoelastic models of the earth's interior support an entire spectrum of normal modes of viscous gravitational relaxation for each deformation wave number, rather than the single mode which is found for homogeneous earth models. In order to reveal this property of the viscoelastic models clearly, we have been obliged to cast the analysis in terms of a normal-mode formalism and we have discussed the intimate connection between this formalism and that for the normal modes of elastic gravitational free oscillation which is so familiar to seismologists. The totality of normal modes, consisting of those which are essentially elastic and oscillatory and those which are essentially viscous and exponentially decaying, are represented by points in the complex plane of the Laplace transform variable s. Normal modes of viscous gravitational relaxation are located on the negative real s axis. The spectrum of such modes spans a wide range of relaxation times, and those with the longest relaxation times, which exist in models which have essentially uniform mantle viscosity, turn out to be crucial to understanding the ability of realistic models to simultaneously explain RSL and free-air gravity data. These modes are supported by the density jumps in the mantle associated with the olivine $\rightarrow$ spinel and the spinel $\rightarrow$ perovskite + magnesiowustite transitions at 420 km and 670 km depth, respectively. Because of the relatively efficient excitation of these modes in models with weak viscosity stratification, the response to a loading event of large spatial scale is initially dominated by a relatively rapid re-

laxation with characteristic time scale near 2×10^3 yr, which is followed after about 8×10^3 yr by a very sluggish approach to the isostatic state on a time scale of about 10^5 yr. This is precisely the behavior which is required to reconcile the RSL data from the Laurentide region, which reveal the short initial time scale only, and the free-air gravity data, which indicate well over 100 m of uplift remaining in the central depression. Models with any substantial increase of viscosity with depth are completely ruled out by *both* the RSL and the free-air gravity observations.

Because of the crucial importance of the modes with long relaxation times in the new theory, we have had to pay particular attention to the question of the influence of the assumption of initial isostatic equilibrium upon the theoretical predictions of RSL and free-air gravity data. We introduced the novel idea in the context of isostatic adjustment studies that the oxygen isotope stratigraphy from deep-sea sedimentary cores could be employed to constrain the previous history of loading and unloading and thus provide us with the essential knowledge necessary to obtain a quantitative estimate of the importance of initial disequilibrium. These data have very clearly established that at least the last 2×10^6 yr of the Pleistocene period have been characterized by a continuous series of ice sheet advances and retreats with successive interglacials separated by a regular time interval near 10^5 yr. Our analysis of the extent to which RSL and free-air gravity data are influenced by initial disequilibrium established that the former measurements are relatively insensitive to disequilibrium effects whereas the latter are influenced to a nonnegligible degree. This demonstration of the complementary nature of RSL and free-air gravity information is very important to understanding the quality of the constraint which these observations provide upon the mantle viscosity profile. When the two sets of data are combined and the influence of initial disequilibrium is taken into account, the data require a mantle viscosity profile in which the viscosity of the upper mantle is near 10^{21} Pa sec and that of the lower mantle is near 3×10^{21} Pa sec, so that viscosity *increases* by a factor of about three across the phase transition at 670 km depth. This inference is entirely based upon a simple two-layer representation of the variation of viscosity in the sublithospheric region. If some modest increase of viscosity were introduced in the upper mantle (say across the 420-km boundary), then that allowed at the 670-km boundary would be reduced. In terms of the new theoretical model, the observed free-air gravity anomaly over Hudson Bay is a very sensitive discriminant between viscosity models.

As we discussed in Section 6 of this paper, it is possible to test the validity of the viscosity profile inferred from the adjustment data through analysis of certain characteristic properties of the earth's rotation. We showed that

both the secular drift of the rotation pole evident in the ILS–IPMS pole path and the observed nontidal acceleration of the earth's rotation are explicable in terms of glacial–deglacial forcing. When the load cycle inferred from the oxygen isotope record is employed through the Euler equations to predict these observations, we find, in the case of the nontidal acceleration, that two quite widely separated values of the mean mantle viscosity are compatible with the observations. The allowed values of $\bar{\nu}$ are near 1.0×10^{21} Pa sec and near 3×10^{22} Pa sec. This basic ambiguity in the interpretation of this datum can be removed only by invoking the RSL and gravity observations, which strongly reject the larger of the two possible roots. The smaller root is beautifully compatible with the isostatic adjustment data, however, so that the observed history of the earth's rotation provides information which enables us to verify the validity of the mantle viscosity profile inferred from them.

Our analysis of the speed of polar wander observed in the ILS pole path showed that this datum had a markedly different dependence upon the parameters of the viscoelastic model than the nontidal acceleration. It was shown to be sensitive not only to mean mantle viscosity but also to lithospheric thickness. Although a low value of the mean mantle viscosity is again preferred by this datum, at the time of writing the trade-off between the effect of lithospheric thickness and that of the viscosity stratification has been insufficiently investigated to allow any unequivocal statement to be made.

The last section of this article was devoted to an application of the new theory of glacial isostasy to an important problem in paleoclimatology which has to do with the explanation of the observed oscillation of ice cover on the 10^5-yr time scale which is so apparent in the oxygen-isotope stratigraphy of sedimentary cores taken from the deep ocean basins. We discussed two recent attempts by Oerlemans (1980) and Birchfield *et al.* (1981) to explain this oscillation using a theory which involved coupling of a model of ice sheet flow subject to insolation forcing with a model of glacial isostatic adjustment. Although the model employed in both these papers was essentially the same, the authors came to diametrically opposite conclusions concerning the plausibility of the proposed mechanism. Oerlemans (1980) found that oscillation was possible on the required time scale but only if the relaxation time for isostatic adjustment of a Laurentide-scale load was taken to be greater than 10^4 yr. Birchfield *et al.* (1981) used a short relaxation time for isostatic adjustment of 3×10^3 yr which was chosen midway between those apparent from the sea level records in Hudson Bay and the Gulf of Bothnia. Their model did not produce the observed oscillation, though it did deliver energy to the low-frequency range due to nonlinear

processes connected with ice flow that were described through the Glen flow law. In Section 7 we derived a theory which incorporated the same basic physical ingredients but which included a correct description of the isostatic adjustment mechanism. In both Oerlemans (1980) and Birchfield *et al.* (1981) the isostatic adjustment component of the model was only crudely approximated though it is crucial to the oscillation. The general form of the spectral model which we derived contained the complete spectrum of modes of relaxation supported by realistic earth models which includes those with long relaxation times which are required to understand the gravity data over Wisconsin Laurentia. These modes could also provide the long relaxation times which are required to support the Pleistocene climatic oscillation. A reduced form of the spectral model was also derived and analyzed to obtain a damped simple harmonic oscillator equation for each component of the ice height spectrum. This equation shows that the period of the relaxation oscillation supported by the feedback between the accumulation rate and ice sheet topographic height may be expressed analytically in terms of the time scale of isostatic adjustment and that determined by the change of the accumulation rate per meter increase of topographic height. Our analysis showed that it would be easiest to oscillate those harmonics of the system with longest characteristic decay time since these had the smallest damping coefficients. The basic ideas in this new theory are the following:

(1) The longest relaxation times necessary to support an underdamped oscillation are supported by the radial structure of realistic viscoelastic earth models.
(2) Energy is forced from the high-frequency solar input to the low natural frequency of the oscillator by the action of nonlinearity due to ice sheet flow.
(3) The energy appears as a sharp peak in the ice volume record because the system is resonant at the natural frequency of the free relaxation oscillation.

Our analysis of the reduced form of the equations of the spectral model shows that this scenario is quite realistic. The Milankovitch experiments which are required to provide a detailed demonstration of the plausibility of this idea will be reported elsewhere.

One idea which we have not developed at all in this article, but which is nevertheless extremely important, concerns the implications of the observed dynamic response of the earth to ice age forcing to our understanding of the mantle convection process. This point has been discussed by Peltier (1980b, 1981b). Of most concern is the question as to whether or not the

magnitude of the viscosity inferred from the rebound data is compatible with theories of the thermal convection process which is responsible for plate creation and destruction. The answer to this question is an unambiguous yes; in fact, one may argue as in the above-cited references that if the mantle viscosity were much different from that inferred from the rebound data then it would be very difficult indeed to produce a theory of the mantle convective circulation. Of equal importance to models of the convective circulation is the inference that there is an increase, by about a factor of about three, of the viscosity across the phase transition at 670 km depth. Although this increase is completely inadequate to confine convection to the upper mantle it could be sufficient to explain the compressive nature of deep seismic focal mechanisms (Isacks and Molnar, 1971). If the upper and lower mantles are filled with separate convective circulations, as some geochemical evidence has been taken to suggest (e.g., De Paolo, 1981), then there should exist a very sharp thermal boundary layer at 670 km depth, since heat could be transported across the boundary only by conduction and the thermal conductivity is low. If the creep activation energy does not change significantly from one side of the phase change to the other (Sammis *et al.*, 1977), then the expected sharp increase in temperature (Jeanloz and Richter, 1979, suggest 500°C) would be accompanied by a decrease of viscosity by several orders of magnitude, and this is not observed. Therefore, either there is no thermal boundary layer at 670 km depth and the mantle convects throughout its volume or there is a sharp increase of creep activation energy at 670 km depth which just offsets the decrease of viscosity which would otherwise be produced by the temperature increase. The only systematic analysis of the expected variation in the creep activation energy is that by Sammis *et al.* (1977) which would strongly suggest that the former possibility is correct. This may not be definitive, however, so that direct experimental measurement of the creep activation energy of the perovskite + magnesiowustite phase would be invaluable.

Peltier (1980b, 1981b) has given a series of arguments based upon dynamical considerations which also support the idea of whole-mantle convection. Of crucial importance among these is that connected with the expected dynamical effects of phase transitions. Richter (1973) has shown that convection through a phase boundary with negative Clapeyron slope such as that at 670 km depth is not significantly impeded by the phase transition. In subsequent analyses the advocates of separate upper and lower mantle circulations have therefore been obliged to invoke the idea that the 670-km discontinuity was a chemical boundary across which there was a significant change of the mean atomic weight of mantle material. A chemical layering would of course prove enormously efficient at preventing convective mixing across the boundary (Richter and Johnson, 1974). Until the

new high-pressure diamond anvil data became available from the group at the Carnegie Institute (Yagi *et al.*, 1979), it was quite possible that the 670-km boundary could have been a chemical boundary since no direct petrological data were available at such high pressures. The new data clearly suggest that this boundary is an equilibrium phase boundary, however, and furthermore show that all of the seismically observed density increase is explicable in terms of the transformation from the less dense to the more dense phase. It would therefore appear that there is no dynamical mechanism available to explain how the separation between separate upper mantle and lower mantle circulations could possibly occur. The only possibility which remains open here, as far as I can see, is that previous calculations of the effect of phase boundaries upon convection are seriously in error. One must either give up the idea of separate upper mantle and lower mantle circulations, and face the geochemical consequences, or demonstrate that convection cannot penetrate a phase boundary with adverse Clapeyron slope. On the basis of this line of argument we can see that the observation from postglacial rebound that the viscosity of the mantle is essentially constant has forced a rather radical rethinking of ideas concerning the mantle convective circulation since it has demonstrated that there is no purely mechanical barrier to the penetration of convection at 670 km depth.

REFERENCES

Aki, K., and Richards, P. G. (1980). "Quantitative Seismology: Theory and Methods." Freeman, San Francisco, California.

Anderson, D. L. (1981). Hotspots, basalts, and the evolution of the mantle. *Science* **213,** 82–89.

Anderson, D. L., and Hart, R. S. (1978). Attenuation models of the earth. *Phys. Earth Planet. Inter.* **16,** 289–306.

Anderson, D. L., and Minster, J. B. (1979). The frequency dependence of Q in the earth and implications for mantle rheology and Chandler wobble. *Geophys. J. R. Astron. Soc.* **58,** 431–440.

Andrews, J. T. (1970). "A Geomorphological Study of Postglacial Uplift with Particular Reference to Arctic Canada." Oxford Univ. Press, London and New York.

Backus, G. E., and Gilbert, J. F. (1967). Numerical applications of a formalism for geophysical inverse problems. *Geophys. J. R. Astron. Soc.* **13,** 247–276.

Backus, G. E., and Gilbert, J. F. (1968). The resolving power of gross earth data. *Geophys. J. R. Astron. Soc.* **16,** 169–205.

Backus, G. E., and Gilbert, J. F. (1970). Uniqueness in the inversion of inaccurate gross earth data. *Philos. Trans. R. Soc. London, Ser. A* **266,** 123–192.

Balling, N. (1980). The land uplift in Fennoscandia, gravity field anomalies and isostasy. *In* "Earth Rheology, Isostasy, and Eustasy" (N.-A. Mörner, ed.), pp. 297–321. Wiley, New York.

Beaumont, C. (1978). The evolution of sedimentary basins on a viscoelastic lithosphere: Theory and examples. *Geophys. J. R. Astron. Soc.* **55,** 471–497.

Berckhemer, H., Auer, F., and Drisler, J. (1979). High temperature anelasticity and elasticity of mantle peridotite. *Phys. Earth Planet. Inter.* **20,** 48–59.

Berger, A. L. (1978). Long term variations of daily insolation and Quaternary climatic changes. *J. Atmos. Sci.* **35,** 2362–2367.

Birchfield, G. E. (1977). A study of the stability of a model continental ice sheet subject to periodic variation in heat input. *JGR. J. Geophys. Res.* **82,** 4909–4913.

Birchfield, G. E., and Weertman, J. (1978). A note on the spectral response of a model continental ice sheet. *JGR. J. Geophys. Res.* **83,** 4123–4125.

Birchfield, G. E., Weertman, J., and Lunde, A. T. (1981). A paleoclimatic model of Northern Hemisphere ice sheets. *Quat. Res. (N.Y.)* **15,** 126–142.

Bloom, A. L. (1963). Late Pleistocene fluctuations of sea level and postglacial crustal rebound in coastal Maine. *Am. J. Sci.* **261,** 862–879.

Braginsky, S. I. (1963). Structure of the F layer and reasons for convection in the earth's core. *Dokl. Akad. Nauk SSSR* **149,** 1311–1314.

Brennan, C. (1974). Isostatic recovery and the strain rate dependent viscosity of the earth's mantle. *JGR. J. Geophys. Res.* **79,** 3993–4001.

Brethau, T., Castaing, J., Rabier, J., and Veyssiere, P. (1979). Movement des dislocations et plasticité à haute temperature des oxydes linaires et ternaires. *Adv. Phys.* **28,** 835–1014.

Broecker, W. S., and Van Donk, J. (1970). Insolation changes, ice volumes, and the O^{18} record in deep sea cores. *Rev. Geophys. Space Phys.* **8,** 169–198.

Brotchie, J. F., and Silvester, R. (1969). On crustal flexure. *JGR. J. Geophys. Res.* **74,** 5240–5252.

Bryson, R. A., Wendland, M. W., Ives, J. D., and Andrews, J. T. (1969). Radiocarbon isochrones on the disintegration of the Laurentide ice sheet. *Arct. Alp. Res.* **1,** 1–14.

Buland, R. P., Berger, J., and Gilbert, F. (1979). Observations from the IDA network of attenuation and splitting during a recent earthquake. *Nature (London)* **277,** 358–362.

Burgers, J. M. (1955). Rotational motion of a sphere subject to viscoelastic deformation. I. II. III. *Proc. K. Ned. Akad. Wet.* **58,** 219–237.

Cathles, L. M. (1975). "The Viscosity of the Earth's Mantle." Princeton Univ. Press, Princeton, New Jersey.

Christensen, R. M. (1971). "Theory of Viscoelasticity: An Introduction." Academic Press, New York.

Clark, J. A., Farrell, W. E., and Peltier, W. R. (1978). Global changes in postglacial sea level: A numerical calculation. *Quat. Res. (N.Y.)* **9,** 265–287.

Cohen, S. C. (1980a). Postseismic viscoelastic surface deformation and stress. 1. Theoretical considerations, displacement, and strain calculations. *JGR. J. Geophys. Res.* **85,** 3131–3150.

Cohen, S. C. (1980b). Postseismic viscoelastic surface deformation and stress. 2. Stress theory and computation, dependence of displacement, strain, and stress on fault parameters. *JGR. J. Geophys. Res.* **85,** 3151–3158.

Cox, A., and Dalrymple, G. B. (1967). Statistical analysis of geomagnetic reversal data and precision of potassium–argon dating. *JGR. J. Geophys. Res.* **72,** 2603–2614.

Crittenden, M. D., Jr. (1963). Effective viscosity of the earth derived from isostatic loading of Pleistocene Lake Bonneville. *JGR. J. Geophys. Res.* **68,** 5517–5530.

Crough, S. T. (1977). Isostatic rebound and power law flow in the asthenosphere. *Geophys. J. R. Astron. Soc.* **50,** 723–738.

Currot, D. R. (1966). Earth deceleration from ancient solar eclipses. *Astron. J.* **71,** 264–269.

Dahlen, F. A., and Fels, S. B. (1978). A physical explanation of the static core paradox. *Geophys. J. R. Astron. Soc.* **55,** 317–332.

Davis, P. A., and Peltier, W. R. (1976). Resonant parallel shear instability in a stably stratified planetary boundary layer. *J. Atmos. Sci.* **33,** 1287–1300.

Davis, P. A., and Peltier, W. R. (1977). Effect of dissipation on parallel shear instability near the ground. *J. Atmos. Sci.* **34,** 1868–1884.

Davis, P. A., and Peltier, W. R. (1979). Some characteristics of the Kelvin–Helmholtz and resonant overreflection modes of shear flow instability and of their interaction through vortex pairing. *J. Atmos. Sci.* **36,** 2394–2412.

De Paolo, D. J. (1981). Nd isotopic studies: Some new perspectives on earth structure and evolution. *EOS Trans.* **62,** 137–140.

Dicke, R. H. (1966). The secular acceleration of the earth's rotation and cosmology. *In* "The Earth–Moon System" (B. G. Marsden and A. G. W. Cameron, eds.), pp. 98–163. Plenum, New York.

Dicke, R. H. (1969). Average acceleration of the earth's rotation and the viscosity of the deep mantle. *JGR. J. Geophys. Res.* **74,** 5895–5902.

Dickman, S. R. (1977). Secular trend of the earth's rotation pole: Consideration of motion of the latitude observatories. *Geophys. J. Roy. Astron. Soc.* **57,** 41–50.

Durham, W. B., and Goetze, C. (1977). Plastic flow of oriented single crystals of olivine. 1. Mechanical data. *JGR. J. Geophys. Res.* **82,** 5737–5754.

Elsen, J. A. (1967). Geology of glacial lake Agassiz. *In* "Life, Land and Water" (W. J. Meyer-Oaks, ed.). pp. 37–43, 71–80. Univ. of Manitoba Press, Winnipeg, Canada.

Emiliani, C. (1955). Pleistocene temperatures. *J. Geol.* **63,** 538–578.

Farrand, W. R. (1962). Postglacial uplift in North America. *Am. J. Sci.* **260,** 181–199.

Farrell, W. E. (1972). Deformation of the earth by surface loads. *Rev. Geophys. Space Phys.* **10,** 761–797.

Farrell, W. E., and Clark, J. A. (1976). On postglacial sea level. *Geophys. J. R. Astron. Soc.* **46,** 647–667.

Fauré, H. (1980). Late Cenozoic vertical movements in Africa. *In* "Earth Rheology, Isostasy, and Eustasy" (N.-A. Mörner, ed), pp. 465–469. Wiley, New York.

Ferry, J. D. (1980). "Viscoelastic Properties of Polymers." Wiley, New York.

Gilbert, F. (1980). An introduction to low frequency seismology. *In* "Physics of the Earth's Interior" (A. M. Dziewonski and E. Boschi, eds.), pp. 41–71. North-Holland Publ., Amsterdam.

Gilbert, F., and Dziewonski, A. M. (1975). An application of normal mode theory to the retrieval of structural parameters and source mechanisms from seismic spectra. *Philos. Trans. R. Soc. London. Ser. A* **278,** 187–269.

Goldreich, P., and Toomre, A. (1969). Some remarks on polar wandering. *JGR. J. Geophys. Res.* **74,** 2555–2567.

Goldstein, H. (1980). "Classical Mechanics," 2nd ed. Addison-Wesley, Reading, Massachusetts.

Greenwood, G. W., Jones, H., and Sritharan, T. (1980). On the transition between dislocation and diffusion creep. *Philos. Mag.* [*Part*] *A* **41,** 871–882.

Gross, B. (1947). On creep and relaxation. I. *J. Appl. Phys.* **18,** 212–216.

Gross, B. (1953). "Mathematical Structure of the Theories of Viscoelasticity." Hermann, Paris.

Hansen, K. (1982). Secular effects of oceanic tidal dissipation on the moon's orbit and the earth's rotation. *Rev. Geophys. Space Phys.* (in press).

Haskell, N. A. (1935). The motion of a viscous fluid under a surface load. 1. *Physics (N.Y.)* **6,** 265–269.

Haskell, N. A. (1936). The motion of a viscous fluid under a surface load. 2. *Physics (N.Y.)* **7,** 56–61.

Haskell, N. A. (1937). The viscosity of the asthenosphere. *Am. J. Sci.* **33,** 22–28.

Hays, J. D., Imbrie, J., and Shackleton, N. J. (1976). Variations in the earth's orbit: Pacemaker of the ice ages. *Science* **194,** 1121–1132.

Heiskanen, W. A., and Vening-Meinesz, F. A. (1958). "The Earth and Its Gravity Field." McGraw-Hill, New York.

Hilaire-Marcel, C., and Fairbridge, R. W. (1978). Isostasy and eustasy in Hudson Bay. *Geology*, Jan. pp. 4–12.

Honkasolo, T. (1963). On the use of gravity measurements for investigation of the land upheaval in Fennoscandia. *Fennia* **89**, 21–23.

Imbrie, J., and Kipp, N. G. (1971). A new micropaleontological method for quantitative paleoclimatology: Application to a late Pleistocene Caribbean core. *In* "Late Cenozoic Glacial Ages" (K. K. Turekian, ed.). Yale Univ. Press, New Haven, Connecticut.

Imbrie, J., and Imbrie, C. P. (1978). "Ice Ages: Solving the Mystery." McMillan, New York.

Imbrie, J., Van Donk, J., and Kipp, N. G. (1973). Paleoclimatic investigation of a late Pleistocene Caribbean deep-sea core: Comparison of isotopic and faunal methods. *Quat. Res (N.Y.)* **3**, 10–38.

Innes, M. J. S., Goodacre, A. K., Weston, A., and Weber, J. R. (1968). Gravity and isostasy in the Hudson Bay region. Pt. V. *Publ. Dom. Obs. (Ottawa)*.

Isacks, B., and Molnar, P. (1971). Distribution of stresses in the descending lithosphere from a global survey of focal mechanism solutions of mantle earthquakes. *Rev. Geophys. Space Phys.* **9**, 103–174.

Jackson, J. D. (1962). "Classical Electrodynamics." Wiley, New York.

Jacobs, J. A. (1976). "The Earth's Core." Academic Press, New York.

Jarvis, G. T., and Peltier, W. R. (1982). Mantle convection as a boundary layer phenomenon. *Geophys. J. R. Astron. Soc.* **68**, 389–427.

Jeanloz, R. (1981). High pressure chemistry of the earth's deep interior. *Am. Chem. Soc., 17th State-of-the-Art Symp.* (in press).

Jeanloz, R., and Richter, F. M. (1979). Convection, composition and the thermal state of the lower mantle. *JGR, J. Geophys. Res.* **84**, 5497–5504.

Jeffreys, H. (1972). Creep in the earth and planets. *Tectonophysics* **13**, 569–581.

Jeffreys, H. (1973). Developments in geophysics. *Annu. Rev. Earth Planet. Sci.* **1**, 1–13.

Jurdy, D. M. (1981). True polar wander. *Tectonophysics* **74**, 1–17.

Jurdy, D. M., and van der Voo, R. (1974). A new method for the separation of true polar wander and continental drift, including results for the past 55 M.Y. *JGR, J. Geophys. Res.* **79**, 2945–2952.

Kohlstedt, D. L., and Goetze, C. (1974). Low stress and high temperature creep in olivine single crystals. *JGR. J. Geophys. Res.* **79**, 2045–2051.

Kukla, G., Berger, A., Lotti, R., and Brown, J. (1981). Orbital signature of interglacials. *Nature (London)* **290**, 295–298.

Lambeck, K. (1977). Tidal dissipation in the oceans: Astronomical, geophysical and oceanographic consequences. *Philos. Trans, R. Soc. London, Ser. A* **287**, 545–594.

Lambeck, J. (1980). "The Earth's Variable Rotation: Geophysical Causes and Consequences." Cambridge Univ. Press, London and New York.

Lerch, F. J., Klosko, S. M., Laubscher, R. E., and Wagner, C. A. (1979). Gravity model improvement using GEOS 3 (GEM 9 and 10). *JGR, J. Geophys. Res.* **84**, 3897–3916.

Libby, W. F. (1952). "Radiocarbon Dating." Univ. of Chicago Press, Chicago, Illinois.

Lidén, R. (1938). Den senkvartära strandförskjutningens förloop och kronologi i Ångermanland. *Geol. Foeren. Stokholm Foerh.* **60**, 397–404.

Litherland, A. E. (1980). Ultrasensitive mass spectrometry with accelerators. *Annu. Rev. Nucl. Part. Sci.* **30**, 437–473.

Liu, H. P., Anderson, D. L., and Kanamori, H. (1976). Velocity dispersion due to anelasticity: Implications for seismology and mantle composition. *Geophys. J. R. Astron. Soc.* **47**, 41–58.

Lliboutry, L. A. (1971). Rheological properties of the asthenosphere from Fennoscandian data. *JGR, J. Geophys. Res.* **76**, 1433–1446.

Löken, O. H. (1962). The late-glacial and postglacial emergence and deglaciation of northernmost Labrador. *Geogr. Bull.* **17,** 23–56.

Longman, I. M. (1963). A Green's function for determining the deformation of the earth under surface mass loads. 2. Computations and numerical results. *JGR. J. Geophys. Res.* **68,** 485–496.

Loper, D. E., and Roberts, P. H. (1978). On the motion of an iron-alloy core containing a slurry. I. General theory. *Geophys. Astrophys. Fluid Dyn.* **9,** 289–321.

McConnell, R. K. (1968). Viscosity of the mantle from relaxation time spectra of isostatic adjustment. *JGR, J. Geophys. Res.* **73,** 7089–7105.

MacDonald, J. R. (1961). Theory and application of a superposition model of internal friction and creep. *J. Appl. Phys.* **3,** 2385–2398.

McElhinny, M. W. (1973). "Paleomagnetism and Plate Tectonics." Cambridge Univ. Press, London and New York.

McKenzie, D. P. (1966). The viscosity of the lower mantle. *JGR, J. Geophys. Res.* **71,** 3995–4010.

McKenzie, D. P. (1967). The viscosity of the mantle. *Geophys. J. R. Astron. Soc.* **14,** 297–305.

McKenzie, D. P. (1968). The geophysical importance of high temperature creep. *In* "The History of the Earth's Crust" (R. A. Phinney, ed.). Princeton Univ. Press, Princeton, New Jersey.

Mankinen, E. A., and Dalrymple, G. B. (1979). Revised geomagnetic polarity timescale for the interval 0–5 my BP. *JGR, J. Geophys. Res.* **84,** 615–626.

Marthinussen, M. (1962). C^{14}-datings referring to shore lines, transgressions, and glacial stages in northern Norway. *Nor. Geol. Unders.* **215,** 37–67.

Milankovitch, M. (1941). "Canon of Insolation and the Ice Age Problem" (translated from the German). U.S. Dept. of Commerce, Israel Program for Scientific Translations (distr. by Davey, Hartford, Connecticut, 1969).

Minster, J. B. (1978). Transient and impulse responses of a one-dimensional linearly attenuating medium. II. A parametric study. *Geophys. J. R. Astron. Soc.* **52,** 503–524.

Minster, J. B., and Anderson, D. L. (1980a). Dislocational and nonelastic processes in the mantle. *JGR. J. Geophys. Res.* **85,** 6347–6352.

Minster, J. B., and Anderson, D. L. (1980b). A model of dislocation controlled rheology for the mantle. *Philos. Trans. R. Soc. London, Ser. A* **299,** 319–356.

Morgan, W. J. (1981). Hotspot tracks and the opening of the Atlantic and Indian Oceans. *In* "The Sea" (C. Emiliani, ed.), Wiley, New York.

Mörner, N.-A. (1980). The Fennoscandian uplift: Geological data and their geodynamic implication. *In* "Earth Rheology, Isostasy, and Eustasy" (N.-A. Mörner, ed.), pp. 251–283. Wiley, New York.

Morrison, L. V. (1973). Rotation of the earth and the constancy of *G*. *Nature (London)* **241,** 519–520.

Müller, P. M. (1975). An analysis of the ancient astronomical observations with the implications for geophysics and cosmology. Ph.D. Thesis, University of Newcastle-upon-Tyne.

Müller, P. M., and Stephenson, F. R. (1975). The acceleration of the earth and moon from early observations. *In* "Growth Rhythms and History of the Earth's Rotation" (G. D. Rosenburg and S. K. Runcorn, eds.), pp. 459–534. Wiley, New York.

Munk, W. H., and MacDonald, G. F. (1960). "The Rotation of the Earth." Cambridge Univ. Press, London and New York.

Nakiboglu, S. M., and Lambeck, K. (1980). Deglaciation effects upon the rotation of the earth. *Geophys. J. R. Astron. Soc.* **62,** 49–58.

Newman, W. S., Cinquemani, L. J., Pardi, R. R., and Marcus, L. F. (1980). Holocene delevelling of the United States east coast. *In* "Earth Rheology, Isostasy, and Eustasy" (N.-A. Mörner, ed.), pp. 449–463. Wiley, New York.

Newton, R. R. (1972). "Medieval Chronicles and the Rotation of the Earth." Johns Hopkins Univ. Press, Baltimore, Maryland.

Nowick, A. S., and Berry, B. S. (1972). "Anelastic Relaxation in Crystalline Solids." Academic Press, New York.

Nur, A., and Mavko, G. (1974). Postseismic viscoelastic rebound. *Science* **183,** 204–206.

O'Connell, R. J. (1971). Pleistocene glaciation and the viscosity of the lower mantle. *Geophys. J. R. Astron. Soc.* **23,** 299–327.

Oerlemans, J. (1980). Some model studies of the ice age problem. Thesis, Publ. No. 158. Koninkliyk Nederlands Meteorologisch Instituut, Utrecht.

Parsons, B. E. (1972). Changes in the earth's shape. Thesis, Cambridge University.

Paterson, W. S. B. (1981). "The Physics of Glaciers." Pergamon, Oxford.

Peltier, W. R. (1974). The impulse response of a Maxwell earth. *Rev. Geophys. Space Phys.* **12,** 649–669.

Peltier, W. R. (1976). Glacial isostatic adjustment. II. The inverse problem. *Geophys. J. R. Astron. Soc.* **46,** 669–706.

Peltier, W. R. (1980a). Ice sheets, oceans, and the earth's shape. *In* "Earth Rheology, Isostasy, and Eustasy" (N.-A. Mörner, ed.), pp. 45–63. Wiley, New York.

Peltier, W. R. (1980b). Mantle convection and viscosity. *In* "Physics of the Earth's Interior" (A. M. Dziewonski and E. Boschi, eds.), pp. 362–431. North-Holland Publ., Amsterdam.

Peltier, W. R. (1981a). Ice Age geodynamics. *Annu. Rev. Earth Planet. Sci.* **9,** 199–225.

Peltier, W. R. (1981b). Surface plates and thermal plumes: Separate scales of the mantle convective circulation. *In* "The Thermal and Chemical Evolution of the Mantle" (R. J. O'Connell and W. Fyfe, eds.), Geodyn. Ser., Vol. 6. Am. Geophys. Union, pp. 59–77.

Peltier, W. R., and Andrews, J. T. (1976). Glacial isostatic adjustment. I. The forward problem. *Geophys. J. R. Astron. Soc.* **46,** 605–646.

Peltier, W. R., Farrell, W. E., and Clark, J. A. (1978). Glacial isostasy and relative sea level: A global finite element model. *Tectonophysics* **50,** 81–110.

Peltier, W. R., Yuen, D. A., and Wu, P. (1980). Postglacial rebound and transient rheology. *Geophys. Res. Lett.* **7,** 733–736.

Peltier, W. R., Wu, P., and Yuen, D. A. (1981). The viscosities of the earth's mantle. *In* "Anelasticity in the Earth" (F. Stacey, M. Paterson, and A. Nicholas, eds.), Geodyn. Ser., Vol. 5, pp. 59–77. Am. Geophys. Union.

Peltier, W. R., and Wu, P. (1982). Comments on [Sabadini *et al.*, 1982b]. *JGR, J. Geophys. Res.* (in press).

Philips, R. J., and Lambeck, K. (1980). Gravity fields of the terrestrial planets: Long-wavelength anomalies and tectonics. *Rev. Geophys. Space Phys.* **18,** 27–76.

Post, R., and Griggs, D. (1973). The earth's mantle: Evidence of non-Newtonian flow. *Science* **181,** 1242–1244.

Richter, F. M. (1973). Finite amplitude convection through a phase boundary. *Geophys. J. R. Astron. Soc.* **35,** 365–276.

Richter, F. M., and Johnson, C. (1974). Stability of a chemically layered mantle. *JGR, J. Geophys. Res.* **79,** 1635–1639.

Ringwood, A. E., and Major, A. (1970). The system Mg_2SiO_4–Fe_2SiO_4 at high pressures and temperatures. *Phys. Earth Planet. Inter.* **3,** 89–108.

Rochester, M. G., and Smylie, D. E. (1974). On changes in the trace of the earth's inertia tensor. *JGR, J. Geophys. Res.* **79,** 4948–4951.

Rundle, J. B., and Jackson, D. D. (1977). A three dimensional viscoelastic model of a strike-slip fault. *Geophys. J. R. Astron. Soc.* **49,** 565–591.

Sabadini, R., and Peltier, W. R. (1981). Pleistocene deglaciation and the earth's rotation: Implications for mantle viscosity. *Geophys. J. R. Astron. Soc.* **66,** 552–578.

Sabadini, R., Yuen, D. A., and Boschi, E. (1982a). Interaction of cryospheric forcings with rotational dynamics has consequences for ice ages. *Nature (London)* **296,** 338–341.

Sabadini, R., Yuen, D. A., and Boschi, E. (1982b). Polar wandering and the forced responses of a rotating, multilayered, viscoelastic planet. *J. Geophys. Res.* **87,** 2885–2903.

Sailor, R. V., and Dziewonski, A. M. (1978). Measurements and interpretation of normal mode attenuation. *Geophys. J. R. Astron. Soc.* **53,** 559–581.

Sammis, C. G., Smith, J. C., Schubert, G., and Yuen, D. A. (1977). Viscosity–depth profile of the earth's mantle: Effects of polymorphic phase transitions. *JGR, J. Geophys. Res.* **82,** 3747–3761.

Sauramo, M. (1958). Land uplift with hinge-lines in Fennoscandia. *Ann. Acad. Sci. Fenn., Ser. A3* **44,** 1–25.

Scheidegger, A. E. (1957). Rheology of the earth: The basic problem of geodynamics. *Can. J. Phys.* **35,** 383–397.

Shackleton, N. J. (1967). Oxygen isotope analyses and Pleistocene temperatures re-addressed. *Nature (London)* **215,** 15–17.

Shackleton, N. J. (1977). The oxygen isotope stratigraphic record of the late Pleistocene. *Philos. Trans. R. Soc. London Ser. B* **280,** 169–182.

Shackleton, N. J., and Opdyke, N. D. (1973). Oxygen isotope and paleomagnetic stratigraphy of equatorial Pacific core V28-238: Oxygen isotope temperatures and ice volumes on a 10^5 and 10^6 year time scale. *Quat. Res. (N.Y.)* **3,** 39–54.

Shackleton, N. J., and Opdyke, N. D. (1976). Oxygen-isotope and paleomagnetic stratigraphy of Pacific core V28-239 late Pleistocene to latest Pleistocene. *Mem.—Geol. Soc. Am.* **145,** 449–464.

Shepard, F. P. (1963). Thirty five thousand years of sea level. *In* "Essays in Marine Geology," pp. 1–10. Univ. of Southern California Press, Los Angeles.

Smith, M. L., and Dahlen, F. A. (1981). The period and Q of the Chandler wobble. *Geophys. J. R. Astron. Soc.* **64,** 223–281.

Smylie, D. E., and Mansinha, L. (1971). The elasticity theory of dislocations in real earth models and changes in the rotation of the earth. *Geophys. J. R. Astron. Soc.* **23,** 329–354.

Takeuchi, H., and Saito, M. (1972). Seismic surface waves. *Methods Comput. Phys.* **11,** 217–295.

Thatcher, W., and Rundle, J. B. (1979). A model for the earthquake cycle in underthrust zones. *JGR, J. Geophys. Res.* **84,** 5540–5556.

Turcotte, D. L. (1979). Flexure. *Adv. Geophys.* **21,** 51–86.

Twiss, R. J. (1976). Structural superplastic creep and linear viscosity in the earth's mantle. *Earth Planet. Sci. Lett.* **33,** 86–100.

Van Bemmelen, R. W., and Berlage, H. P. (1935). Versuch einer mathematischen Behandlung Gestektonischer Bewegungen unter besonderer Beruchsichtigung der Undationstheories. *Gerlands Beitr. Geophys.* **43,** 19–55.

Vening-Meinesz, F. A. (1937). The determination of the earth's plasticity from the postglacial uplift of Scandinavia: Isostatic adjustment. *Proc. K. Ned. Akad. Wet. Amsterdam* **40,** 654–662.

Vernekar, A. D. (1972). Long term global variations of incoming solar radiation. *Meteorol. Monogr.* **34,** 1–21.

Vernekar, A. D. (1974). Variations in insolation caused by changes in orbital elements of the Earth. *In* "The Solar Output and Its Variations" (O. R. White, ed.), pp. 117–130. Colorado Assoc. Univ. Press, Boulder.

Vincente, R. O., and Yumi, S. (1969). Co-ordinates at the pole (1899–1968), returned to the conventional international origin. *Publ. Int. Latit. Obs. Mizusawa* **7,** 41–50.

Vincente, R. O., and Yumi, S. (1970). Revised values (1941–1961) of the co-ordinates of the pole referred to the CIO. *Publ. Int. Latit. Obs. Mizusawa* **7,** 109–112.

Walcott, R. I. (1970). Isostatic response to the loading at the crust in Canada. *Can. J. Earth Sci.* **7,** 716–727.

Walcott, R. I. (1972). Late Quaternary vertical movements in eastern North America. *Rev. Geophys. Space Phys.* **10**, 849–884.

Walcott, R. I. (1973). Structure of the earth from glacio-isostatic rebound. *Annu. Rev. Earth Planet. Sci.* **1**, 15–37.

Walcott, R. I. (1980). Rheological models and observational data of glacio-isostatic rebound. *In* "Earth Rheology, Isostasy, and Eustasy" (N.-A. Mörner, ed.), pp. 3–10. Wiley, New York.

Washburn, A. L., and Struiver, M. (1962). Radiocarbon-dated postglacial delevelling in Northeast Greenland and its implications. *Arctic* **15**, 66–72.

Weertman, J. (1961). Stability of Ice Age ice sheets. *JGR. J. Geophys. Res.* **66**, 3783–3792.

Weertman, J. (1976). Milankovitch solar radiation variation and ice age sheet size. *Nature (London)* **261**, 17–20.

Weertman, J. (1978). Creep laws for the mantle of the earth. *Philos. Trans. R. Soc. London Ser. A*, 110–125.

Wegener, A. (1926). "The Origin of Continents and Oceans." Dover, New York.

Wu, P., and Peltier, W. R. (1982a). Viscous gravitational relaxation. *Geophys. J. R. Astron. Soc.* (in press).

Wu, P., and Peltier, W. R. (1982b). Glacial isostatic adjustment and the free air gravity anomaly as a constraint on deep mantle viscosity. *Geophys. J. R. Astron. Soc.* (in press).

Yagi, T., Bell, P. M., and Mao, H. K. (1979). Phase relations in the system MgO–FeO–SiO_2 between 150 and 700 kbar at 1000°C. *Year Book Carnegie Inst. Washington* **78**.

Yamashita, T. (1979). Aftershock occurrence due to viscoelastic stress recovery and an estimate of the tectonic stress near the San Andreas fault system. *Bull. Seismol. Soc. Am.* **69**, 661–688.

Yuen, D. A., and Peltier, W. R. (1982). Normal modes of the viscoelastic earth. *Geophys. J. R. Astron. Soc.*, 495–526.

Zener, C. A. (1948). "Elasticity and Anelasticity of Metals." Univ. of Chicago Press, Chicago, Illinois.